Fundamental and Applied Electrochemistry for Photonic Applications

by

Saurabh Acharya

A dissertation submitted in partial fulfillment
of the requirements for the degree of
Doctor of Philosophy
(Electrical Engineering)
in the University of Michigan
2020

Doctoral Committee:

Professor L. Jay Guo, Chair
Professor Wei Lu
Professor Mark E. Meyerhoff
Professor Zetian Mi

Saurabh Acharya

sachar@umich.edu

ORCID iD: 0000-0002-2855-457X

To my parents,

B. S. ACHARYA

and

SHEELA ACHARYA

for their unconditional love and unwavering support

ACKNOWLEDGEMENTS

I have many people to thank for making this thesis possible. First and foremost, I would like to thank my advisor, Professor L. Jay Guo. His enthusiasm for research and for life in general is contagious and he has been a constant source of inspiration for me during my graduate studies. I have learnt greatly from our discussions on science and nonscience related topics, and I thank him for all the support and mentorship he has provided me. He was always patient and supportive, and provided me with very important insights whenever I was stuck with something in research or life. I am grateful for the various comments and life experiences he shared to guide me along the right path and to improve myself. In addition to supervising my research, he gave me the exciting opportunity of working towards commercializing our technology and exposed me to a world I otherwise would have never seen. This was an unforgettable experience, which will definitely shape the way I perceive and plan for my future endeavors.

I wish to express my gratitude to Professor Mark Meyerhoff, Professor Wei Lu and Professor Zetian Mi for serving on my thesis committee. Without their valuable suggestions, this thesis would be incomplete. I would also like to thank Professor Stephen Maldonado for introducing me to the amazing field of electrochemistry, and providing the opportunity to perform research on the electrochemical growth of crystalline semiconductors and investigations on kinetic processes at semiconductor/liquid interfaces. His advising on this part of the thesis is highly appreciated. I am grateful to Professor Jamie Phillips for his guidance during the initial years of

my graduate studies. I would like to acknowledge my mentors and colleagues from Chemistry, Dr. Luyao Ma, Dr. Sudarat Lee, Dr. Tim Zhang, Dr. Joshua DeMuth, Dr. Sofiya Hlynchuk, Molly MacInnes, and Quintin Cheek for their time and productive discussions which helped me significantly as I was still getting exposed to electrochemistry. I am grateful for all their kindness and the lessons I have learnt from them. Special thanks to Mitchell Lancaster, with whom I had a great experience collaborating with while working on semiconductor ultramicroelectrodes. I would like to thank Professor Rachel Goldman and Theodore Jimson for their assistance in preparing MBE-deposited Ga nanodroplets for Ge nanowire growth. Thanks to Anthony Aiello from the Bhattacharya Group and Fuxi Cai from the Lu Group for their assistance in characterizing some of the materials mentioned in this work.

I also appreciate Dr. Chengang Ji for getting me interested in photonic applications, for sharing his knowledge on the optical design of structural colors, and for guiding me to become a better researcher. I had a great time working with Kaito Yamada, Dr. Zhengmei Yang, Yongbum Park, Changyeong Jeong and Dr. Qingyu Cui on a variety of successful projects ranging from structural color filters for aesthetic applications to transparent flexible conductors for displays to photodetectors for finger print sensing. I am fortunate to have crossed paths with these talented people and wish I could spend more time working with them. I would also like to thank other past and present members of the Guo Group, Dr. Qiaochu Li, Dr. Dong Liu, Dr. Sangeon Lee, Heyan Wang, Danyan Wang, Zhenya Meng, Zhong Zhang, Yeonjoon Cheong, Jihun Lim, Suneel Joglekar, Sunghyun Nam, Weijie Feng, Yichun Zhang, Boonjae Jang, Jennie Paik, Zeyang Liu, and Dr. Semi Oh. Their cooperation has made this work successful, and my graduate school experience a fruitful experience.

I would like to thank all staff members of the Lurie Nanofabrication Facility (LNF) and Electron Microbeam Analysis Lab (EMAL) at the University of Michigan for their continuous support. I am grateful for all the help provided by Robert Hower, Nadine Wang, Gregory Allion, Dennis Schweiger, Brian Armstrong, Matthew Oonk, David Sebastian, Samuel Edwards, Terre Briggs, Kevin Owen, Shawn Wright, Anthony Sebastian, and many others at the LNF. I am also thankful to Zhongrui (Jerry) Li and Owen Neill at EMAL for their mentorship and support in teaching me various material characterization techniques. Thanks to Divya Patil Hangargekar at the University of Michigan's Center for Entrepreneurship for sharing her enthusiasm and for opening up various enriching opportunities for me. I am extremely grateful to Anne Rhodes, Elissa Trumbull, Jessi Cebulski, Jennifer Honeycutt, and Kevin Calhoun. Their administrative support has helped me throughout my graduate school career.

Special thanks to everyone who made my stay in Ann Arbor a happy one – Ameya, Anurag, Ayush, Dhanvin, Harsha, Jessica, Sajal, Siddharth (my cousin) and Anisha. Finally, my heartfelt appreciation and gratitude to my family - my parents and my sister Sowmya, whose unfailing support and encouragement has been a constant source of strength throughout my graduate studies. This thesis would not have been possible without your constant love and support.

TABLE OF CONTENTS

LIST OF TABLES

LIST OF FIGURES

Figure 7.5 Time-dependence of normalized steady-state voltammetric responses of a) non-degenerately doped and c) degenerately doped Si SUMEs in 0.1 M KCl containing 2 mM $Ru(NH_3)_6^{3+}$ over time. Scan rate: 10 mV s^{-1}, r = 5 μm. Half-wave potentials of the SUME response for b) non-degenerately doped and d) degenerately doped Si SUMEs as a function of time.⋯ 131

Figure 7.6 a) Mott-Schottky plots for freshly etched and oxidized 0.19 cm^2 n-Si electrodes in 0.1 M KCl. b) Voltammetric responses of freshly etched and treated non-degenerately doped n-Si SUMEs in 0.1 M KCl containing 2 mM $Ru(NH_3)_6^{3+}$. Scan rate: 10 mV s^{-1}, r = 5 μm. ⋯⋯⋯ 133

Figure 7.7 Fraction of potential dropped across space charge region in n-Si with N_d = 1.6 x 10^{15} cm^{-3} immersed in water with an ionic strength of 0.1 M as a function of the applied potential. 135

Figure 7.8 a) Concentration-dependent voltammetric response to $Ru(NH_3)_6^{3+}$ for a 5 μm n-Si SUME. The scan rate was 10 mV s^{-1}. b) Plot of the voltammetric wave position at E = -0.28, -0.30, -0.32, -0.34, -0.36, -0.38, and -0.40 V vs. E(Ag/AgCl) as a function of concentration. ⋯⋯⋯ 136

Figure 7.9 Normalized voltammetric responses of n-Si SUMEs with r = 5 μm in separate 0.1 M KCl aqueous solutions containing either (red) 2 mM $Ru(NH_3)_6^{3+}$, (blue) 2 mM MV^{2+}, or (purple) 2 mM $Co(sep)_3^{3+}$. The corresponding best fit line for each measurement is shown in black. The dashed line indicates the conduction band edge determined from separate impedance measurements. Color-coded arrows show the standard potential for each redox couple. Scan rate: 5 mV s^{-1}. ⋯⋯⋯ 137

Figure 8.1 Schematic representation of the proposed tunable structural color device with an embedded SiO_2 solid electrolyte layer.⋯⋯⋯ 151

Figure 8.2 Schematic of proposed all-solid-state tunable structural color device making use of the catalytic property of Pt.⋯⋯⋯ 152

ABSTRACT

Photonic devices that selectively transmit or reflect light are highly desirable in a wide variety of applications, including energy harvesting, aesthetic decorations and optical displays. However, most of these high optical-quality devices demonstrated to date involve complex patterns or expensive fabrication processes, which limits high volume production. In comparison, electrochemical methods can be simultaneously performed under mild conditions and with the unique advantage of being applicable to objects of arbitrary shape and size.

This dissertation is focused on using two ambient condition approaches to fabricate photonic devices with the capacity for scaling up. First, the electrochemical liquid-liquid-solid (ec-LLS) growth technique is used to grow crystalline semiconductor micro/nanowires at $T < 80$ C and Ge nanowire-based broadband absorbers on thermally sensitive substrates. The low temperature aspect of ec-LLS makes this process compatible with a wide variety of substrates ranging from metals to semiconductors to conducting polymers. This thesis provides a detailed study on the critical factors affecting ec-LLS crystal growth, and the scope for implementation of this growth method for practical applications is detailed. Additionally, electrical and optical characterization of ec-LLS grown Ge micro/nanowires are presented. Second, electrochemical techniques are used to fabricate angle-insensitive structural color filters by sequential electrodeposition of tri-layer asymmetric metal/dielectric/metal Fabry-Pérot cavities. Additionally, low-power consumption tunable color filters are achieved by employing an electrochemical effect

into the structural color design. It is shown that the proposed structures offer advantages over existing colorant-based filters in terms of high efficiency, lifetime and switching stability. The benchtop electrodeposition method utilized avoids any reliance on vacuum systems and ancillary equipment.

To have a finer control over the electrodeposition processes explored above, it is imperative to understand electrochemical processes and electron transfer processes at semiconductor/liquid junctions. In the last part of the thesis, theoretical and experimental studies on semiconductor-liquid interfaces using individual ultra-micro electrodes are presented, which test the accuracy of Marcus theory at these interfaces. The intent is to develop methodologies that test the extent that classical Marcus theory describes charge transfer at semiconductor/liquid interfaces, and to afford more reproducible and precise measurements of heterogeneous electron transfer rates than are currently available in the literature.

Chapter 1

Introduction

1.1 Background

In the last fifty years, society has become increasingly dependent on semiconductor devices. Research and development on transistors, optoelectronics, memory devices, sensing applications, etc. has been driven by the constant need to improve semiconductor devices. In addition to this, new technologies that have emerged in the areas of photonics and semiconductor electronics (e.g. flexible electronics on plastic substrates) that put stringent limitations on the device fabrication and semiconductor growth methods employed. Traditionally, monolithic semiconductor devices are fabricated using single crystalline semiconductor wafers using a top-down approach (subtractive steps). However, in contrast to the top-down approach, the bottom-up approach (additive steps) enables the growth and fabrication of nanostructures and other complex architectures with low material and processing costs.

Traditionally, crystalline semiconductor growth has been driven by two strategies: (1) employing high temperatures during crystal growth, and (2) employing a fluid medium that can solvate the adatoms of the crystal at the solid/fluid interface, thereby enabling a reversible pathway between these two phases. The first strategy imparts a high surface mobility to the adatoms on the

growth surface (Figure 1.1). This results in efficient rearrangement of adatoms on the crystal growth front and promotes a defect free crystal lattice. This concept is the basis for the various vapor phase epitaxy (VPE) techniques, which have been around since the 1960s, that include molecular beam epitaxy (MBE)[1] and metal organic vapor phase epitaxy (MOVPE)[2] techniques.

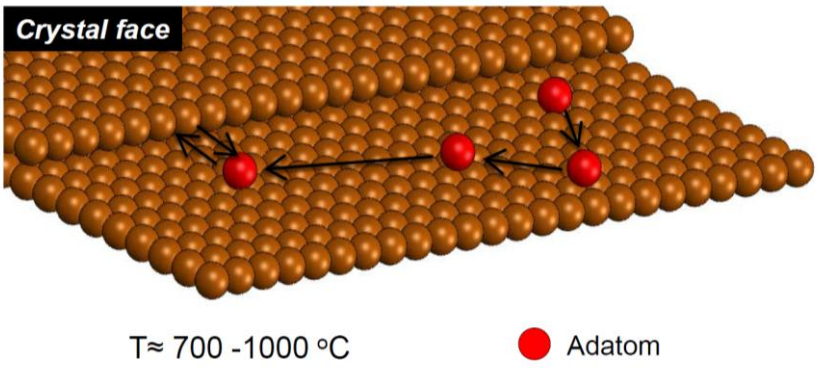

Figure 1.1 Schematic depicting crystalline semiconductor growth at high temperatures to promote fast adatom surface mobilities. (Courtesy of Dr. J. DeMuth, University of Michigan)

The second strategy is the basis for several growth techniques such as liquid phase epitaxy (LPE),[3, 4] vapor-liquid-solid growth (VLS),[5] solution-liquid-solid growth (SLS),[6, 7] etc. These methods employ metals capable of dissolving covalent semiconductors. Relatively high temperatures are used to ensure the metals are in the liquid state and capable of dissolving the covalent semiconductors. The solid/fluid interface formed between the nucleating surface and the liquid metal forms a reversible pathway wherein semiconductor atoms can either deposit at the crystal growth front or dissolve back into the liquid metal (Figure 1.2). This reversible pathway

allows for the correction of defects at the crystal growth front and ultimately results in high quality crystal growth.

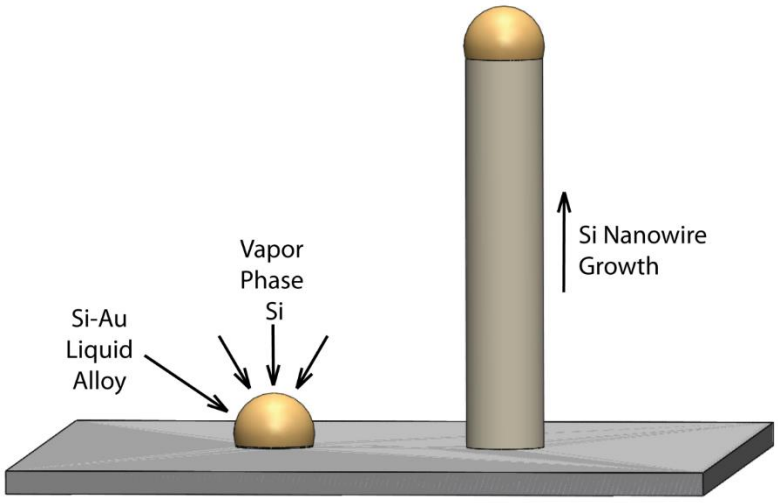

Figure 1.2 Schematic representation of crystalline semiconductor growth method employing a fluid medium that can solvate the adatoms of the crystal at the solid/fluid interface.

Although these strategies produce high-quality defect-free semiconductor thin-films and micro/nanowires, they all suffer from three main drawbacks. First, the high growth temperatures employed makes these processes incompatible with thermally sensitive substrates and substrates comprised of pre-existing device architectures. Second, the highly-processed, toxic, and corrosive precursor gases used in these processes add significant costs when considering large-scale processing. Third, the VPE and LPE techniques require strictly controlled ultra-high vacuum environments. As a result, the complex ancillary equipment employed render these processes very energy and cost intensive.

In contrast to the crystal growth methods mentioned above, electrochemical liquid-liquid-solid growth (ec-LLS) is an aqueous process conducted at lab ambient conditions.[8-12] This process has several advantages over its traditional counterparts. First, ec-LLS is a bench-top process and the instrumentation required for this process is comparatively simple. This is in sharp contrast to previously mentioned growth techniques, most of which use excessive ancillary equipment. Second, this process uses benign precursors that are formed using non-energy intensive processes. Third, the use of an electrochemical gradient rather than a thermal gradient to drive crystal growth allows the use of much milder growth conditions compared to the methods mentioned above. Section 1.3 provides an overview of the ec-LLS crystal growth process. Cumulatively, the first part of this thesis identifies and studies the critical factors that affect crystal growth in ec-LLS in detail, and also highlights efforts made to improve the purity of crystals grown using ec-LLS. Further, electrical and optical characterization of the as-grown ec-LLS micro/nano structures is demonstrated.

Ec-LLS offers a low-cost, benchtop alternative to conventional semiconductor crystal growth methods, while also possessing milder growth conditions. On the same grounds, different solution-based electrochemical approaches and electrodepositions can be further applied to other electrical and photonic devices to address cost, performance and scaling-up issues. This thesis identifies structural colors as one such application that can benefit from the various advantages offered by electrochemistry.

For the case of color generation, many schemes based on plasmonic or guide-mode resonances have been proposed and demonstrated.[13-17] However, these structures typically involve sub-wavelength patterns that require complex and time-intensive fabrication techniques such as e-beam lithography and focused ion beam milling, significantly limiting their ability to be fabricated

in high volume. Multilayered structural colors fabricated using additive deposition techniques provide one possible solution for mass-production.[18-21] Roll-to-roll vacuum deposition methods have been developed for obtaining pigment flakes exhibiting unique metallic appearance with high purity for decorative paints and colored solar cells,[22] however these methods carry a high cost associated with having to rely on vacuum deposition systems. Thus, approaches that produce high quality thin-films at ambient conditions are highly desirable. In this regard, this thesis introduces a novel, low-cost electrodeposition approach to fabricate structural colors, with a potential to scale-up.

The electrochemical approaches mentioned above involve semiconductor/liquid junctions and complete measurements of charge transfer at these interfaces are desired in order to drive electrochemical processes at the most efficient conditions. The topic of semiconductor electrochemistry has been critical to advancing fundamental electrochemical concepts, including the nature of charged solid/liquid interfaces, heterogeneous reaction kinetics, photochemical processes, and corrosion/passivation.[23] Semiconductor electrochemistry also is at the heart of many long-standing applied technologies such as semiconductor wet etching,[24-26] ion-sensitive field effect transistor sensors,[27, 28] and photoelectrochemical energy conversion strategies.[29-31] Paradoxically, though, the ability to interpret readily, quantitatively, and unambiguously even the most basic voltammetric responses for charge transfer between a semiconductor electrode and a dissolved redox species is still a challenge.[32-39] Taking this into account, this thesis introduces semiconductor ultramicroelectrodes (SUMEs) a new tool for accurate measurement of charge-transfer processes at semiconductor/liquid interfaces.

1.2 Aqueous Electrodeposition of Crystalline Covalent Semiconductors

Ec-LLS is a hybrid synthetic method developed to prepare crystalline inorganic materials at ambient conditions. Combining elements of electrodeposition and melt crystal growths, the ec-LLS process uses electrochemistry to drive solutes of interest into liquid metals where nucleation and crystal growth can occur. The main premise in ec-LLS is that a liquid metal cathode acts both to reductively activate a precursor(s) and as a solvating phase for semiconductor species. In this way, an applied electrochemical gradient, rather than a thermal gradient, is exploited to nucleate and to sustain crystal growth.

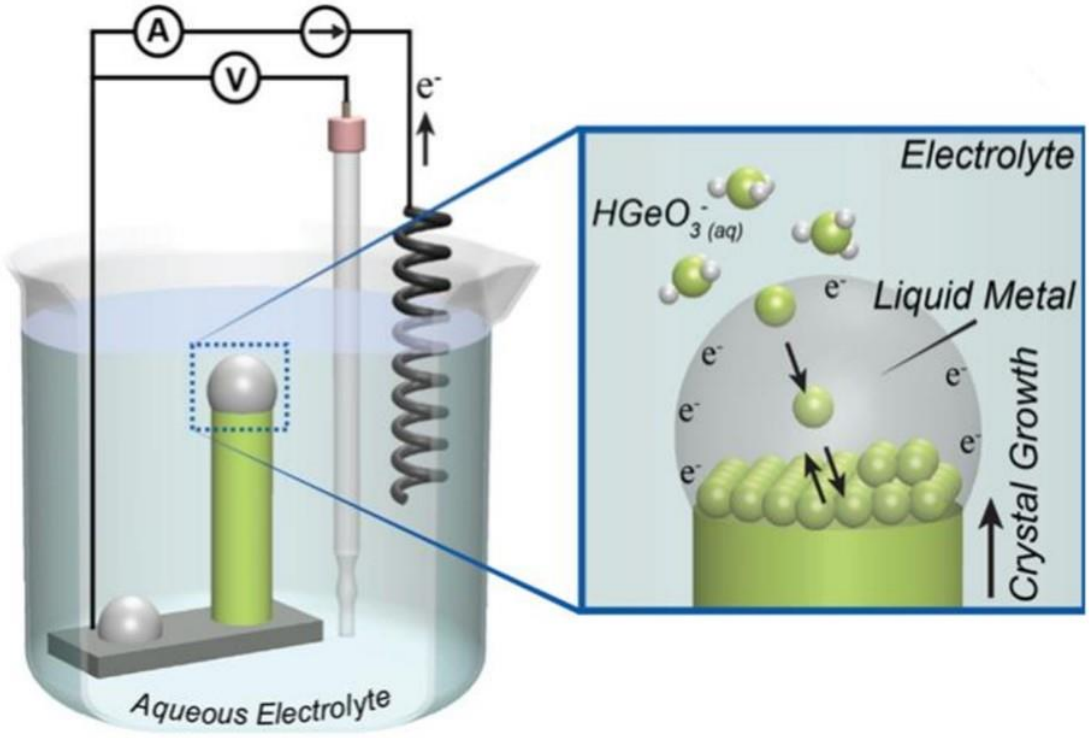

Figure 1.3 Schematic illustration of electrochemical liquid-liquid-solid process. (Fahrenkrug, E; et al. *Chem. Mater.*, 2015, *27* (9), pp 3389–3396)

The ec-LLS process can be broken down into four elementary steps. To synthesize semiconductor crystals using ec-LLS, the oxidized form of the semiconductor is dissolved in solution and is brought in contact with the liquid metal that is deposited on a conductive substrate. First, to initiate the ec-LLS process, a potential must be applied to the liquid metal electrode, which provides the driving force for the reduction of the dissolved oxidized precursor to the zero valent state. In this thesis, germanium oxide (GeO_2) was used as the precursor for the ec-LLS growth of Ge crystals. On application of a reductive potential, zero valent Ge is formed through the following reaction:

$$HGeO_3^-\ (aq) + 4e^- + 2H_2O \rightarrow Ge\ (s) + 5OH^-\ (aq) \qquad (1.1)$$

Second, the semiconductor adatoms dissolve into the liquid metal owing to their non-zero solubility at the growth temperature. The minimum growth temperature allowed for ec-LLS is dictated by the melting point of the liquid metal used. For example, while using eutectic Ga-In as the liquid metal, ambient condition semiconductor crystal growth can be achieved at T = 60 ºC. Third, if the oxidized precursor is reduced further, a concentration gradient of zero valent Ge is formed between the surface and interior of the liquid metal which drives the dissolution Ge (s) into the bulk of the liquid metal droplet. Lastly, the concentration of Ge (s) in the liquid metal droplet eventually exceeds its equilibrium solubility, which induces nucleation and growth of semiconductor crystals. These four steps are illustrated in Figure 1.3.[40] The size of the liquid metal droplet utilized determines the nucleation sites of the semiconductor crystals. Macroscopic liquid metal droplets result in homogenous nucleation, whereas heterogenous nucleation on the

underlying solid substrate is achieved when using nano- and micro-sized liquid metal droplets or thin-films (Figure 1.4).

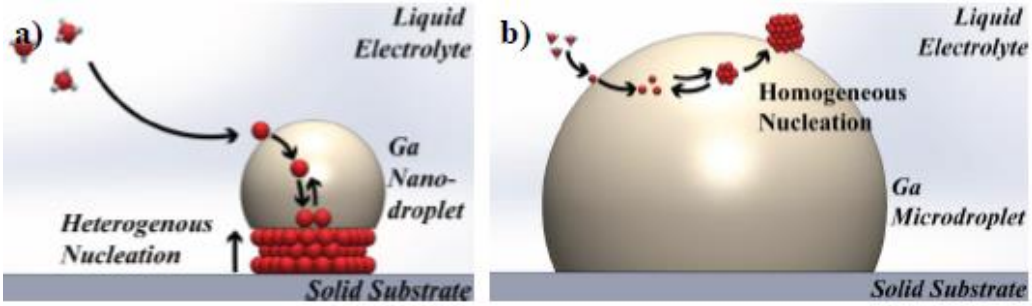

Figure 1.4 Schematic illustration of (a) heterogenous nucleation (b) homogenous nucleation during the ec-LLS growth process. (Courtesy of Dr. L. Ma, University of Michigan)

1.4 Thesis Outline

The work in this thesis can be split into two separate objectives. The first part involves work on deposition techniques that do not rely on vacuum-based systems and other ancillary equipment. The aim of this part is to improve new methodologies for ambient condition, benchtop growth of semiconductor crystals and to utilize these new or existing methods to develop novel, low-cost, scalable processes for the fabrication of electrical or optical devices. The second objective of this thesis is to develop and verify a new platform (Semiconductor Ultramicroelectrodes, SUMEs) to precisely measure charge transfer processes at semiconductor/liquid junctions. In this thesis, experimental measurements of charge transfer using SUMEs are demonstrated for Si in an aqueous electrolyte.

In chapter 2, alloys of gallium and indium ($Ga_{1-x}In_x$) are used as liquid metal nano/microdroplet electrodes in ec-LLS to determine whether the resultant conductivity of as-grown Ge could be strongly modulated by adjusting the fraction of Ga. Current-potential measurements on individual microwires were performed as a function of alloy composition. All alloys of Ga and In yielded Ge microwires with low resistivity and showed evidence of metal incorporation beyond the solubility limit (i.e. hyperdoping). This chapter also presents electrical characterization data on Ge nanowires grown using Ga-free liquid metal nanodroplets.

Chapter 3 identifies factors that affect crystalline growth of germanium (Ge) micro- and nanowires by the ec-LLS method in an aqueous solution. The observed Ge crystal growth rates were insensitive to the alloy composition. In contrast, lowering the concentration of GeO_2 dissolved in solution and/or increasing the density of droplets noticeably slowed down the microwire growth rate. Complex potential-time waveforms for ec-LLS consisting of a sequence of potential steps were separately employed for the first time and strongly affected the morphology of the nanowires, the occurrence of kinking, and their resultant growth directions. Cumulatively, the data presented here help define what parameters should be useful in refining the ec-LLS method to produce materials with specific targeted properties.

Chapter 4 demonstrates a simple, inexpensive, and non-toxic bench-top electrodeposition process for the fabrication of structural color filters at ambient conditions. This process avoids the need for expensive vacuum-based equipment and is compatible with highly non-planar substrates of arbitrary shape, size and roughness. Asymmetric metal-dielectric-metal multilayered structures are prepared by sequential electrodeposition of smooth gold, thin cuprous oxide, and finally thin Au on conductive substrates, forming an effective optical cavity. Different colors of high brightness were achieved by simply tuning the thickness of the electrodeposited middle cavity

layer. Due to the high refractive index of the cuprous oxide dielectric layer, the vividness of the generated colors was invariant to viewing angle. This chapter also highlights the clear advantages of this approach over traditional deposition or assembly methods for preparing colored films.

Chapter 5 demonstrates a simple design approach to generate multiple reconfigurable optical colored states using a single structural color device or pixel. Tunability between the different colored states were achieved by utilizing an electrochromic thin-film as the dielectric anti-reflection layer in the structural color device, wherein the effect of change in optical constants of the electrochromic thin-film is analogous to the change in the thickness of the dielectric thin-film. Studies related to the design principles, stability and cycling performance are also discussed in this chapter.

Chapter 6 details the theoretical similarities and differences between inlaid and recessed ultramicroelectrodes (UMEs). The geometrical conditions are described for which analytical equations derived for an inlaid UME can be safely applied to a recessed UME without any significant errors while extracting the charge transfer parameters. In this chapter, theoretical studies are performed for metal/liquid junctions, however this analysis of inlaid vs. recessed UME responses can be extended to SUMEs too and it lays the foundation for the next chapter.

Chapter 7 describes the preparation, characterization, and utility of semiconductor ultramicroelectrodes for the study of heterogeneous charge transfer reactions at semiconductor/electrolyte interfaces.

Chapter 8 summarizes future directions related to the work presented in this thesis.

Chapter 2

Effect of Liquid Metal Composition on the Growth of Hyperdoped Germanium Microwires by ec-LLS

Acharya, S.; Ma, L.; Maldonado, S. *ACS Applied Nano Materials* **2018** *1* (10), 5553-5561 [†]

2.1 Introduction

The main premise in electrochemical liquid-liquid-solid (ec-LLS) is that a liquid metal acts both as a cathode to electrochemically reduce an oxidized precursor(s) into a zero valent semiconductor and as a medium to nucleate and grow semiconductor crystals (Figure 2.1, inset).[8] As detailed in the previous chapter, a consequence and primary advantage of this unorthodox approach is that ec-LLS does not necessarily involve high temperatures since an electrochemical stimulus rather than a thermal input is employed to drive material formation. This aspect makes ec-LLS potentially attractive for preparing optoelectronic devices based on crystalline inorganic semiconductors directly on soft, thermally-sensitive, and flexible substrates. Preliminary work on

[†] All experiments, data analysis, and figure construction for this chapter were performed by Saurabh Acharya. APT data was acquired by Luyao Ma. Stephen Maldonado was the principal investigator for the project.

this front has been demonstrated,[41] but there are still several elementary questions regarding optimization of ec-LLS conditions in order to produce the highest quality semiconductor materials.

One principal variable in ec-LLS is the choice of liquid metal. Gallium (Ga) is an attractive metal solvent for low temperature ec-LLS due to its low melting point (29.7 °C)[42] and its capacity to solvate many Group IV and III-V semiconductors. However, pure Ga is limited as a semiconductor growth solvent in one primary aspect. Various reports of Ga as a liquid metal solvent in semiconductor growth by melt crystal growth,[43] liquid phase epitaxy,[44] and vapor-liquid-solid processes[45] indicate that Ga tends to incorporate into the resultant semiconductor crystal (as a p-type dopant) at high levels, rendering the as-grown materials highly conductive. Even when crystals are grown under (slow) equilibrium conditions,[43, 46] a Ga atom at the crystal growth front is readily 'trapped' in Ge and Si crystals in part because its comparable size provides no basis for exclusion. A recent report demonstrated 'hyperdoped' Ge nanowires grown with Ga nanodroplets even with an extremely slow growth rate (~ 0.2 nm/s).[46] To be clear, controllable hyperdoping of Ge can be beneficial. For example, hyperdoping Ge with Sn[47] is one strategy to impart a direct bandgap, assuming aspects like strain and crystal structure are also properly controlled.

Since the solid solubility of indium (In) in Ge is approximately two orders of magnitude lower than Ga in Ge[48] and since it was previously noted that there is qualitative evidence of lower metal incorporation in nanowires/microwires grown with eutectic gallium indium alloy (e-GaIn) as compared to pure Ga,[49] one critical question in ec-LLS is whether the specific composition of Ga-based alloys mitigates the tendency of Ga to incorporate into the resultant crystals. Alloys of Ga and In are notable since they remain molten at low temperature over a wide compositional range (Figure 2.1).

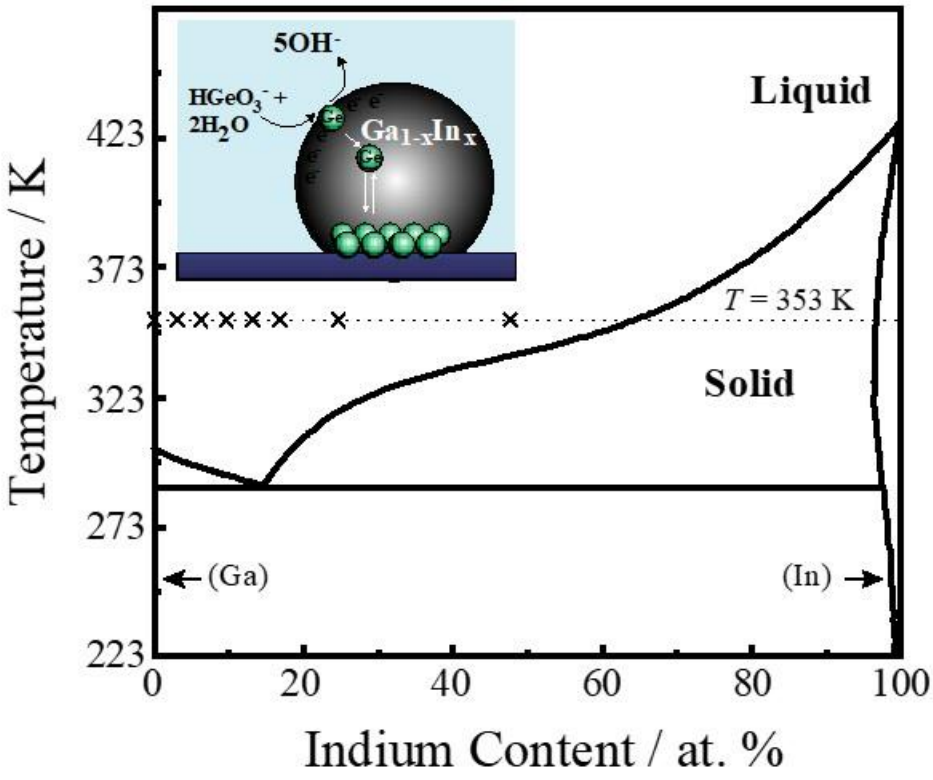

Figure 2.1 Binary phase diagram for Ga-In alloys. The dashed line represents the ec-LLS temperature used in this work and each x represents a specific composition used for ec-LLS in this work.

Accordingly, in this chapter, the effect of the tuning the liquid metal composition on ec-LLS crystal growth is investigated. The resistivity of Ge microwires grown by ec-LLS involving the reduction of GeO_2 dissolved in water[50] and a range of liquid gallium alloys ($Ga_{1-x}In_x$) is gauged to determine whether a larger alloying metal can provide the size exclusion necessary to inhibit Ga doping in the resultant crystal (Figure 2.1).[51] This resistivity measurements are complemented

by Atom Probe Tomography to get a better understanding of the presence of the dopants and impurities present in the as-grown Ge microwires.

2.2 Experimental Methods – Growth of Ge Microwires and Fabrication of Devices

2.2.1 Preparation of Liquid Metal Microdroplet Arrays

Acetone (ACS grade, Fisher Scientific), indium (99.99% Gallium Source), gallium (99.999%, Alfa Aesar), germanium dioxide (99.998% Sigma-Aldrich), sodium borate (>99.5% Sigma-Aldrich), buffered hydrofluoric acid (Transene Inc.), wet etching solution GE-8111 (Transene Inc.), hydrochloric acid (37%, Sigma-Aldrich), methanol (ACS grade, Fisher Scientific), 2-propanol (ACS grade, Fisher Scientific), SU-8-2010 (MicroChem Corp), SU-8 developer (MicroChem Corp), MEGAPOSIT SPR 220 3.0 (Dow Chemical Company), AZ 726 MIF Developer (MicroChem Corp), and oxygen gas (Metro Welding, Detroit, MI) were used as received. Degenerately doped n-type Si(111) wafers (0.625 ± 0.020 mm, $\rho < 0.007$ Ω·cm, Addison Engineering, Inc.) and p-type Si(111) wafers (0.525 mm, $\rho < 0.004$ Ω·cm SunEdison) were diced and used as substrates. Water with a resistivity >18.2 MΩ·cm was used throughout.

Photoresist films patterned with arrays of regularly spaced cylindrical holes ($r = 5$ μm) on Si wafer substrates were prepared using standard photolithographic procedures. All substrates were first plasma cleaned (300 W, 100 sccm O_2(g), 12 sccm Ar(g), Glen 1000P Plasma Cleaner) for 2 minutes. The wafer substrates were further degreased by sequentially sonicating for 5 minutes each in acetone, methanol and water, then dried under a N_2(g) stream. 10 μm thick SU-8 2010 film was then spin-coated onto each Si wafer and was allowed to air dry for 2 minutes at room

temperature prior to soft baking on a hotplate at T = 95 °C for 3 minutes. Edge bead removal was performed on the wafers only when required. Following, the substrates were exposed (hard-contact mode) at 15-20 mW/cm^2 at the 405 nm wavelength (Karl Suss MA 45S) using a custom photomask that was patterned with multiple 15 x 15 mm^2 dies (μPG 501, Heidelberg Instruments). Substrates were subject to a post-exposure bake at T = 95 °C for 3.5 minutes on a hotplate and allowed to cool down to room temperature prior to developing. Development for 2.5 minutes under agitation with SU-8 developer (MicroChem) removed the unexposed regions of the photoresist. Following, the substrates were immediately rinsed with 2-propanol, dried under N_2 (g) and then hard baked in air at T = 150 °C for 20 minutes. Finally, the wafer was diced into individual 15 x 15 mm^2 pieces. To ensure the bottom of each patterned was free from any residual organic, the patterned substrates were subjected to another plasma etching step (400 W, 15 sccm O_2(g), PE-50, Plasma Etch Inc.) for 1.5 minutes.

$Ga_{1-x}In_x$ alloys of varying compositions, x = 3.1, 6.3, 9.7, 13.2, 16.8, 24.6, and 47.6 at. % (i.e. x = 5, 10, 15, 20, 25, 35 and 60 wt. %), were prepared by mechanically mixing stoichiometric amounts of metallic In and Ga at T = 100 °C. Immediately prior to use, the alloys were stirred again. Any native oxide at exposed Si substrate surface was removed by etching in buffered HF for 1 minute, rinsing vigorously with water and drying under N_2(g), immediately prior to use. To fill the patterned holes with the desired liquid metal, the patterned substrates were mounted on a vacuum chuck while approximately 1 mL of the liquid metal was dispensed. The liquid metal was repeatedly spread over the entire area and mechanically tapped into patterned holes. Excess liquid metal was removed by wiping with a methanol-soaked lint-free cloth (Kimtech W4, Fisher). For the alloys with higher melting points, the sample was heated to T = 65 °C during this step.

2.2.2 ec-LLS Ge Growth

Computer controlled potentiostats (CHI420A and CHI760C, CH Instruments) were used throughout. All ec-LLS experiments were performed in a three-electrode cell and heated to a specified temperature with an aluminum heating block. A thermocouple mounted on the underside of the Si wafer section was used to measure the temperature of the electrode. Custom-built, compression Teflon cells featuring a Viton O-ring defined the area of the working electrodes (either 0.041 or 0.919 cm^2). Ohmic contact to all Si substrates was made by applying e-GaIn to the back of the wafer. A platinum mesh and a silver wire coated with silver chloride immersed in 3 M KCl and sealed behind a glass frit were employed as the counter and reference electrodes, respectively. All potentials are referenced to *E*(Ag/AgCl). Unless otherwise mentioned, ec-LLS growths were performed at E = -1.6 V and T = 80 °C using a 0.05 M GeO_2(aq) and 0.01M $Na_2B_4O_7$(aq) solution and were restricted to 10 minutes in order to control the Ge microwire height between 20 to 30 μm.

2.2.3 Device Fabrication for Resistivity Measurements

Following the ec-LLS growth of Ge microwires, the liquid metal cap was etched by immersion in 1M HCl(aq) while held at a bias of E = -0.097 V. The fabrication of the vertical devices started with spincoating an insulator (SU-8 2010) on the sample followed by flood exposure and T = 95 °C hard bake, to isolate the Ge microwires from each other and to provide mechanical strength to the Ge microwires. The insulator was selectively etched back down using a plasma etch to expose the tip of the Ge microwires. The sample was then briefly dipped in buffered HF and immediately loaded into an e-beam evaporator, where 200 nm of Au was deposited from a 45° angle with a dome rotation of 15 rpm for contacting the Ge microwires from the top and the sidewall. Finally, a positive tone photoresist (MEGAPOSIT SPR 220 3.0) was spin-

coated onto the sample and photolithographically patterned to make individual 40 x 40 um^2 top contact pads to each Ge microwire. The Au between the contact pads was wet etched using GE-8111 and the patterned photoresist was dissolved in acetone followed by a dehydration bake. Current-potential measurements was performed using a Keithley 4200 semiconductor parameter analyzer and an Alessi probe station.

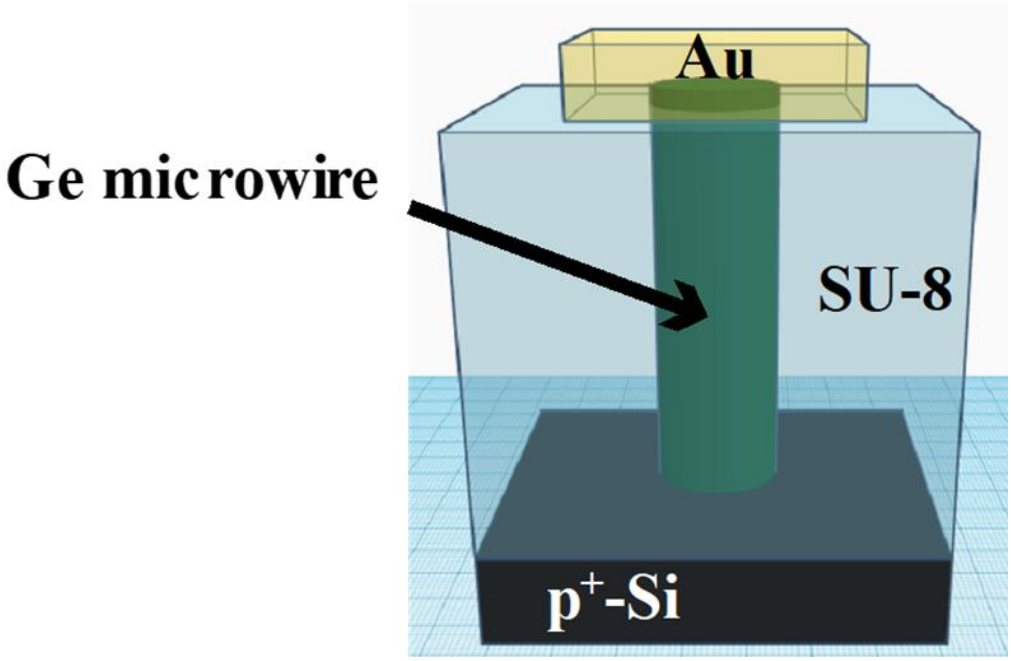

Figure 2.2 Device schematic for individual Ge microwire resistivity measurements.

2.2.4 Atom Probe Tomography Sample Preparation

Atom probe tomography (APT) was performed to determine the metal content in the as-prepared Ge microwires. Germanium microwires grown on p^+ Si substrates using $Ga_{1-x}In_x$ (x = 16.8 at. %) were sonicated in methanol and were cast onto a flat substrate. The APT samples were then prepared using a method already detailed elsewhere.[52, 53] Figure 2.3 provides a schematic illustration of the sample preparation process. All samples for APT analysis were prepared using

a FEI Helios 650 NanoLab focused ion-beam scanning electron microscope. The measured ratios of gallium-69 and gallium-71 before and after the sample preparation were the same, thus indicating no introduction of Ga contaminants into the sample during focused ion beam (FIB) processing.

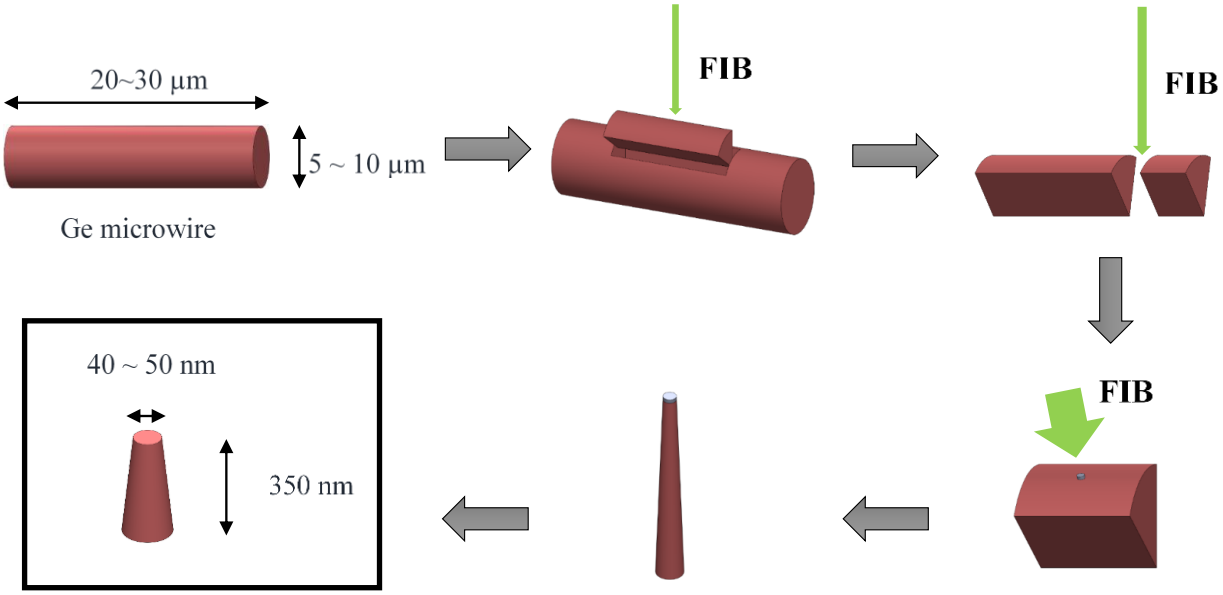

Figure 2.3 Schematic illustration of the APT sample preparation process.

2.3 Voltammetric Responses and ec-LLS Growth Rate as a Function of Liquid Metal Composition

Voltammetric responses for arrays of microdroplets with r = 5 μm were recorded at T = 80 °C (353 K) ± 2 °C for six different $Ga_{1-x}In_x$ alloy compositions, x = 3.1, 6.3, 9.7, 13.2, 24.6, and 47.7 at. % in 0.01 M $Na_2B_4O_7$ (aq) (Figure 2.4). At this temperature, all alloys were molten. In the blank electrolyte, the voltammograms were similar, save for a small cathodic wave peaked at -1.1 V from some alloys that was consistent with oxide removal.[54] More notably, the profiles and magnitudes of the H^+ reduction current at more negative potentials for all alloys were similar

(Figure 2.4a). The current at E = -1.6 V shown for each alloy in the inset of Figure 2.4a showed no obvious trend with In content. Based on these data, experiments in this electrolyte where the potential is held constant at E = -1.6 V for t = 1800 s would only pass approximately 0.015 C for H^+ reduction. However, upon addition of dissolved GeO_2 to the electrolyte, such experiments showed consistently higher currents above 10^{-4} A, implying a high Faradaic efficiency for the reduction of GeO_2. The current-time responses for the reduction of GeO_2 at E = -1.6 V (not shown) contained varying degrees of random current spikes presumably from H_2 bubbles. Therefore, the integrated charge vs time responses are presented instead (Figure 2.4b). The total charge passed with each alloy was consistently larger than the 0.015 C for just H^+ reduction for all alloys and corresponded to expected nominal Ge microwire lengths of 40 to 50 µm.

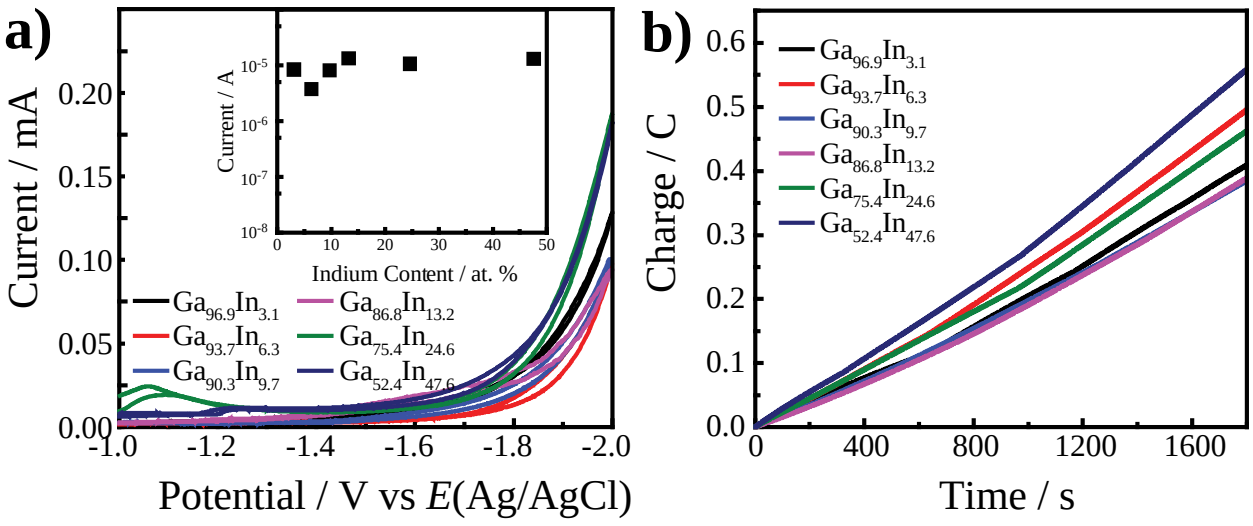

Figure 2.4 a) Voltammetric responses for microdroplet arrays with different compositions of $Ga_{1-x}In_x$ liquid metal in a blank electrolyte containing 0.01 M $Na_2B_4O_7$ (aq) at T = 80 °C and scan rate = 0.025 V s^{-1}. Inset: Current at E = -1.6 V as a function of $Ga_{1-x}In_x$ composition. b) Charge vs time plot for Ge microwire ec-LLS experiments performed in an electrolyte containing 0.05 M GeO_2 and 0.01 M $Na_2B_4O_7$ (aq) at T = 80 °C and E = -1.6 V using different compositions of $Ga_{1-x}In_x$ liquid metal.

Adding In to liquid Ga did not substantially alter all interfacial properties relevant to ec-LLS. There was no strong dependence of the activity for H^+ reduction at E = -1.6 V in the voltammetric responses recorded in the blank electrolyte for the different $Ga_{1-x}In_x$ compositions, in slight contrast to prior reports on $Ga_{1-x}In_x$ alloys which were collected only at room temperature.[55, 56] Since the data do not indicate a substantial difference in the faradaic efficiency for reduction of dissolved GeO_2 over H^+ reduction in this electrolyte, the addition of In does not appear to accelerate the rate of GeO_2 reduction drastically at the potentials of interest.

Figure 2.5a-f presents cross-sectional scanning electron micrographs of Ge microwire arrays electrodeposited by ec-LLS at E = -1.6 V and t = 1800 s for an array pitch of 30 μm (same as Figure 2.4b) as a function of $Ga_{1-x}In_x$ alloy composition. All of the Ge microwire films exhibited microwires that were oriented generally normal to the surface plane. However, a large plurality showed extensive kinking and changes in the growth direction that argued against both epitaxial growth and single-crystallinity. Figure 2.5g-h depicts the change in wetting of the Ge microwires by the liquid metal droplets. The contact angles between the surface plane of the microwire and the tangent of the surface of the liquid metal droplet at the interface were 160.47° and 144.66° for x = 3.1 at. % and 47.7 at. %, respectively. This implies a change in the interfacial character of the liquid metals. The wetting contact angles between the liquid metal alloys and the as-deposited solid Ge crystals became more pronounced with higher In concentrations. One strong inference from the change in wetting is that In atoms must also be present at the solid Ge/liquid metal interface. This general observation is in accord with the fact that these alloys, despite being still mostly composed of Ga, have some In character at the interface.[57]

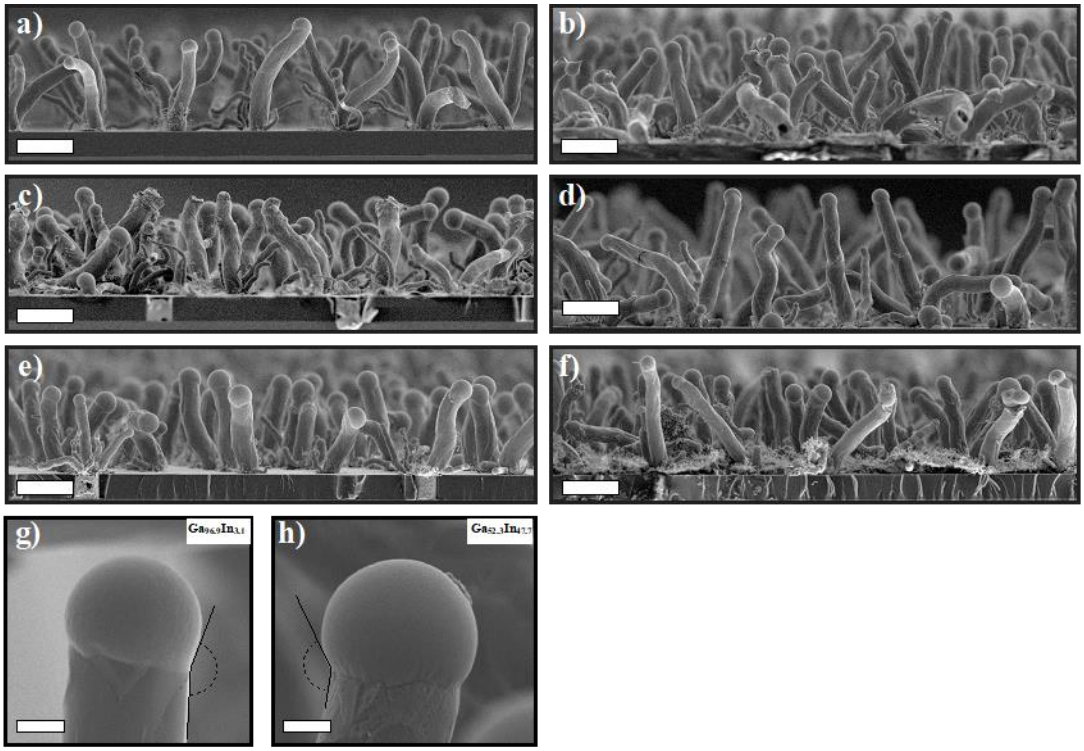

Figure 2.5 Cross-section scanning electron micrographs of Ge microwire ec-LLS experiments performed in an electrolyte containing 0.05 M GeO_2 and 0.01 M $Na_2B_4O_7$ (aq) at T = 80 °C and E = -1.6 V using different compositions of $Ga_{1-x}In_x$ liquid metal, where microdroplet array pitch = 30 µm and t = 1800 s. x = a) 3.1 at. %, b) 6.3 at. %, c) 9.7 at. %, d) 13.2 at. %, e) 24.6 at. %, and f) 47.6 at. %. Scale bars: 20 µm. Additional higher magnification scanning electron micrographs depicting the wetting of the top of the Ge microwire by the corresponding liquid metal droplet are shown for x = e) 3.1 and h) 47.6 at. %, respectively, with wetting angles of 160.47° and 144.66°, respectively. Scale bars: 2 µm.

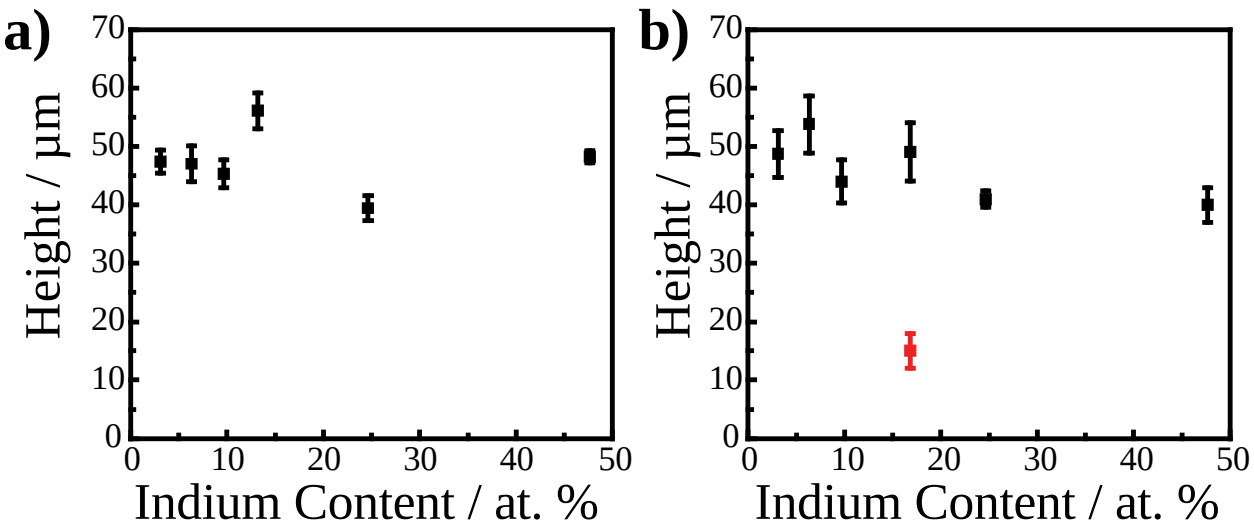

Figure 2.6 Ge microwire height as a function of $Ga_{1-x}In_x$ composition for a) *microdroplet pitch* = 30 µm and *growth time* = 1800 sec (b) *microdroplet pitch* = 110 µm and *growth time* = 600 sec. The red data point in b) corresponds to a sample with *microdroplet pitch* = 30 µm and *growth time* = 600 sec. All ec-LLS growths were performed in aqueous 0.05 M GeO_2 and 0.01 M $Na_2B_4O_7$ at T = 80 °C and E = -1.6 V.

Figure 2.6a plots the average heights of Ge microwires produced under the conditions described in Figure 2.5 as observed from cross-sectional scanning electron micrographs. An electrodeposition time of t = 1800 s yielded Ge microwires with lengths between 40 and 55 µm, in accord with the expectation from the electrochemical data with the assumption that the majority of charge passed results in the reduction of GeO_2 rather than H^+. The observed average microwire height showed no strong dependence with x in $Ga_{1-x}In_x$ composition, although changes in the pitch did strongly affect the microwire lengths (Figure 2.6b). The same nominal microwire length as in Figure 2.6a was attained in one third of the total time when the pitch was increased. Still, even with this change, there was no significant dependence on the microwire length and growth rate as a function of x in $Ga_{1-x}In_x$.

2.4 Electrical Characterization of ec-LLS Grown Ge Microwires

The electrical properties of the Ge microwires grown by ec-LLS were ascertained by measuring the current-potential characteristics of individual vertical Ge microwires of different lengths (l ~ 20, 30, 40 μm). Figure 2.7a depicts representative current-potential responses of four distinct Ge microwires with l ~ 30 μm on p+ Si (111) substrates, wherein $Ga_{1-x}In_x$ (x = 16.8 at. %) was used as the liquid metal solvent during Ge ec-LLS microwire growth. In these measurements, the potential was applied to the top Au contact while the back contact to the degenerately doped Si substrate was grounded. The small variations in the current-potential characteristics of the different microwires is due to the dispersity in the diameter of the microwires. The total resistance for each microwire was measured by analyzing the linear region of the current-potential plot (E = -0.5 to -0.1 V). The combined contribution of the Si substrate, contact resistance, and the Si/Ge interface to the total resistance measured was extracted from the y-axis intercept of Figure 2.7b. Over 30 individual microwires were measured for every $Ga_{1-x}In_x$ alloy composition.

The electrical resistivity of individual microwires was then calculated using *eq* 2.1,[58]

$$R_T = R' + \frac{\rho_s}{\pi r^2} l \qquad (2.1)$$

where R_T is the total resistance extracted from the current-potential profiles between 0 and -0.5 V, R' is the combined contribution of the Si substrate, contact resistance and the Si/Ge interface to R_T, r is the radius of the microwire and ρ_s is the resistivity of the semiconductor. Contributions of metal clusters to the Ge conductivity were assumed negligible and were not considered in this analysis, as described previously.[53]

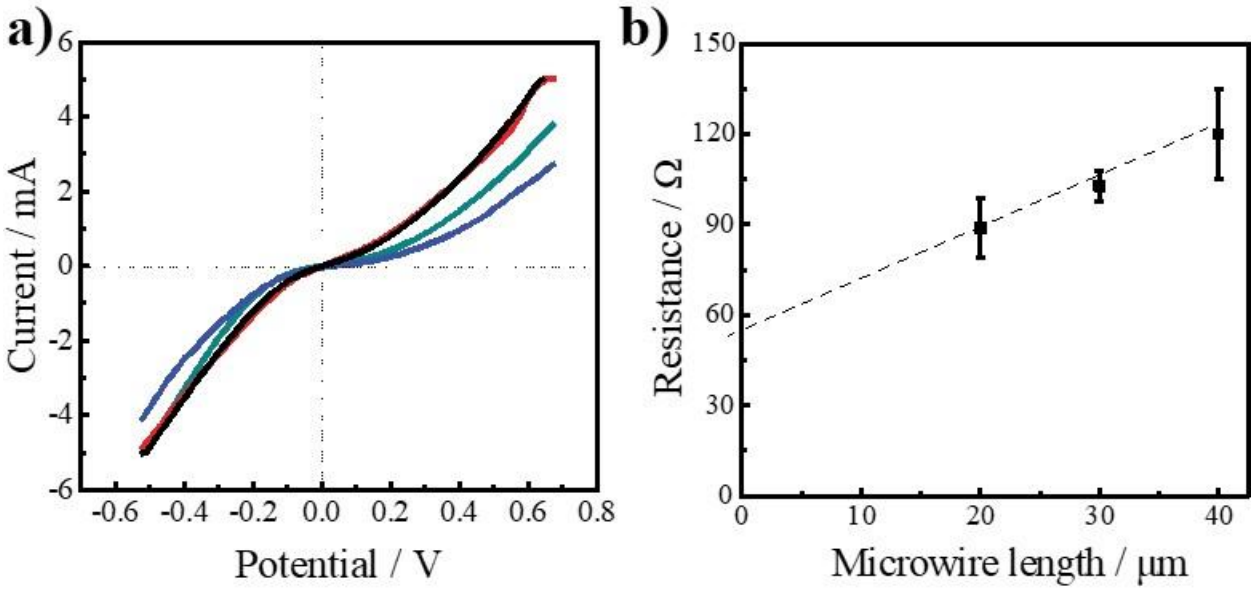

Figure 2.7 a) Representative current-potential characteristics of individual Ge microwires with *l* = 30 μm on p^+-Si(111) substrates b) Total resistance measured from the current-potential characteristics of Ge microwires grown using $Ga_{1-x}In_x$ (x = 16.8 at. %) microdroplets vs Ge microwire length.

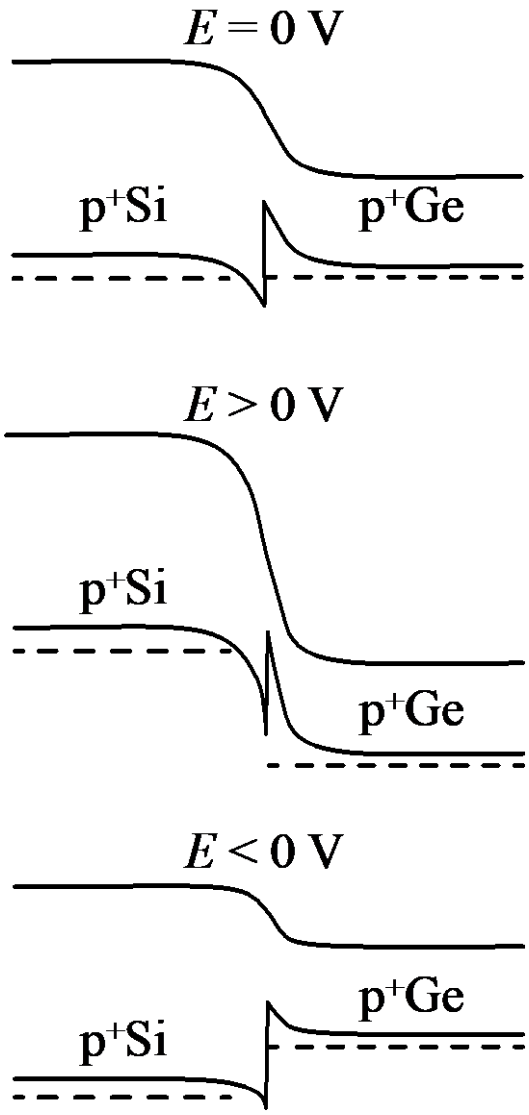

Figure 2.8 Energy band diagrams of p^+Si/p^+Ge heterojunctions at equilibrium and positive/negative biases.

In this analysis, R_T was explicitly extracted from the linear region of the current-potential responses from 0 to -0.5 V. This potential region was purposely used to simplify interpretation. Figure 2.8 shows band diagrams of p^+Si/p^+Ge heterojunctions at equilibrium and different applied biases. At progressively more negative biases, the activation barrier for electron flow from Ge into Si is minimized, minimizing the impact of the valence band offset between Si and Ge on the current-potential profile.

The resistivity of the crystalline Ge microwires determined using *eq* 2.1 is shown in Figure 2.9a. For every $Ga_{1-x}In_x$ alloy composition, over 30 individual microwires were measured. For all electrodeposited Ge microwires, the measured resistivity values were low, suggestive of two points. First, the changes in the alloy composition did not impart substantial changes in material resistivity. Second, the Ge microwire electrical properties were consistent with degenerate doping. Separately, Figure 2.9b plots the temperature dependent resistivity data performed using the same device structure while keeping the liquid metal composition fixed at $Ga_{1-x}In_x$ (x = 16.8 at. %). The insensitivity of the microwire resistivity to temperature further suggests a degenerate doping condition and points towards the presence of a continuous dopant band in the band structure of Ge.[59] The observation of statistically similar resistivities of the as-deposited Ge microwires across all $Ga_{1-x}In_x$ alloy compositions strongly suggests that In does not inhibit Ga from incorporating into the growing Ge crystallites. That is, if the presence of In lowered the activity of Ga at the crystal growth front, the expectation would be less Ga gets incorporated and the measured resistivities should increase with larger fractions of In. Since the data do not show such a trend, any notion that In similarly accumulates at the crystal growth interface and inhibits Ga from being trapped in the growing crystal front is not supported, as we have previously speculated.

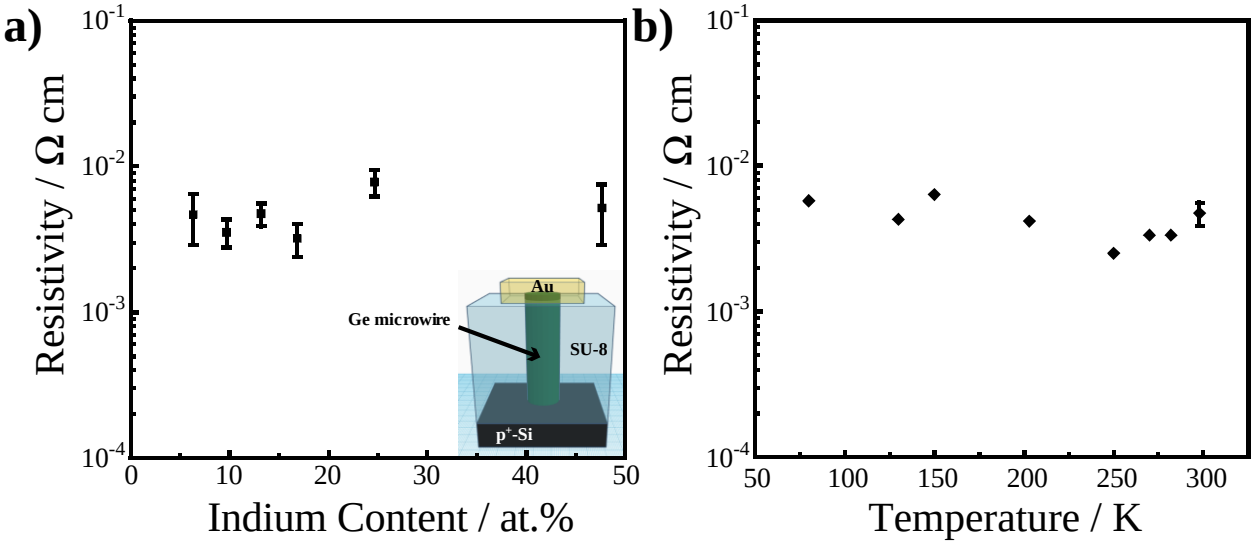

Figure 2.9 a) Resistivity of Ge microwires grown by ec-LLS as a function of $Ga_{1-x}In_x$ composition. All ec-LLS growths were performed in aqueous 0.05 M GeO_2 and 0.01 M $Na_2B_4O_7$ for t = 600 sec at T = 80 °C and E = -1.6 V using a *microdroplet pitch* = 110 μm (N = 50 for each data point). The inset shows corresponding device schematic for individual microwire resistivity measurements. b) Variation of resistivity of Ge microwires grown with $Ga_{1-x}In_x$ (x = 16.8 at. %) as a function of measurement temperature. Conditions for ec-LLS growth were the same as in (a).

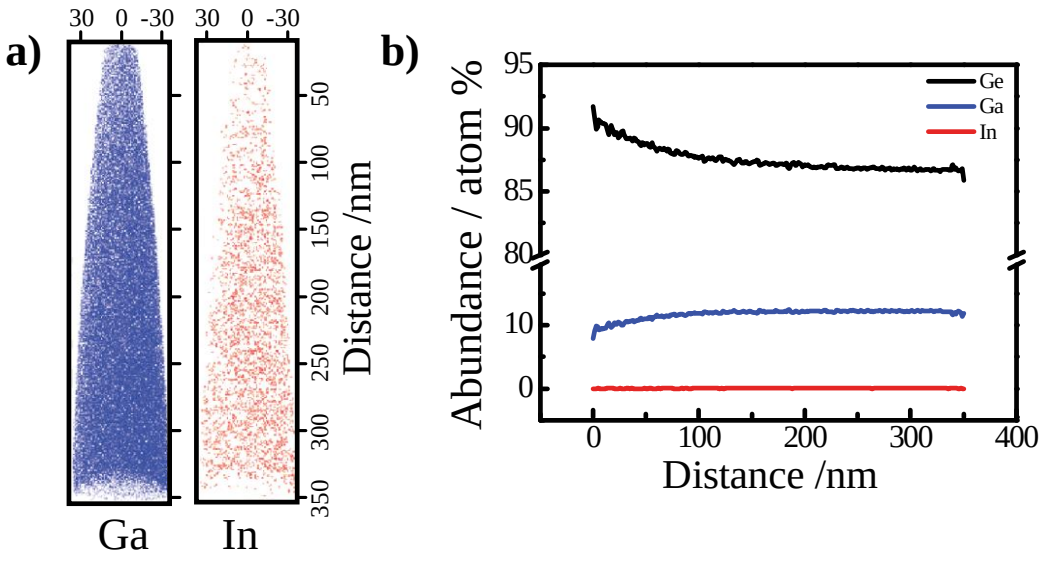

Figure 2.10 Atom probe tomography data showing a) the spatial distribution of Ga and In atoms in a Ge microwire grown by ec-LLS with a Ga_xIn_x microdroplet and b) the average elemental concentrations (atom %) of Ge, Ga and In as a function depth into the interior of the Ge microwire.

Figure 2.10 summarizes results from an atom probe tomography analysis of a Ge microwire grown with a $Ga_{1-x}In_x$ (x = 16.8 at. %) alloy. Figure 2.10a shows the elemental maps for Ga and In in the Ge microwire. In these maps, the top corresponds to the outer surface of the Ge microwire and the bottom corresponds to a region 350 nm inward into the bulk of the microwire along the radial direction. Ga and In are detected throughout the interrogated volume, showing no discernible difference at the surface vs in the bulk of the microwire. Although it would be desirable to use these elemental maps to identify metal impurities occupying substitutional vs interstitial sites, these tomography data do not have sufficient spatial resolution for accurate distinction between these two types. Figure 2.10b presents the average elemental abundances (atom %) of Ge, Ga and In in the sample as a function of depth into the interior of the Ge microwire. Ga and In were both detectable in the as-prepared samples. However, the ratio of Ga and In in the original liquid metal microdroplet was not maintained within the Ge microwire. The In abundance was < 10^{-1} atom %

while the Ga abundance exceeded 10 atom %. This concentration of Ga far exceeds the equilibrium solubility of Ga in solid Ge at room temperature.[60] In fact, the total Ga incorporation is so high that only a small fraction (~0.03-0.3 %) would need to be electrically active in order to impart the hyperdoped characteristics to the Ge micro/nanowires. These findings are consistent with earlier results with In-Cu-Ga liquid metal alloys, where Ga was again selectively enriched in the Ge crystals.[52]

Although the presented results do not yield direct insight on the crystal growth process at the atomic level, the data strongly imply that Group IV crystals grown in liquid metal solvents where Ga is a primary component will likely always show a high level of (p-type) doping. This point is in agreement with a recent demonstration of Ge nanowires grown by the vapor-liquid-solid process with Ga nanodroplets at a slow growth rate (~ 0.2 nm/s), where the analysis suggested these nanowires were still highly doped with Ga.[46] In consideration of the total available evidence, we posit that Ge crystals grown in metal solvents that have a high solid solubility in the semiconductor of interest (e.g. Ga, Sn and Al)[43] will always show a high level of metal incorporation. Since the lattice spacings of ec-LLS grown Ge were consistent with that of crystalline Ge, the crystals were treated as pure Ge rather than a Ge-Ga alloy.[11, 53] Assuming the resistivity−dopant concentration correlations for bulk crystalline Ge holds for the Ge microwires studied here,[61] the average resistivity value measured in this work translates to an approximate active dopant concentration of 10^{-2} atom % (~4-6 × 10^{18} cm^{-3}). This value likely is an underestimate since the carrier mobilities in these polycrystalline microwires are likely lower than in large Ge single crystals. Nevertheless, the point is clear that only a small fraction of the total incorporated Ga is electrically active. The low doping 'efficiency' of the metal impurities likely results from the strongly non-equilibrium growth conditions employed here. The high metal

incorporation in ec-LLS grown crystals suggests ec-LLS operates under the solute trapping mode.[62, 63] In this case, if the mobility of the solvent atoms at the crystal growth front is not fast enough compared to the crystal growth rate, metal solvent atoms can get trapped in the crystal.

Extensive incorporation of metal solvents into semiconductor crystals is not necessarily detrimental. For example, we recently showed that high metal loadings of Ga in Ge microwires imparts a beneficial stability enhancement when the material is used as a Li^+ battery anode.[52] More generally, alloying Ge with metals is one route actively being explored to produce a direct bandgap material with high charge-carrier mobilities.[64-68] Accordingly, the overall utility of Ga as (the major component in) the growth solvent in ec-LLS depends largely on the desired material properties and targeted applications. Nevertheless, the prospect of synthesizing ultra-pure, electronic-grade Group IV semiconductor crystals using Ga-based liquid metal electrodes appears limited. More, non-Ga containing liquid metal compositions ought to be explored for this purpose. In this context there are numerous low melting point liquid metal alloy solders that could prove useful in this regard.[69-71]

2.5 Electrical Characterization of Ge Microwires Grown using Non-Ga Containing Liquid Metals

The previous section specifically details the electrical characterization of ec-LLS grown crystalline materials using Ga-In liquid metal systems. It is seen that Ga tends to incorporate strongly in group IV semiconductor crystals, while the resultant crystals have low levels of In incorporation. Eutectic bismuth indium (21.3 at % Bi and 78.7 at. % In, e-BiIn) is a potentially interesting alternative liquid metal for ec-LLS growth. This alloy has a low melting point of T =

72 °C at ambient pressure and is a commonly used allow for soldering. Figure 2.11 shows the calculated pseudo-binary phase diagram for mixtures of Ge and e-BiIn at standard pressure.[72] Both Bi and In have the tendency to solvate Ge, and have been used individually in their molten state as solvents for liquid phase epitaxial (LPE) growth of group IV semiconductor films at elevated temperatures. Further, the larger crystal radii of Bi (0.117 nm) and In (0.094 nm), relative to Ge (0.053 nm) could impede their unwanted substitution into Ge lattice sites, limiting their potential as unintended dopants. Accordingly, this section presents the electrical characterization on resultant materials produced through ec-LLS using liquid e-BiIn.

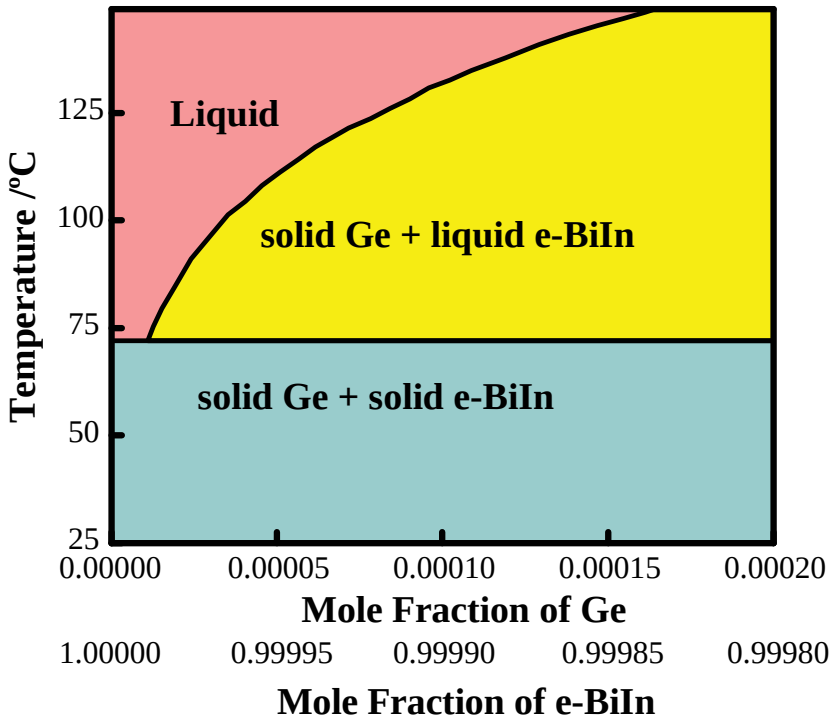

Figure 2.11 Pseudo-binary phase diagram of mixtures of Ge and e-BiIn at standard pressure. The relative fractions of Bi and In are constant as the amount of Ge is varied.

The electrical resistivities of the Ge nanowires were accessed through individual I-V measurements on the wires (Figure 2.12a). After the growth of the Ge nanowires using liquid e-BiIn during the ec-LLS process, the wires were etched in HCl to selectively remove the Bi-In liquid metal cap. The nanowires were mechanically transferred from the growth substrate to a degenerately doped silicon substrate, which was covered with 2 μm of SiO_2 and patterned with metal contact pads (10 nm Ni-Cr and 190 nm Au). Ion beam assisted chemical vapor deposition (FEI Helios Nanolab Dualbeam Focused Ion Beam Workstation) was used to deposit Pt and to establish contact between the ends of the wire and the Au contact pads. Measurements were performed on wires of varying lengths (l = 1.3, 3.1, 5, 7.5 μm) in order to extract the contact resistance and accurately determine the resistivity of the wires. All wires used in this study were from the same growth substrate and identical steps were followed to establish the end contacts, so it is reasonable to assume that the resistivity and contact resistances for all wires are identical. The total resistance for each wire, obtained from the I-V response, is plotted in Figure 2.12b as a function of contact spacing in order to determine the contact resistance Rc and the transfer length L_T. The resistivity of Ge was obtained from the slope of Figure 2.12b and the contact resistance to the nanowires was extracted from the *y*-axis intercept. For the resistivity calculation, it is assumed that the current is carried by the full cross-sectional area of the wire. Since the nanowires are heavily doped, this allows us to meet the above requirement. The electrical resistivity of each individual nanowire was calculated though *eq* 2.2. Further, the specific contact resistivity of the contacts was obtained through *eqs* 2.3 and 2.4,[73]

$$R_T = 2R_c + \frac{\rho_s}{\pi r^2} l \qquad (2.2)$$

$$R_C = \frac{\rho_s L_T}{\pi r^2} \coth(L/L_T) \qquad (2.3)$$

$$L_T = \sqrt{\frac{r\rho_c}{\rho_s}} \tag{2.4}$$

where R_T is the total resistance between a pair of contacts separated by a segment of nanowire of length l, R_C is the contact resistance, r is the radius of the nanowire, L_T is transfer length, L is the length of the contact (L = 1.2 um), ρ_s is the resistivity of the semiconductor and ρ_c is the specific contact resistance. For the device under test, the measured data indicated a ρ_c value of 8.7 x 10^{-6} ohm·cm^2. After accounting for the contact resistance, the resistivity of the ec-LLS crystalline Ge nanowires grown using e-BiIn was between 3 – 6 x 10^{-3} Ω-cm, which corresponds to a active dopant concentration of 2 – 6 10^{18} atoms cm^{-3}.

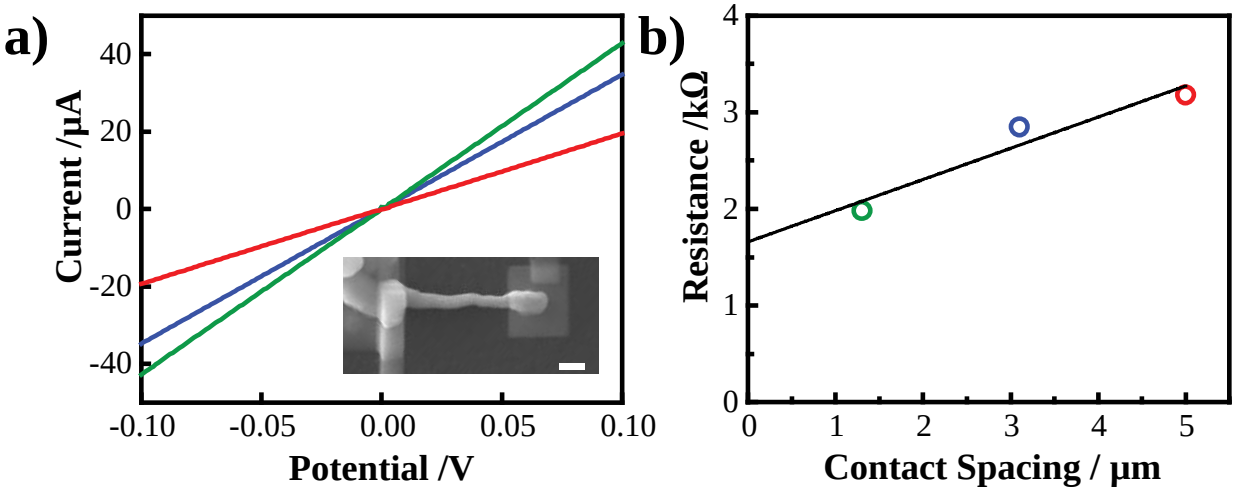

Figure 2.12 a) Current-potential responses for three separate Ge nanowires measured by two contacts. Inset: Scanning electron micrograph of Ge nanowire resistivity measurement. Scale bar: 2.5 μm b) Measured resistance vs contact spacing for the data in (a).

Interestingly, atom probe tomography data acquired on Ge nanowires grown using e-BiIn indicated a measurably high amount of metal incorporation (~ 10 at. %), wherein the ratio of Bi:In in the Ge crystal was approximately equal to that in the e-BiIn alloy used as the liquid metal.[53] In comparison to this, very low levels of In was detected in Ge crystals grown using a Ga-In liquid metal. This indicates the metal incorporation during ec-LLS crystal growth is nuanced and is strongly dependent on the liquid metal solvent system as a whole.

2.6 Conclusion

The data presented here collectively support the following points. Variation in the composition of $Ga_{1-x}In_x$ alloys, when all other electrodeposition factors are held constant, results in no perceptible differences in the conductivity and inferred Ga doping of the resultant Ge microwires. Correspondingly, the negative aspects of Ga as a liquid metal solvent are not necessarily ameliorated when alloyed with another metal. Further, changing the Ga fraction by dilution with In does not affect crystal growth rates or crystal faceting in ec-LLS when all other parameters are held constant. These findings encourage identification of more Ga-free liquid metals when crystalline materials from ec-LLS are needed with higher purity.

Chapter 3

Identifying Critical Factors in the Growth of Germanium Micro/Nanowires by ec-LLS

Acharya, S.; Ma, L.; Maldonado, S. *ACS Applied Nano Materials* **2018** *1* (10), 5553-5561 [†]

3.1 Introduction

The previous chapter explored the option of tuning the liquid metal composition to affect changes in ec-LLS crystal growth. Another important factor in ec-LLS is the crystal growth rate.[40] In ec-LLS, the electrochemical current, *i*, measured during the process defines the rate that zero-

[†] All experiments, data analysis, and figure construction for this chapter were performed by Saurabh Acharya. Stephen Maldonado was the principal investigator for the project.

valent solute is introduced into the liquid metal. When the current is limited solely by the rate of electron transfer to a species dissolved in solution, *eq 3.1* is operative,

$$i = qnk\left(E\right)AC \tag{3.1}$$

where q is the unsigned charge of an electron, n is the number of electrons, A is the electrode area, C is the electroactive concentration of dissolved precursor in solution, and $k(E)$ is the potential-dependent reaction rate constant. In conventional electrodeposition, i is most often adjusted by changing E to affect a change in $k(E)$.[74] However, varying E is somewhat more nuanced in ec-LLS for two reasons. First, a change in the potential of a metal electrode by definition alters the surface charge and correspondingly the interfacial energy at the electrode/electrolyte junction.[74] Since liquid metals are deformable, the change in surface energetics alters the liquid metal shape.[75] This property of liquid metal electrodes is known as electrocapillarity,[76, 77] and could impact crystal growth. Second, low-melting point metals are generally non-noble and can have narrow electrochemical potential 'windows'. For example, metals like In and Ga are easily oxidized at positive potentials while other metals like Bi can be reduced to hydride gas.[78] Although the use of a consistent E value to attain a consistent i across different liquid metals in ec-LLS may not always be possible, changes in either C or A should be.

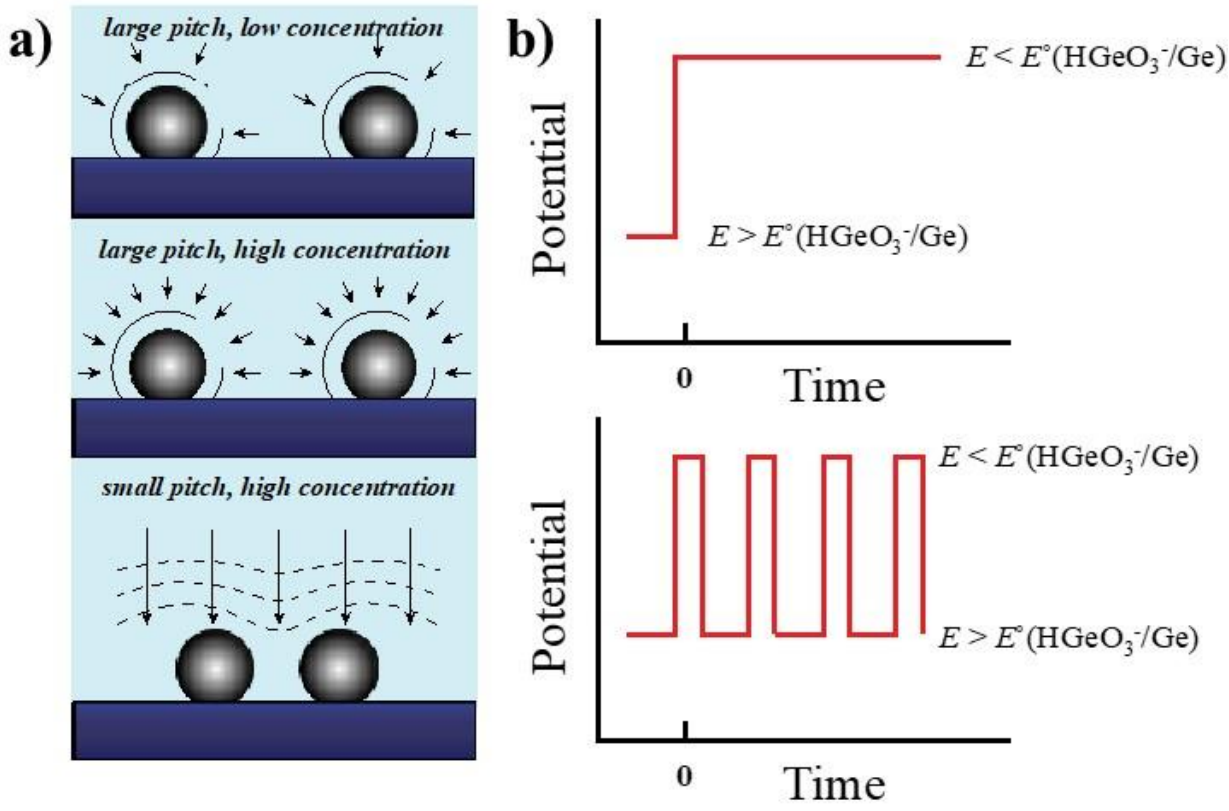

Figure 3.1 a) Three schematic depictions of the flux at widely spaced liquid metal droplet/electrolyte interfaces at (top) low and (middle) high concentrations of dissolved GeO_2 as well as (bottom) for closely spaced liquid metal droplets. b) A graphical comparison of constant potential-time and pulsed potential-time waveforms used for ec-LLS in this work.

Accordingly, in this chapter, the efficacy of two factors that affect ec-LLS is explored. First, the concentration of dissolved GeO_2 and separately the total area over which current is being passed are adjusted to determine if microwire growth rates in Ge ec-LLS can be easily tuned.[51] The latter variable was controlled by adjusting the density/spacing of liquid metal droplets in a regular array (Figure 3.1a).[41] Second, we show that periodic changes in *E* alters how the liquid metal wets the crystalline semiconductors, strongly influencing the crystal growth direction. Specifically, through the use of sequential potential steps (Figure 3.1b), evidence is presented that illustrates the crystal growth is not the same as with a single applied potential step.

3.2 Experimental Methods – Preparation of Liquid Metal Platforms for ec-LLS

Liquid metal microdroplet fabrication and Ge microwire growth was achieved by following steps similar to those mentioned in sections 2.2.1 and 2.2.2. However, in this study, the pitch of each array (defined as the spacing between the centers of two holes) was varied from 20 to 110 μm during the photolithography step. In addition to the array of liquid metal microdroplets, Ga and Ga_xIn_x nanodroplets were prepared for studies described later in this chapter using the methods described below.

3.2.1 Liquid Metal Nanodroplet Preparation

Liquid metal nanodroplets were prepared in two ways. Gallium (Ga) nanodroplets were prepared on n^+-Si(111) wafers by molecular beam epitaxy. Prior to growth, the substrate was cleaned by etching in buffered HF for 45 s to remove native SiO_2 and was immediately transferred into the load-lock of the GEN II MBE chamber. The load-lock was then baked at T = 150 °C for 8 hours prior to substrate transfer into the growth chamber. Once in the MBE growth chamber, the substrate temperature was slowly ramped up to T = 880 °C to calibrate the substrate-heating coil offset. Substrates were then heated at T = 900 °C for 10 minutes in the growth chamber to desorb the SiO_2, at which point a streaky RHEED pattern was observed revealing a smooth Si surface free of SiO_2. Ga droplet deposition was initiated once the substrate temperature was reduced to T = 550 °C and was performed using a constant Ga beam equivalent pressure of 3.7 x 10^{-7} torr for 10 s, corresponding to 7.5 monolayers of Ga.

$Ga_{1-x}In_x$ nanodroplets on n^+-Si (111) wafers were prepared by thermally evaporating e-GaIn using a custom-built thermal evaporator system. In this case too, the native SiO_2 was etched immediately prior to introducing the substrate into the evaporator chamber. The chamber pressure

was kept below $2x10^{-6}$ torr and $Ga_{1-x}In_x$ nanodroplets with diameters d = 60, 100, 300 nm were deposited by controlling the deposition time while maintaining a deposition rate of 2-5 nm/s.[79] Energy Dispersive X-Ray Spectroscopy performed on these nanodroplets determined the composition to be $Ga_{1-x}In_x$ (x = 57.8 ± 8.6 at. %), which could be attributed to the different vapor pressures of In and Ga.[80, 81] Nevertheless, for our purposes, the melting point of these nanodroplets (T ~ 70 °C) is lower than the ec-LLS growth temperature employed.

3.3 Effect of Flux Changes on ec-LLS Crystal Growth

3.3.1 Variation of Concentration of Dissolved GeO_2

The flux of dissolved GeO_2 to each liquid metal microdroplet during ec-LLS growth was modulated by adjusting the concentration of the GeO_2 precursor species in solution. A series of Ge ec-LLS microwire growths were performed where the concentration of dissolved GeO_2 was varied from 0.5 mM to 5 mM to 50 mM. The electrolyte also contained 0.01 M $Na_2B_4O_7$ as well as an inert salt (0.1 M KNO_3) that was necessary to maintain a constant ionic strength and to minimize the resistance drop across the solution for each experiment. The Ge ec-LLS microwire array growths were performed at T = 80 °C and E = -1.6 V using $Ga_{1-x}In_x$ (x = 16.8 at. %) as the liquid metal solvent and a pitch of 110 μm. This pitch was chosen to avoid any interference from neighboring microwires on the diffusion and flux of GeO_2 to each liquid metal microdroplet. The corresponding chronoamperometric data is shown in Figure 3.2. Spikes in the current-time traces correspond to mechanical removal of H_2(g) bubbles from the edges of the film. The currents at t = 720 s are plotted as function of the formal concentration of dissolved GeO_2 (Figure 3.3a). A strong relation between the current and dissolved GeO_2 concentration was observed but the data could

not be well-fit with a linear regression model. Figure 3.3b-d provides tilted-view scanning electron micrographs of as-prepared Ge microwires grown with the three different concentrations of dissolved GeO_2. The variation in the Ge microwire heights with concentration follows Figure 3.3a.

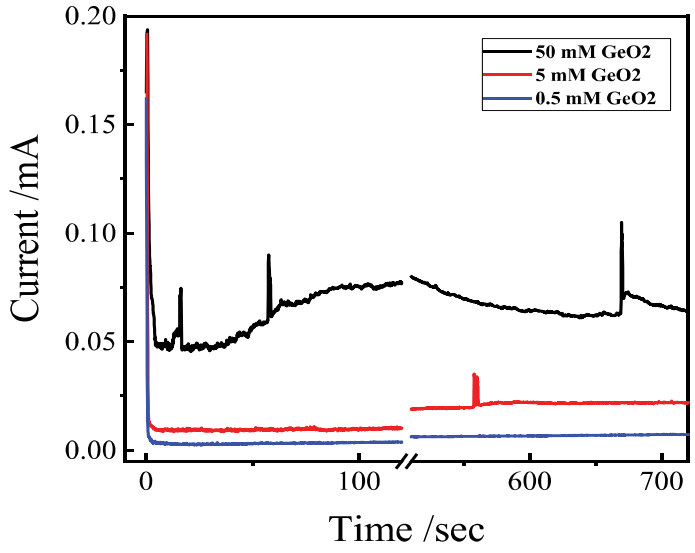

Figure 3.2 Current vs time plots for Ge microwires grown using different concentrations of the GeO_2 precursor in an electrolyte containing 10 mM $Na_2B_4O_7$ and 100 mM KNO_3.

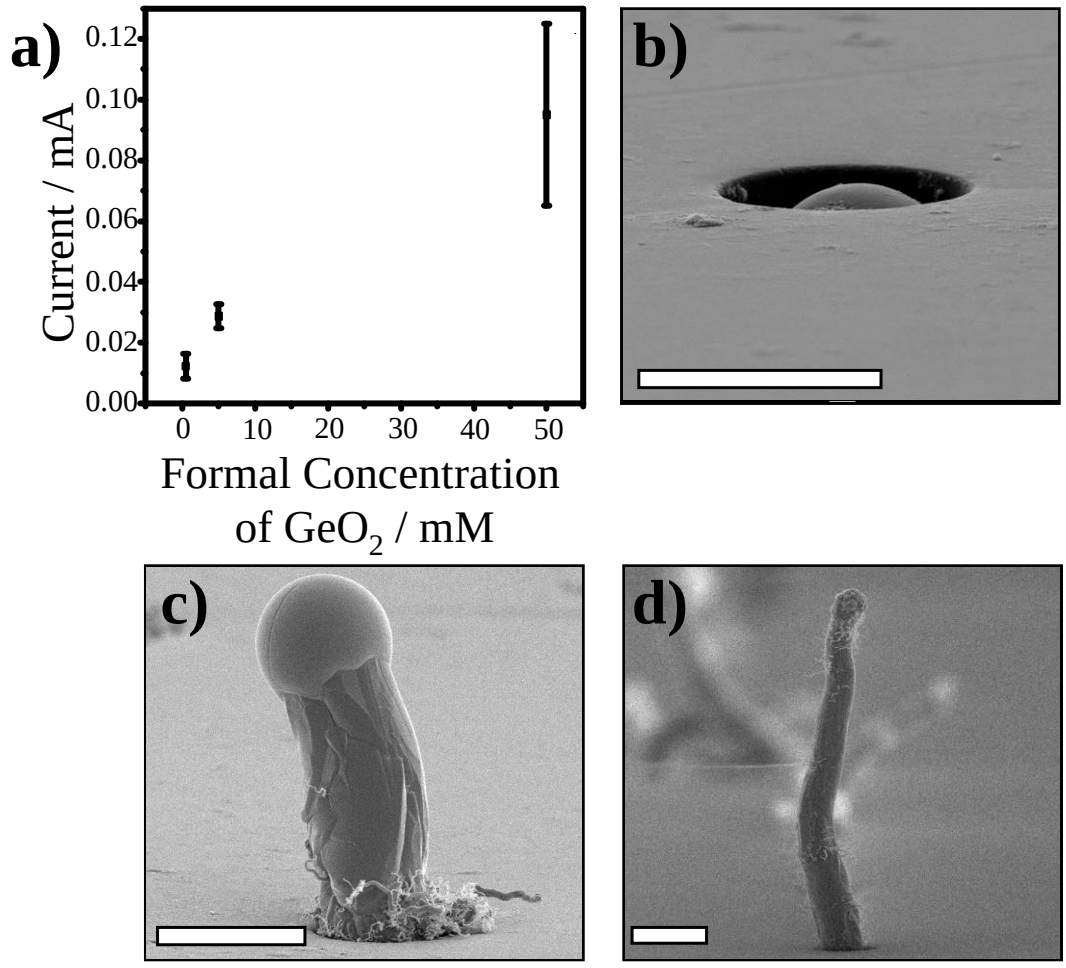

Figure 3.3 a) Current at t = 720 s during ec-LLS experiments performed in an electrolyte containing 0.01 M $Na_2B_4O_7$ and 0.1 M KNO_3 with different concentrations of dissolved GeO_2 at T = 80 °C and E = -1.6 V using $Ga_{1-x}In_x$ (x = 16.8 at. %) as a function of formal concentration of GeO_2. b-d) Tilted cross-sectional scanning electron micrographs of Ge microwires grown by ec-LLS experiments using b) 0.5 mM GeO_2 c) 5 mM GeO_2, and d) 50 mM GeO_2 dissolved. Scale bar: 10 µm.

To compare and to assess the viability of other liquid metals as electrodes in ec-LLS, well-defined and standardized reaction conditions are necessary. As in the case of vapor-liquid-solid processes, nucleation and crystal growth in ec-LLS depends strongly on the rate of Ge introduction into the liquid metal.[82-84] Clearly, large increases in concentration of dissolved GeO_2 affect

correspondingly large differences in current and microwire growth rate. However, the non-linear correlation, coupled with an earlier observations on the complex dependence of the voltammetric response for dissolved GeO_2 reduction with scan rate,[85] strongly imply that the rate-limiting step for this complex redox process is not necessarily a heterogeneous electron transfer between the electrode and a freely dissolved precursor species. For example, pre-adsorption of GeO_2 on electrodes prior to electroreduction has been noted previously.[86] The data here do not specifically implicate an adsorptive mechanism for electroreduction of GeO_2 but do suggest the electron-transfer is more complex than implied by *eq 3.1*.

3.3.2 Variation of Microdroplet Spacing

Experiments were performed to assess how the pitch density affected ec-LLS growths using a constant applied potential. For an isolated liquid metal droplet (i.e. an array with a large pitch), mass transport should follow spherical diffusion. In this case, the maximum flux to an individual droplet can be large.[87] In contrast, the mass transport to a liquid metal droplet with several neighboring droplets (i.e. an array with a small pitch) tends towards planar diffusion since the diffusional fields of each droplet overlap quickly (Figure 3.1a).[88] Electrodepositions were performed with E = -1.6 V for t = 900 s at T = 80 ^{o}C in 0.05 M GeO_2(aq) and 0.01 M $Na_2B_4O_7$(aq) with arrays that had the same microdroplet radius (5 μm) but differed in pitch. Figure 3.4a shows both the steady state current values and the total number of microwells for each array type enclosed in the 0.065 cm^2 region exposed to electrolyte. The overall steady state current was a strong function of the microwell density but did not scale identically as the microwell density. Figure 3.4a shows that the scaling down factor for the steady state current is nearly 5 times smaller than that for the number of microwells in the growth region. As the spacing between the microwells was increased, the flux of dissolved GeO_2 to each liquid metal microdroplet significantly increased.

As a corollary, the length of Ge microwires increased. In Figure 3.4b, the steady state current from Figure 3.4a is normalized to the total number of microwires in the growth region for each array pitch and is plotted as the current per individual microwire as a function of the microwire array pitch. As the charge passed and the current per microwire is a direct measure of the ec-LLS growth rate, Figure 3.4b directly indicates increased ec-LLS growth rates as the microwell array pitch was made larger.

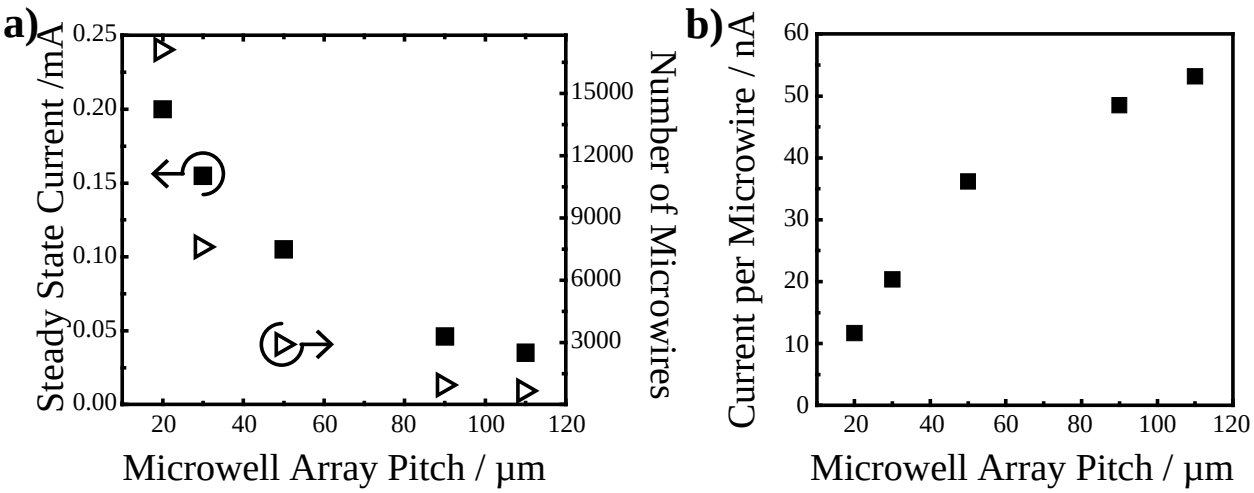

Figure 3.4 a) Steady state current and Ge microwire density as a function of microdroplet pitch. All ec-LLS growths were performed in aqueous 0.05 M GeO_2 and 0.01 M $Na_2B_4O_7$ for t = 900 sec at T = 80 °C and E = -1.6 V using $Ga_{1-x}In_x$ (x = 16.8 at. %). b) The average current passed per microwire as a function of microdroplet pitch.

As an alternative to regulating dissolved GeO_2 concentration to control the flux of GeO_2 to each liquid metal, regulating the current flux by altering the pitch of arrays of discrete liquid metal droplets operating as electrodes in parallel has more appeal. Somewhat paradoxically, the shift from radial to linear diffusion when the pitch decreases results both in an *increase* in the absolute current passed across the array (since the total number of droplets per unit area increases) but a

decrease in the current flux at each individual droplet. Hence, using the pitch of an array to modulate the growth rate of individual microwires without changing any other parameter is effective. The work in this report shows that changing the pitch by roughly a factor of 5 (from 20 to 110 μm) effected a similar change in the current for each individual droplet (11 to 55 nA). For uniform microwires, these currents correspond to microwire growth rates of 15 and 70 nm/s as inferred from the collected electron micrographs. Lower current fluxes are possible with smaller pitches. Arrays of closely spaced, smaller liquid metal nanodroplets may be useful in this regard but are difficult to fabricate by conventional photolithography.

3.4 Potential Step Waveforms for ec-LLS

Although complex, time-dependent waveforms are routinely employed in conventional metal electrodeposition processes,[89-92] they have not been employed in ec-LLS to date. One appeal for ec-LLS with a sequence of short time potential steps is the possibility of 'titrating' discrete and precise amounts of Ge^0 into the liquid metal droplets. If properly regulated, it may be possible to promote nucleation and crystal growth in ec-LLS under defined levels of supersaturation. Knowledge of the precise rates of dissolution, diffusion, nucleation, and crystal growth are needed to design a potential pulse duty cycle with the optimal pulse width and delay time. Presently, such information is lacking. Nevertheless, even with the employed sequence of short potential steps, the data are clear that changes in the potential during growth can strongly impact crystal growth.

Two electrodeposition waveforms were contrasted for Ge ec-LLS: a constant applied potential and a sequence of applied potential pulses. The former case introduces a constant flux of Ge into the liquid metal droplet while the latter titrates discrete amounts of Ge into the liquid metal

droplet. For ec-LLS with a constant applied potential, an applied bias of E = -1.6 V at T = 80 ^{o}C was used with a solution containing 0.05 M GeO_2 and 0.01 M $Na_2B_4O_7$. For ec-LLS with potential pulses, sequential pulses between open circuit and E = -1.6 V with a pulse width of t = 0.8 s and a pulse separation of t = 0.1 s at T = 80 ^{o}C were used in the same electrolyte. The cumulative growth time for the pulsed ec-LLS experiments were determined by accounting for the charging time during each pulse in this electrolyte (measured by performing analogous potential steps in the blank electrolyte).

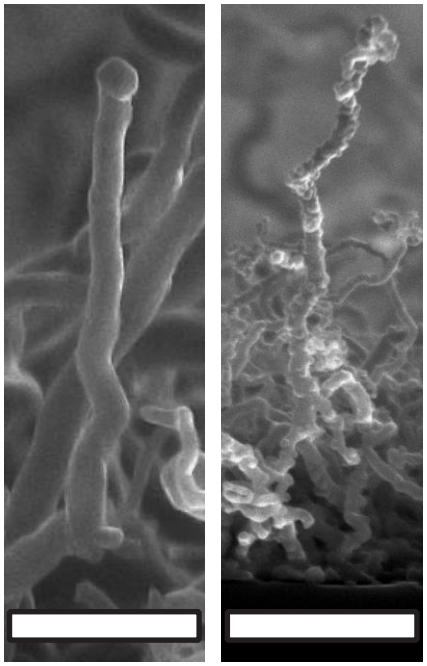

Figure 3.5 Cross-sectional scanning electron micrograph of Ge nanowires grown using a) constant potential and b) pulsed potential Ge nanowire ec-LLS experiments performed in an electrolyte containing 0.05 M GeO_2 and 0.01 M $Na_2B_4O_7$ for a cumulative growth time of t = 720 sec at T = 80 °C using thermally evaporated GaIn nanodroplets on n^+-Si (111) substrates. Scale: 500 nm.

When the two electrodeposition waveforms were applied for the synthesis of Ge microwires using liquid metal ($Ga_{1-x}In_x$) microdroplets, there were no discernable differences between the prepared Ge microwires. Interestingly, applying the same electrodeposition waveforms to liquid metal (Ga and $Ga_{1-x}In_x$) nanodroplets clearly yielded nanowires with different morphologies. Figure 3.5 shows cross-sectional scanning electron micrographs of Ge nanowires prepared by these two ec-LLS waveforms. For these potential step parameters, nanowires were noticeably much less straight. Since these nanodroplet alloys were prepared by thermal evaporation, there was no control over pitch or average separation. Further, slight variation in nanodroplet alloy composition (due to inequivalent rates of evaporation for Ga and In from the source) was noted. As a result, additional potential step experiments were pursued with pure Ga nanodroplets.

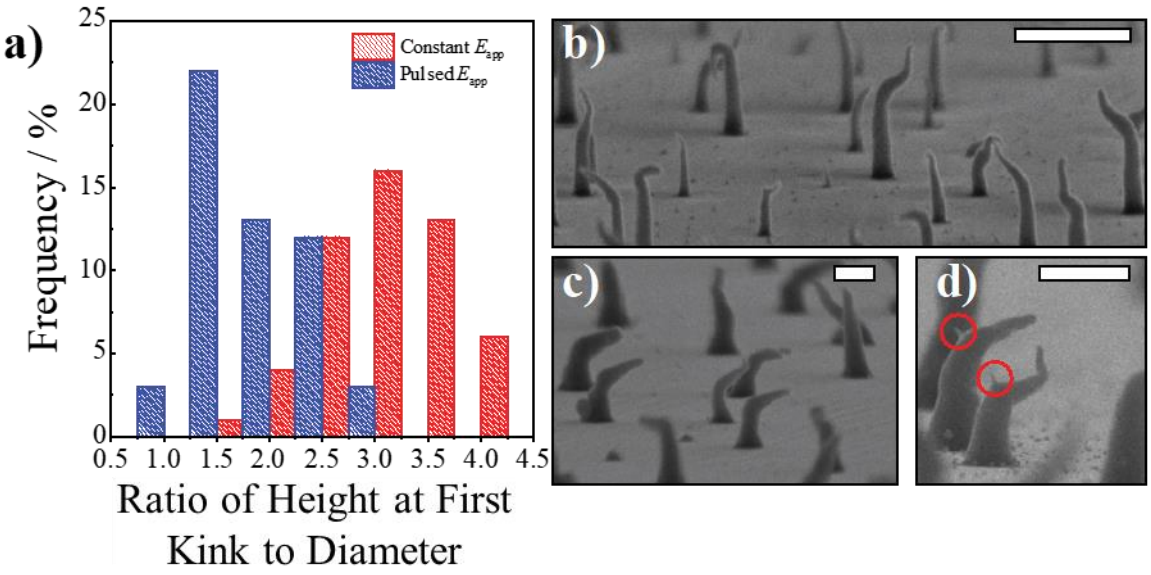

Figure 3.6 a) Distribution of ratio of Ge nanowire height at first kink to diameter for ec-LLS growth with a constant applied potential and a sequence of potential steps. b) Representative tilted cross-sectional scanning electron micrograph of a constant potential Ge nanowire ec-LLS experiment performed in an electrolyte containing 0.05 M GeO_2 and 0.01 M $Na_2B_4O_7$ for t = 60 sec at T = 80 °C and E = -1.6 V using Ga nanodroplets on n^+-Si (111) substrates. c) Representative tilted cross-sectional scanning electron micrograph of Ge nanowires grown with ec-LLS using a sequence of potential steps but otherwise the same conditions as in (b). The potential was stepped from E = 0 V to -1.6 V for 800 ms and then held at E = 0 V for 100 ms for 100 cycles. d) Higher magnification tilted cross-sectional scanning electron micrograph of nanowires in (c) depicting secondary nanowire growth at nanowire kinks. Scale bar: 500 nm.

Figures 3.6b-d show tilted cross-sectional scanning electron micrograph of Ge nanowires prepared by constant potential and pulsed potential ec-LLS methods, wherein MBE-prepared Ga nanodroplets on n^+-Si (111) was used as the growth substrate and the cumulative growth time was restricted to t = 60 s. As reported previously,[11] Ge ec-LLS performed with Ga nanodroplets can yield single-crystalline, epitaxial Ge nanowires that kink during growth but still grow along the [111] direction (i.e. along the surface normal for epitaxy on a Si (111) substrate). Figures 3.6b-d

demonstrate the same phenomenon for both ec-LLS waveforms. However, the relative height at which the first kink was observed was affected by the employed waveform. Figure 3.6a presents summary histograms (N = 150) of the ratios between the height the first kink occurred and the nanowire base diameter. The data indicate that the pulsed waveform consistently yielded nanowires with kinks that occurred at shorter relative nanowire heights. In addition, a propensity for smaller, secondary nanowire growth at some nanowire kinks (Figure 3.6d) was noted. No such observation was seen in multiple samples grown using the constant potential ec-LLS method.

In general, there is significant interest in being able to form nanowires with arbitrary kinks/bends/changes in directions.[93, 94] In vapor-liquid-solid nanowire growths, changes in nanowire growth directions are caused by the introduction of adsorbates/diluents to the reaction chamber.[95-97] We believe the phenomenon observed here is distinct. Specifically, the observed effects on kinking have nothing to do with changes in the composition of either the electrolyte or liquid metal. Instead, we posit that the electrocapillarity of the liquid metal is the determining factor. That is, since changes in E necessarily alters the shape of the liquid metal, the wetting of the nascent crystal must also be affected. Without direct visualization, it is difficult to know exactly the specific extent of deformation of the liquid metals during pulsing. Still, the general concept that liquid metal microdroplets significantly flatten/bow as the potential is varied is well-established, even being exploited as a pumping action in microfluidics.[98-100] We reason that deformation of the liquid metal during changes in E may cause the liquid metal to change which crystalline plane is being wetted. This concept of 'capillary instability' of liquid metal drops during nanowire growth as a mechanism to induce changes in growth directions has been previously modeled and described.[101] However, the response time for shape change is also a function of liquid metal size.[102] This facet may explain why the specific duty cycle affected ec-LLS with

nanodroplets greatly (i.e. their shape change could occur within the pulse time) while ec-LLS with larger microdroplets was nominally unchanged (i.e. the pulse time was too short to effect a substantial shape change).

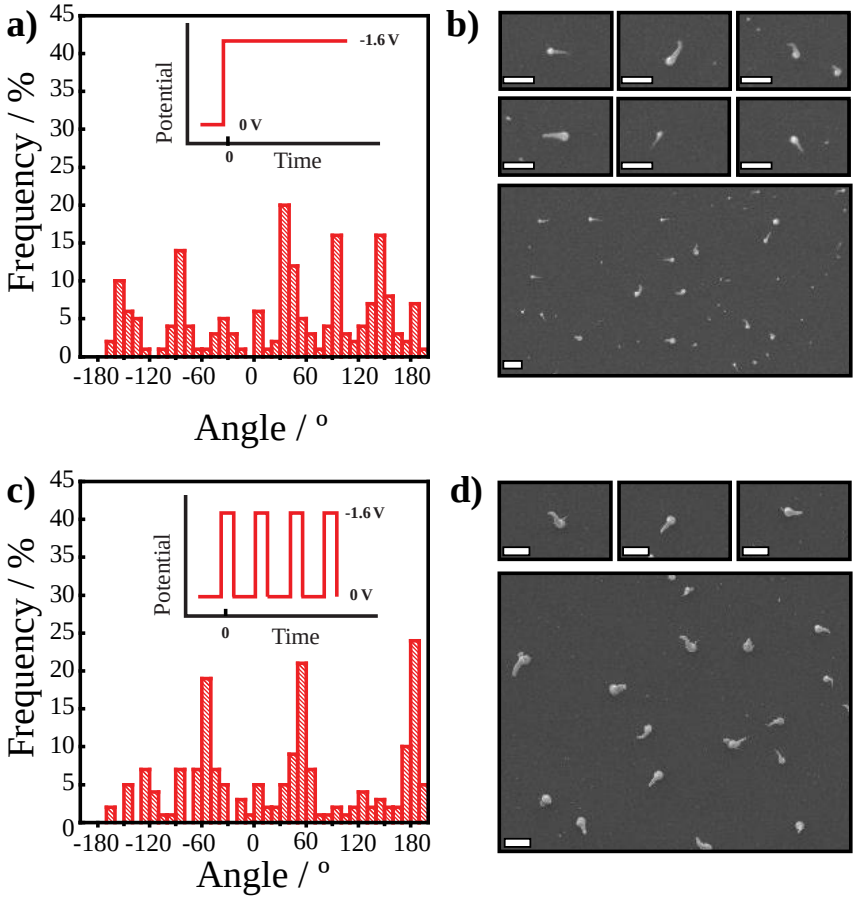

Figure 3.7 a) Distribution of Ge nanowire orientations after the first kink for Ge nanowire ec-LLS with a constant applied potential. b) Representative plan-view scanning electron micrographs of Ge nanowires shown in Figure 3.6b. Scale bar: 400 nm. c) Distribution of Ge nanowire orientations after the first kink for Ge nanowire ec-LLS with a sequence of discrete potential steps. d) Representative plan-view scanning electron micrographs of Ge nanowires shown in Figure 3.6c. Scale bar: 1 µm.

A further observation regarding the effect of the ec-LLS waveform on kinking was noted. For longer ec-LLS nanowire depositions, the orientation and growth directions of the Ge nanowires after kinking was examined. Figures 3.7b and 3.7d show top-down view scanning electron micrographs of Ge nanowires grown with a constant potential and a sequence of applied potentials respectively. As evident in Figures 3.7b and 3.7d, the Ge nanowires were predominantly oriented at a small number of angles after kinking. Figures 3.7a and 3.7c show corresponding histograms where the frequency of observations is plotted as a function of nanowire growth angle. While the principal <111> direction is normal to the image plane, the other three <111> directions are separated by 120° from this viewing perspective. Accordingly, nanowire kinking that causes the growth direction to shift to one of these other [111] directions would be expected to occur equally at just these three angles. Figure 3.7c shows this scenario occurs only when ec-LLS is performed with potential pulses. When the potential was constant, nanowire growth predominantly occurred at 6 discrete angles separated by 60°, implying an inversion of symmetry and growth along [$\bar{1}\,\bar{1}\,\bar{1}$] directions.

Presently, it is not clear why pulsed ec-LLS apparently prevented the occurrence of twinning defects that would cause an inversion of the [111] growth directions, but such results are strongly encouraging that potential steps can affect more than just the growth direction of nascent crystallites. More work is necessary to determine the extent that this effect is specifically operative and the degree to which it can be deliberately employed.

3.5 Highly Efficient Solution Processed Optical Absorbers across the Visible-to-Infrared Spectrum

The various ec-LLS approaches presented in this thesis all yield hyperdoped-Ge crystalline materials. Although it is premature to conclude that high metal incorporation is inevitable in ec-LLS, it is nevertheless a persistent theme with the liquid metals and non-equilibrium growth conditions employed so far. However, residual metal content in crystalline semiconductors is acceptable for certain passive photonic applications. Various applications in optics and optoelectronics require efficient, low-cost, and compact optical absorbers and Ge is a suitable candidate for absorbers that spread across the visible-to-infrared spectrum. Previous reports of Ge nanowire based optical absorbers make use of the top-down fabrication approach or other energy and cost intensive approaches.[103, 104] Ec-LLS Ge nanowires in its current state is an interesting process for passive optical absorbers. Here, we present solution processed vertical Ge nanowire films that exhibit excellent light absorbing properties.

Ge nanowires were prepared by the ec-LLS process in an aqueous solution at T < 95 C with Ga-In liquid metal droplets. In order to increase the density of Ga-In droplets and the resultant Ge nanowire film, evaporation of Ga-In droplets was developed in a custom home-built thermal evaporator (Figure 3.8). Eutectic Ga-In (75-25 wt. %) was used as the source material, while a variety of substrates including n^+-Si, FTO, Cr, and PEDOT-PSS were used for this study. In order to tune the Ga-In droplet diameter and spacing during the thermal evaporation, the deposition time and working distance (distance between the source and substrate) were used as control parameters. Figure 3.9 illustrates scanning electron micrographs of Ga-In droplets with diameters of 1 μm, 300 nm, and 100 nm, illustrating fine control over the deposition parameters.

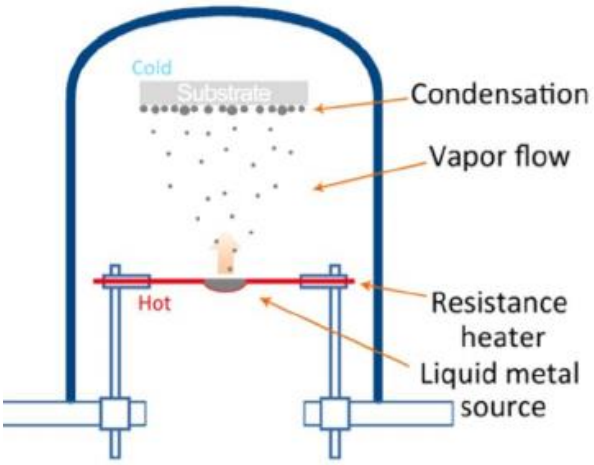

Figure 3.8 Schematic of the custom home-built thermal evaporator for Ga-In deposition (Martin-Palma, R. J.; et al. *Engineered Biomimicry*, 2013, pp 383–398).

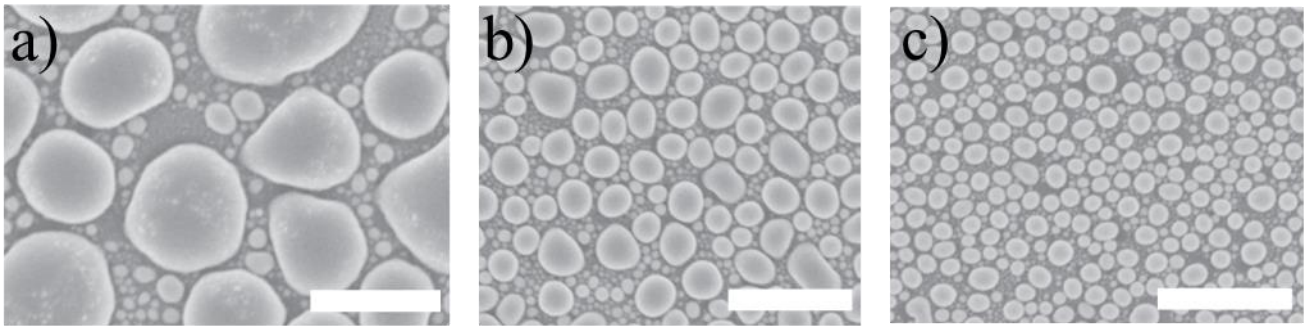

Figure 3.9 a-c) Top-view scanning electron micrographs of Ga-In droplets thermally evaporated on Si substrates for different deposition times. Scale bar: 1 µm.

Due to the difference in vapor pressures of Ga and In,[80, 81] the composition of the evaporated $Ga_{1-x}In_x$ droplets was measurably different (x = 57.8 ± 8.6 at. %) compared to the

eutectic composition. Nevertheless, the melting point of the Ga-In droplets was low enough to perform ec-LLS growth at temperatures less than 80 °C. Ec-LLS growth was performed using a potential of E = -2 V vs. E(Ag/AgCl) for t = 1 minute, while all other parameters were the same as described in Section 2.2.2.

The voltammetric responses in Figure 2.4 clearly depict that in addition to Ge^{4+} reduction, there is an enhanced propensity for H^+ reduction at more negative potentials. A potential of E = -2 V vs. E(Ag/AgCl) was purposely selected in order to increase the H_2 (g) evolution during ec-LLS growth, which creates a degree of disorder in the Ge nanowire array being grown. This can be seen in the tilted scanning electron micrograph of Figure 3.10, where the density of the nanowire array decreases gradually from the bottom to the top. This translates to a cumulative effect of a graded refractive index profile for the Ge nanowire film, potentially leading to reduced reflection or enhanced light trapping in this structure.

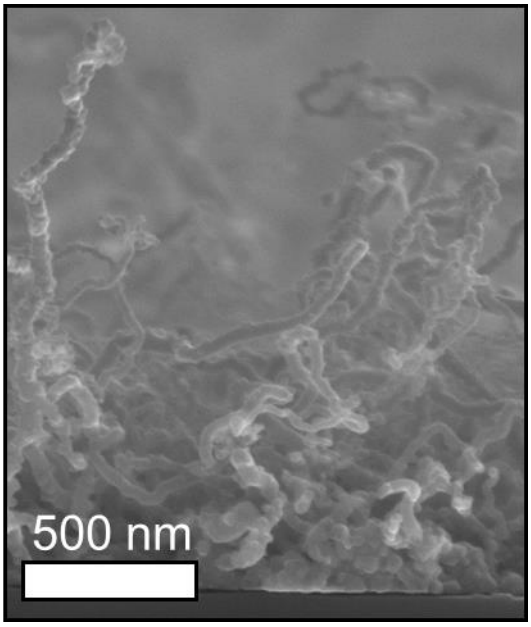

Figure 3.10 Tilted-view scanning electron micrograph of Ge nanowires grown using Figure 3.9c as the growth substrate. Scale bar: 500 nm.

Preliminary results indicated the Ge nanowire films have an absorption > 90% in the 300-1900 nm wavelength range. The broadband absorption performance of the Ge nanowire films was further optimized by varying the diameter of the In-Ga droplets as well as the spacing between these droplets (Figure 3.11). The diffused and specular reflectance of the Ge nanowire film was measured using UV-Vis spectrometer coupled with an integrating sphere (Cary 5000, Varian). The signal noise in the reflectance plot in the near-infrared (NIR) region corresponds to detector error. The optimized Ge nanowire structures demonstrated a maximum absorption of 93% from the visible to the NIR range. The light absorption efficiency can be further enhanced easily by depositing an anti-reflection layer, which is a standard practice for reflection-based photonic devices.

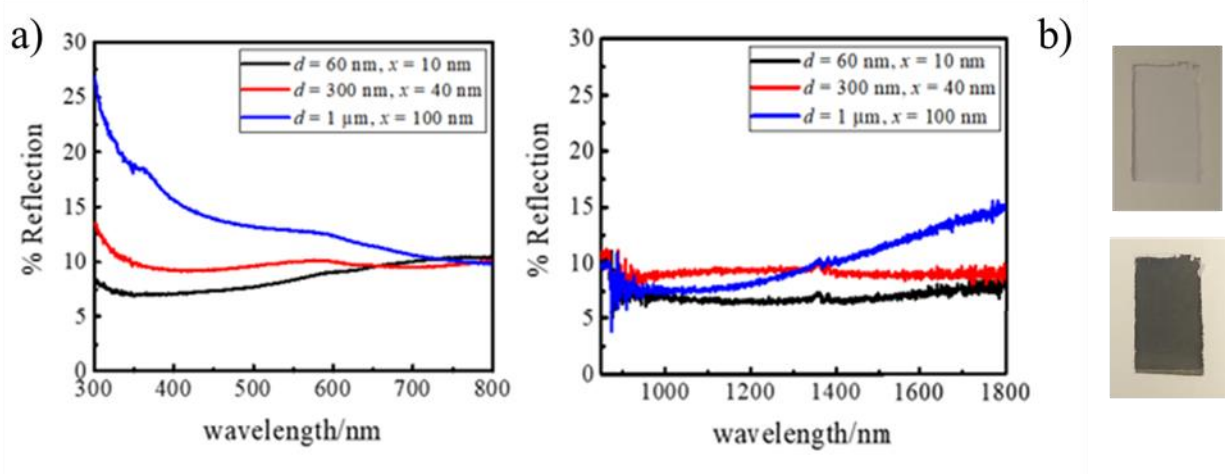

Figure 3.11 a) Total reflection spectra of ec-LLS grown Ge nanowire films on FTO substrates for a variety of Ga-In nanodroplet diameter and spacing conditions. b) Photograph of FTO substrate on a white paper before and after being coated with a Ge nanowire film with Ga-In droplet diameter, d = 60 nm and Ga-In droplet spacing, x = 10 nm. Sample size is 2 cm x 3 cm.

Highly-absorbing Ge nanowire films were deposited on a variety of substrates for two reasons: (1) to demonstrate compatibility of this approach with semiconductor, metal, ceramic, polymer substrates (2) to examine the influence of the substrate on the optical performance of the Ge nanowire-based absorbers. From the reflection spectra of the samples prepared on Si and FTO substrates (Figure 3.12), it is evident the excellent light absorption properties does not arise from the absorptive nature of the Si substrate but is rather inherent to the Ge nanowire film deposited.

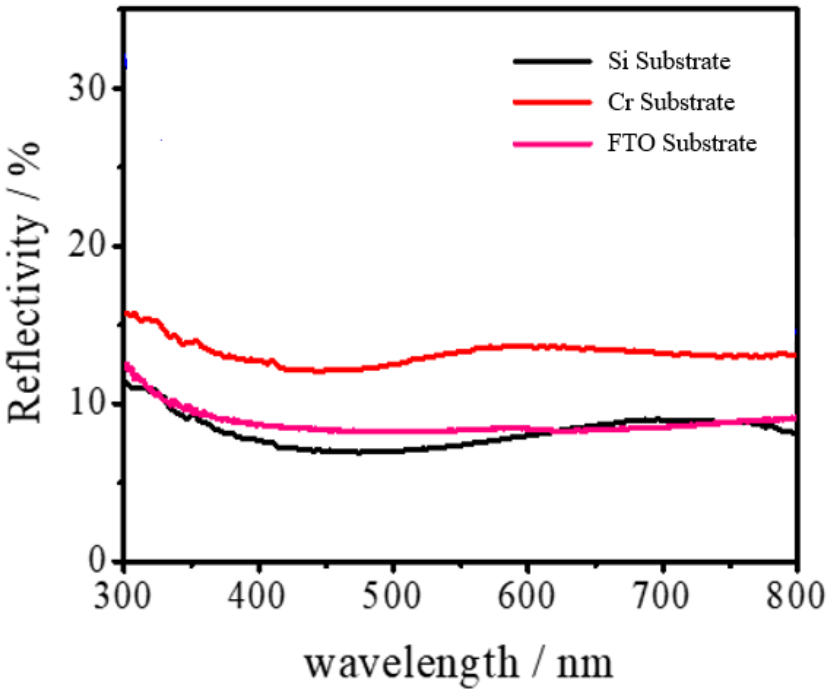

Figure 3.12 Total reflection (diffused + specular) spectra of ec-LLS grown Ge nanowire films on a variety of substrates.

The strategy presented in this section offers a lithography-free approach to coat any substrate black at ambient conditions, without using any energy or cost intensive processes. The results presented here are the highest ever reported value for purely Ge-based absorber films, while

the thickness of the Ge nanowire films is also approximately ten times thinner than previous reports.[104, 105] Low-cost, light-weight broadband absorbers presented here are an exciting option for solar-steam generation and desalination devices,[106-108] textiles for radiation control,[104, 109] cloaking,[110] and potentially also for imaging applications.[103]

3.6 Conclusion

Changes in either the concentration of the precursor species in solution or the current flux to the liquid metals in ec-LLS strongly alter the growth rate, even when the applied potential is held constant. Specifically for microwire and nanowire growth, the packing density of liquid metal droplets is a simple and direct determinant of the crystal growth rate. Also, the use of complex waveforms in ec-LLS can strongly perturb crystal growth, particularly at the nanoscale. Switching the Ge ec-LLS process from a steady-state to a pulsed growth mode affected the crystallinity and morphology of the resultant Ge nanowires. The data suggest pronounced effects on the wetting of crystal faces by the liquid metal when its volume is small. Accordingly, complex potential-time (or current-time) waveforms represent another possible handle in controlling material properties synthesized by ec-LLS. The collective results here motivate future work in expanding the fidelity of ec-LLS for tailored microwire and nanowire growth.

Chapter 4

Electrodeposition of Large Area, Angular-Insensitive Multilayered Structural Colors

Acharya, S.*; Ji, C.*; Yamada, K.; Maldonado, S.; Guo, L. J. *ACS Appl. Mater. Interfaces* **2019**, 11, 32, 29065-29071 †

4.1 Introduction

Color filters that selectively transmit or reflect visible light are highly desired in a wide variety of applications, including optical displays,[111, 112] colored printings,[13, 113, 114] aesthetic decorations,[18, 115] and energy harvesting.[116-121] In recent years, structural colors based on optical interference effects of nanostructures have received increasing interest due to their various advantages over traditional colorant-based pigmentations, such as, high brightness, ultra-compactness, easy manufacturability, and long-term stability.[122]

† All experiments, data analysis, and figure construction for this chapter were performed by Saurabh Acharya. Chengang Ji performed the refractive index measurement, angle-dependent reflectance measurement, and all simulations for this chapter. Kaito Yamada acquired the AFM images. L. Jay Guo and Stephen Maldonado were the principal investigators for the project.

In this chapter, a simple, inexpensive, and non-toxic bench-top electrodeposition process for the fabrication of structural color filters at ambient conditions is reported. This process avoids the need for expensive vacuum-based equipment and is compatible with highly non-planar substrates of arbitrary shape, size and roughness. Asymmetric metal-dielectric-metal (MDM) Fabry-Pérot (F-P) cavities have been achieved by sequential electrodeposition of smooth gold, thin cuprous oxide, and finally thin Au on conductive substrates, forming an effective optical cavity. Different colors of high brightness are achieved by simply tuning the thickness of the electrodeposited middle cavity layer, while constraining the thickness of the top and bottom Au films. This work is the first demonstration of solution-processed, electrodeposited metal-dielectric-metal film stacks and highlights the clear advantages of this approach over traditional deposition or assembly methods for preparing colored films.

4.2 Overview of New Methods for Structural Color Generation

Chapter 1 listed the traditional schemes and methods being used to produce structural colors and it also made it evident that new schemes need to be developed to expand and open-up new avenues for the use of structural colors. Three-dimensional (3D) photonic crystals employing self-assembled nanoparticles to generate colors have been explored.[123-128] However, substrates of high flatness and smoothness are demanded for self-assembled processes to obtain continuous and uniform coating, which puts a limitation on the use of these methods for many applications.[129, 130] In addition, the use of this approach to generate pigment flakes for decorative paints is hindered by the fact that the ordered nanoparticle films could get disordered or disassembled while being ground into flakes, which would result in the change or even the disappearance of the color.

In comparison, electrochemical methods can be simultaneously performed under mild conditions and with the unique advantage of being applicable to objects of arbitrary shape and size. Electrodeposition specifically affords conformal film coatings on substrates with both micro- and macro- roughness[131-133] since film nucleation[134, 135] and growth rate are readily controllable in real-time by regulation of the applied potential/current.

In this work, we present data describing a simple and inexpensive procedure for the fabrication of structural color filters at ambient conditions and $T \leq 50$ °C using electrodeposition of metal and dielectric thin films[136, 137]. Unlike simple structural color films based upon uncapped oxide films,[138-140] the MDM structures demonstrated here show several fundamental and practical advantages. First, due to the high refractive index of Cu_2O (Figure 4.6a), the color of the resultant electrodeposited MDM films is angle-insensitive at viewing angles up to ± 60°. Second, the electrodeposition method shown here produces MDM structural colors across the CMY color space with superior brightness. Third, the electrodeposition process is comparatively rapid, performed without expensive ancillary process equipment, and compatible with irregular, curved substrates. Specifically, we use a fully aqueous, non-toxic electrolyte is utilized that is free of any harmful pollutants. Fourth, the films are strongly adherent on stainless steel substrates.

4.3 Electrodeposition of Au and Cu_2O Thin-Films

4.3.1 Chemicals, Materials and Substrate preparation

Acetone (ACS grade, Fisher Scientific), methanol (ACS grade, Fisher Scientific), 2-propanol (ACS grade, Fisher Scientific), buffered hydrofluoric acid (BHF, Transene Inc.), 49% hydrofluoric acid (HF, Transene Inc.), gold (III) chloride trihydrate ($HAuCl_4 \cdot 3H_2O$, >99.9%

Sigma-Aldrich), potassium sulfate (K_2SO_4, ACS grade, Fisher Scientific), potassium chloride (KCl, ACS grade, Fisher Scientific), sulfuric acid (H_2SO_4, 0.1 M eluent concentrate for IC, Sigma-Aldrich), copper (II) sulfate pentahydrate ($CuSO_4 \cdot 5H_2O$, ACS grade, Avantor), citric acid (>99.5% ACS grade, Sigma-Aldrich), sodium hydroxide (NaOH, >98% ACS grade, Sigma-Aldrich), indium (99.99%, Gallium Source), and gallium (99.999%, Alfa Aesar) were used as received. Degenerately doped n^+-Si(111) wafers with a ± 0.5 º miscut (0.525 ± 0.020 mm, $\rho < 0.007$ Ω·cm, Addison Engineering, Inc.) were diced and used as substrates. Deionized (DI) water with a resistivity >18.2 MΩ·cm was used throughout.

Both n^+-Si(111) substrates and stainless-steel spoons were degreased by sequentially sonicating for 5 minutes each in acetone, methanol, isopropyl alcohol, and water, and then dried under a nitrogen (N_2) gas stream. H-terminated Si(111) surfaces were prepared by immersion of the Si substrates in 5% HF for 30 seconds, soaking in DI water at T = 95 °C for 20 minutes, and then etching sequentially in 5% HF and BHF for 30 seconds each. Etched Si substrates were then rinsed with water, dried under a N_2(g) stream, and were immediately used for the electrodepositions. The stainless-steel spoons were used as working electrodes directly after the initial degreasing steps without any HF etch steps.

4.3.2 Electrodeposition of Bottom Au Layer

All electrochemical depositions were performed in a three-electrode cell in lab ambient and $T \leq 50$ °C. Computer controlled potentiostats (CHI760C, CH Instruments and Solartron Analytical 1287A, AMETEK Scientific Instruments) were used throughout. A platinum mesh counter electrode was used for all electrodepositions whereas multiple reference electrodes were employed as dictated by the *p*H of the electrodeposition solution.

Since all three layers are electrodeposited for the structural colors presented in this work, the surface roughness is expected to gradually increase as we sequentially electrodeposit each layer. However, high smoothness and uniformity are required to obtain highly reflective structural colors. Thus, appropriate care was taken to ensure low surface of these electrodeposited films and epitaxial growth of ultra-smooth Au on Si (111) was specifically used to reduce the roughness of the subsequent dielectric and metal layers. Epitaxial growth of Au on H-terminated Si was first demonstrated by Allongue and co-workers [141] and an interface model using coincident site lattices has been used to explain the epitaxial growth of Au on Si even though this system has a -24.9% mismatch of lattice parameters. As expected, it was shown that Au films deposited on Si (111) were smoother than those deposited on Si (100) and Si (110).[142, 143] In addition to the H-terminated surface and Si (111) orientation, Si substrates with a 0.5º miscut angle were utilized wherein the staircase structure due to the miscut results in additional nucleation sites for Au growth.[141, 144]

An aqueous stock solution of 0.1 mM $HAuCl_4 \cdot 3H_2O$, 1 mM KCl, and 100 mM K_2SO_4 was prepared for Au electrodeposition. For Au electrodeposition on n^+-Si (111) and stainless-steel, a portion of this stock solution was separated and 1 mM H_2SO_4 was added to it to adjust the pH to ~3.[141, 143] An aqueous Ag/AgCl (sat. KCl) electrode was employed as the reference electrode for these solutions. Ohmic contact to the Si substrate was made by applying eutectic gallium-indium to the tip of the wafer and clipping the working electrode of the potentiostat to this region. For the case of stainless-steel spoons, the working electrode of the potentiostat was directly clipped on to the end of the spoon. The current-potential characteristics for both an n^+ Si (111) substrate and a stainless-steel spoon immersed in an aqueous solution of 0.1 mM $HAuCl_4 \cdot 3H_2O$, 1mM H_2SO_4, 1 mM KCl, and 100 mM K_2SO_4 are shown in Figure 4.1. These measurements were performed at T = 35 °C. The hump at E = -0.8 V vs. Ag/AgCl is associated to O_2 reduction. Based on these

voltammetric responses, Au electrodeposition on n^+ Si (111) substrates and stainless-steel spoons were determined based on these voltammetric responses. The Si substrate was prepolarized by applying a potential of E = -1.9 V vs. E(Ag/AgCl) and was then immersed into solution. This prepolarization step was necessary to avoid electroless plating of Au and the formation of a native oxide layer on Si that could prevent further epitaxial Au growth. A potential of E = -1.45 V vs. E(Ag/AgCl) was selected for Au electrodeposition on the stainless-steel spoons in order to avoid excessive hydrogen evolution at more negative potentials.

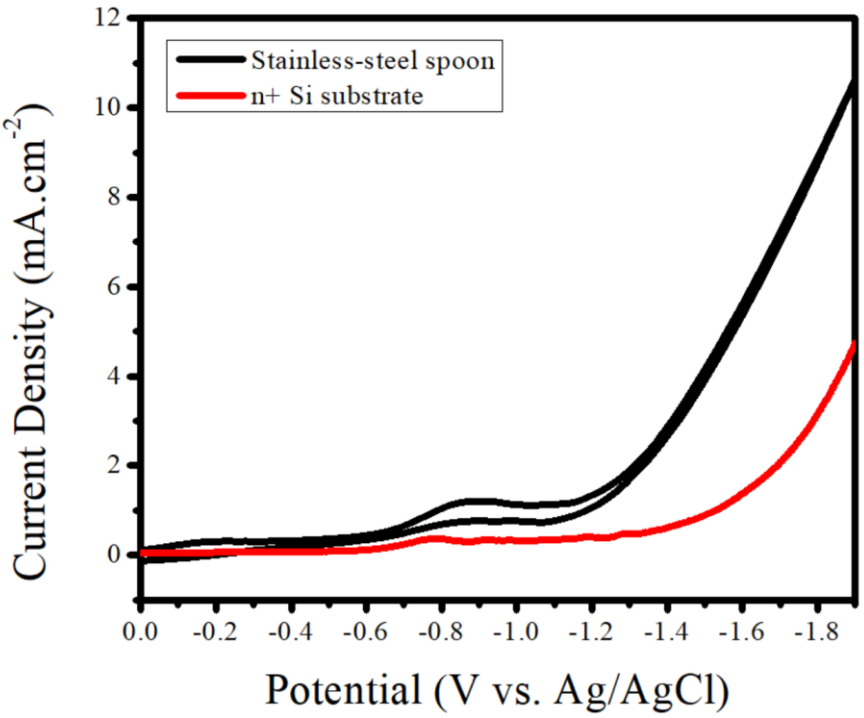

Figure 4.1 Cyclic Voltammetry response of an n^+ Si (111) electrode and a stainless-steel spoon electrode in 0.1 mM $HAuCl_4 \cdot 3H_2O$, 1mM H_2SO_4, 1 mM KCl, and 100 mM K_2SO_4. Scan rate = 50 mV s^{-1}.

For all samples, electrodepositions performed for 40 minutes at T = 35 °C with a stirred solution yielded uniform ~ 40 nm thick Au films. Au film growth rates of ~1 nm/min were determined from the as-deposited films using spectroscopic ellipsometry and cross-sectional scanning electron microscopy (SEM). Faster growth rates at this potential were possible by increasing the concentration of $HAuCl_4 \cdot 3H_2O$ if the *p*H was separately maintained. Figure 4.4a shows atomic force microscopy (AFM) measurements of a representative electrodeposited Au thin-film (40 nm thick) on n^+-Si(111). The root-mean-square roughness (R_{RMS}) was ~1.4 nm, with an arithmetic average roughness (R_a) of ~1.1 nm.

4.3.3 Electrodeposition of Cu_2O Layer

The electrodeposition of Cu_2O on these Au films was performed galvanostatically in an alkaline solution where Cu(II) hydroxypropane-1,2,3-tricarboxylate (i.e. copper citrate) was generated by addition of 0.4 M $CuSO_4 \cdot 5H_2O$ and 1.6 M citric acid ($H_3C_6H_4O_6OH$).[145] NaOH was slowly added to this solution to raise the pH to ~10.9. A mercury sulfate (sat. K_2SO_4) electrode was employed as the reference electrode in the three-electrode cell, but all stated potentials are reported with respect to E(Ag/AgCl). Kapton tape was used to define the total active area of the working electrodes in contact with the solution. The applied cathodic current density, j, dictated whether Cu_2O (j = 0.1 mA/cm^2) or Cu ($j \geq$ 1 mA/cm^2) was produced,[146]

$$[Cu_2(C_6H_4O_7)_2]^{4-} + 2e^- + H_2O \rightarrow Cu_2O + 2C_6H_4O_6OH^{3-} \quad (4.1)$$

$$[Cu_2(C_6H_4O_7)]^{4-} + 4e^- + 2H_2O \rightarrow 2Cu + 2C_6H_4O_6OH^{3-} + 2OH^- \quad (4.2)$$

Care was taken to avoid producing any Cu^0 in the Cu_2O films by tuning the cathodic current density between 0.05 to 0.1 mA/cm^2 to ensure the potential measured during electrodeposition did not exceed E = -0.41 V vs. E(Ag/AgCl). Electrodepositions performed at T = 50 °C and under convection resulted in uniform Cu_2O electrodeposition (~ 0.05 – 0.1 nm/s) and a measured potential of E = -0.16 V to -0.41 V vs. E(Ag/AgCl). Representative chronopotentiometry plots for three different thicknesses (20, 40, 60 nm) of electrodeposited Cu_2O are presented in the Figure 4.2. The consistent shape and form of these plots highlights both the repeatability and consistency of the Cu_2O electrodepositions and the ability to readily use time as the sole variable to determine thickness.

AFM measurements of a 45 nm thick Cu_2O film (used for the magenta device) electrodeposited on the same Au film in Figure 4.4a are shown in Figure 4.4b. The R_{RMS} and R_a values were slightly larger (4.2 nm and 3.3 nm, respectively) but nonetheless more than low enough to maintain a mirror-like appearance.

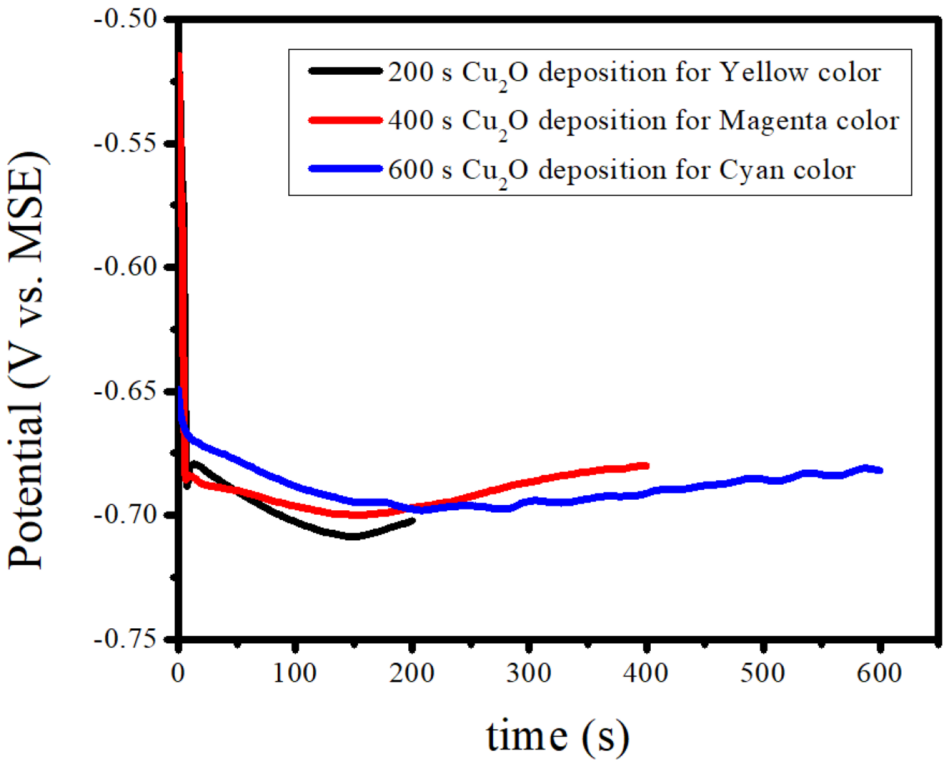

Figure 4.2 Chronopotentiometry plots of different thicknesses of Cu_2O thin-films electrodeposited on Au/n^+ Si (111) electrodes in an electrolyte containing 0.4 M $CuSO_4 \cdot 5H_2O$ and 1.6 M citric acid at T = 50 °C and using a current density of j = 0.1 mA/cm^2.

4.3.4 Electrodeposition of Top Au Layer

The electrodeposition of a thin metal layer of good optical quality on top of a dielectric is very challenging. For example, the intent to use the same bath as the Cu_2O electrodeposition and just grow a capping Cu^0 layer[145, 147-150] on top by increasing the current density to produce Au/Cu_2O/Cu MDM stacks or even Cu/ Cu_2O/Cu MDM stacks failed to produce smooth Cu with good optical property. There is precedent for this approach in previous reports of electrodeposition of epitaxial metal-metal oxide layers by pulsed currents.[145, 147-150] However, while Cu^0 layers were readily formed, all samples yielded Cu^0 films that were of poor optical and electrical quality,

showing significant lossy character and approximately 100x lower conductivity than thermally evaporated Cu films of similar thickness. Even though energy dispersive (EDS) and X-ray diffraction (XRD) spectra showed no detectable impurities and pure Cu character, the optical and electrical properties could not be improved for a film with a thickness below 20 nm. Annealing these Cu films in Ar (g) at T = 200 °C increased the surface roughness of these films (Figure 4.3), possibly due to the diffusion of entrapped air/solvent in nanoscale voids in the Cu film. Accordingly, electrodeposited Cu thin films were not pursued further using this electrolyte.

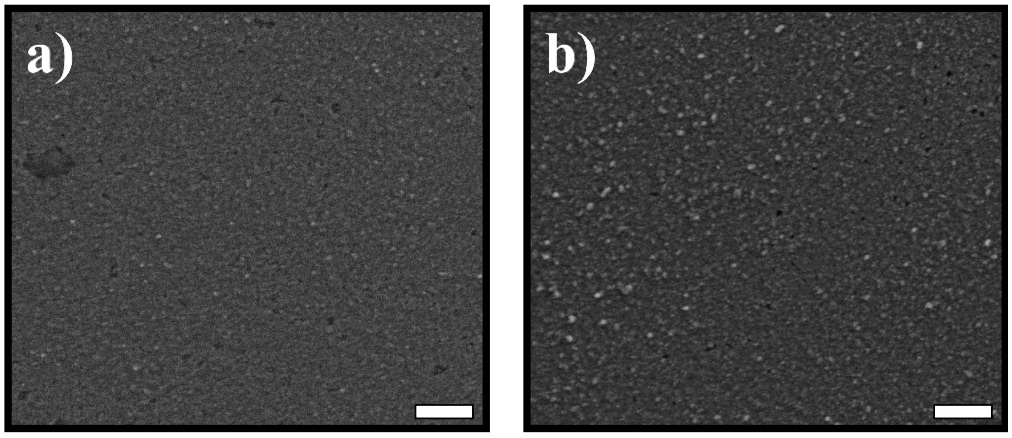

Figure 4.3 Scanning electron micrographs of a) as-deposited Cu film on a Si substrate b) Cu film annealed in Ar (g) at T = 200 °C for t = 120 s. Scale bar = 2 μm.

Electrodeposition of the top metal layer must not compromise the integrity of the underlying Cu_2O film. Specifically, either chemical etching of Cu_2O or partial reduction of Cu sites that perturbs film stoichiometry during top metal electrodeposition would compromise the optical quality of the MDM structures. As an alternative, Au films were again electrodeposited using the same stock solution that was prepared for the bottom Au electrodeposition, however a

radically different methodology than that used for the underlying Au film was necessary. Cu_2O is more chemically stable in alkaline solutions and will not reduce to Cu^0 so long as the potential is not made more negative than approximately -0.5 V vs. *E*(Ag/AgCl) (for *p*H ~ 11).[151] For these reasons, a portion of the Au stock solution prepared above was separated and its pH was adjusted to ~ 10-11 by addition of NaOH. A mercury sulfate (sat. K_2SO_4) reference electrode was employed, but the potentials are reported with respect to *E*(Ag/AgCl) for consistency. In this alkaline solution at T = 50 °C, Au electrodeposition was possible over a wide potential range (-2.06 < E < -0.52 V vs. *E*(Ag/AgCl)). Still, electrodepositions performed at E < -1.05 V vs. *E*(Ag/AgCl) on the Au/Cu_2O MD stack resulted in peeling off due to H_2 bubbles from concurrent proton reduction process. Accordingly, the top Au layer with a thickness of approximately 15 nm was specifically electrodeposited at E = -0.52 V vs. *E*(Ag/AgCl) and T = 50 °C with constant solution convection for t = 30 minutes. These factors ensured the underlying Cu_2O films were not compromised. AFM measurement of the final MDM structure is provided in Figure 4.4c. The surface morphology of each layer was investigated by tapping mode atomic force microscopy (TESPA-V2 tip and Dimension Icon AFM, Bruker Corporation). At a thickness of 15 nm, the top Au film did not significantly increase the overall roughness of the tri-layer stack (R_{RMS} = 5.3 nm, R_a = 3.5 nm). Although some larger Au aggregates (100 nm wide, 30 nm thick) suggestive of sporadic 3D film growth were observed, the overall macroscopic uniformity and regularity of these films yielded reflectance spectra very similar to responses predicted for the ideal flat slab film stacks.

The cross-section SEM image of a tri-layer Au/Cu2O/Au stack is shown in Figure 4.4d. Cross-sectional SEM was performed with a SU8000 FE-SEM (Hitachi High-Technologies Corporation) with a Schottky field emitter operated at 5 keV beam voltage. For this particular MDM stack, the thickness of the bottom Au, Cu_2O and top Au layers were designed to be 40 nm,

45 nm and 15 nm respectively, to obtain a magenta color. The variation between the average measured thickness of each layer in Figure 4.4d and the designed thickness values of the corresponding layers for the magenta color is minimal and this verifies a good control over film thickness during our electrodeposition process. However, the small degree of thickness variation between measured and designed thicknesses of each layer and the surface roughness of the electrodeposited films can lead to slight discrepancy between the measured and the ideal simulated spectra, as can be seen in Figure 4.5c.

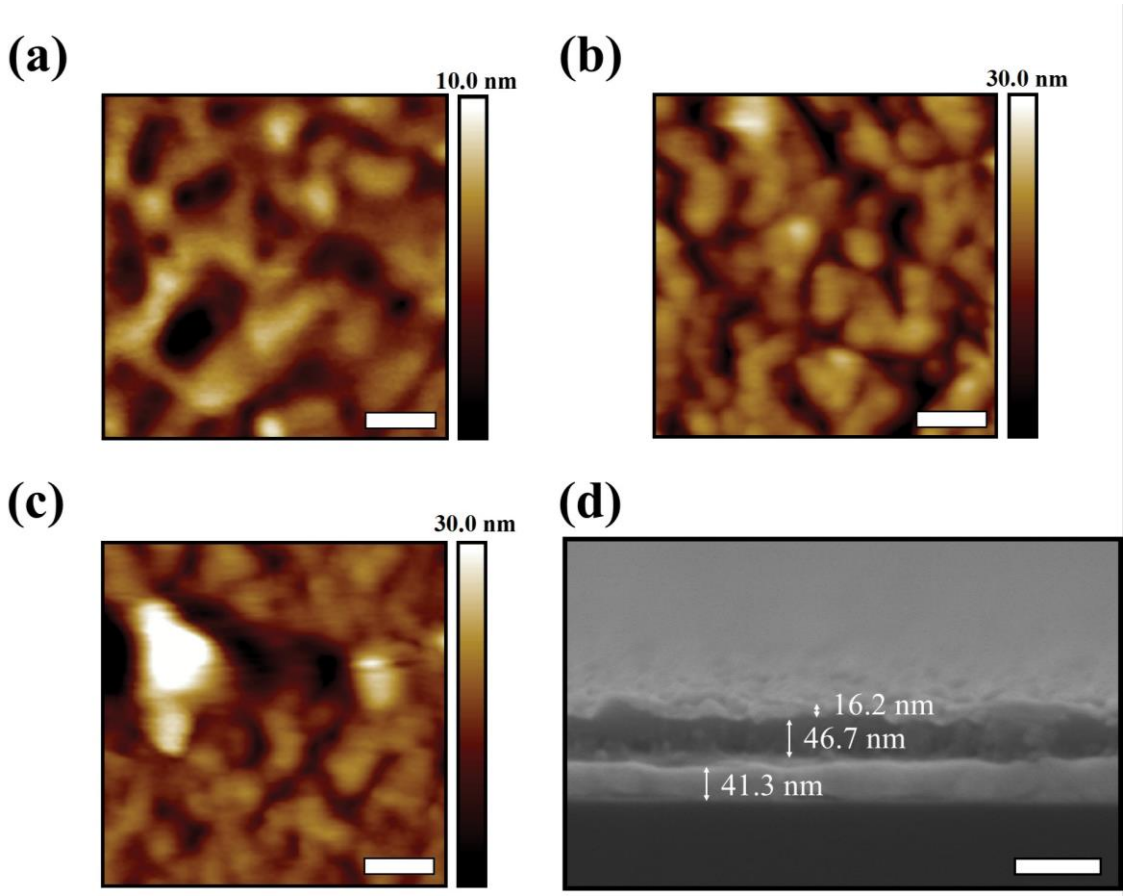

Figure 4.4 AFM measurements of a) bottom Au, b) Cu_2O/Au, and c) final Au/Cu_2O/Au structure on a n^+-Si(111) substrate. d) A representative cross-sectional scanning electron micrograph of the magenta colored devices, verifying the thickness of each electrodeposited layer. Scale bar = 100 nm.

4.4 Design Principle and Optical Characterization of Electrodeposited Structural Colors

Figure 4.5a illustrates the design of electrodeposition process for structural color films comprised of Au/Cu_2O/Au tri-layer MDM stacks on a crystalline n^+-silicon (Si) substrate. As will be discussed later, the method demonstrated in this work is not limited to n^+- Si substrates and can be extended to a variety of conductive surfaces regardless of their smoothness and shape. A three-electrode electrochemical cell design was employed for the electrodeposition (Figure 4.5b). Here the conductive n^+-Si substrates were used directly as the working electrode, while a platinum mesh counter electrode and suitable reference electrodes were used as part of the three-electrode electrochemical cell.

The thicknesses of the bottom and top Au layers were fixed at 40 and 15 nm, respectively. The thickness of the middle Cu_2O layer was varied intentionally to obtain the desired colors by exciting absorption resonances at different wavelength positions. For example, pure cyan, magenta, and yellow (CMY) film colors were realized with electrodeposited Cu_2O thicknesses of 70, 45, and 20 nm, respectively. The measured reflection spectra in Figure 4.5c (dashed curves) of the CMY colored devices agreed very well with predictions from optical simulations of the respective MDM structures (solid curves). The measured reflection spectra at normal incidence was obtained using a thin-film measurement instrument (F20, Filmetrics) integrated with a spectrometer and a white light source, while the simulated reflection spectra was calculated based on the transfer matrix method.[152] These simulations used measured refractive indices of the electrodeposited Au and Cu_2O thin-films from a spectroscopic ellipsometer (M-2000, J. A. Woollam Co.) as inputs. The insets in Figure 4.5c illustrate the colors of the fabricated devices as viewed from 0º with respect to the surface normal.

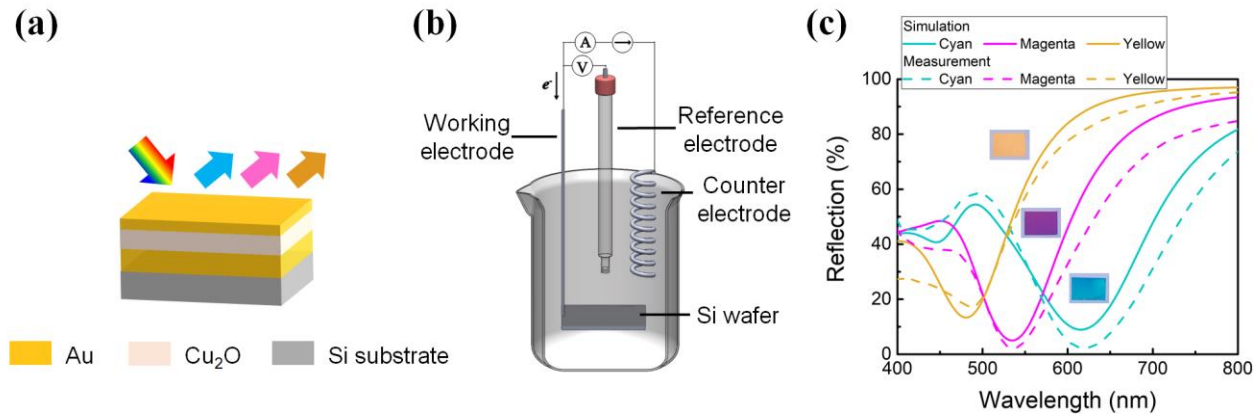

Figure 4.5 a) Design schematic of the solution processed structural colors comprised of tri-layer MDM stacks on a Si substrate. b) A schematic representation of the three-electrode electrochemical cell used for the electrodeposition of MDM structures. c) Measured and calculated reflection spectra of CMY colored devices. Insets are photographs of fabricated CMY samples. The size of each sample is 1.5 cm × 1.0 cm.

Figure 4.6a shows the refractive indices *n* and *k* (the real and imaginary parts of the refractive index, respectively) of the electrodeposited Au and Cu_2O films. Both data sets are generally in agreement with data recorded for Au and Cu_2O films prepared by vacuum-based deposition methods. The refractive index of the reference Au was characterized using Au films grown in our own lab by e-beam evaporation and the reference data for reactively-sputtered Cu_2O was extracted from Ref. [153]. Accordingly, these measurements illustrate the high-quality optical properties of these films despite being prepared entirely from aqueous solution. Even the measurably smaller *n* for electrodeposited Cu_2O as compared to that for Cu_2O bulk standards resulted in the need for only slightly thicker Cu_2O layers to generate a reflection dip at a given wavelength and to realize functional cavity layers for a given color. Figure 4.6b provides the net phase shift calculated using the transfer matrix method[152] and the measured refractive indices, which includes two reflection phases at both the top and bottom interfaces and the accumulated

propagation phase within the Cu_2O layer for the three CMY MDM films. These data clearly indicate the absorption resonances (λ=458 nm for yellow, λ=531 nm for magenta, and λ=618 nm for cyan, where the net phase shift is equal to a multiple of 2π) that selectively absorb light in the visible range for the reflective color generation, and are in agreement with the reflection dips seen in Figure 4.5c.

Figures 4.7a-c present the measured angle-resolved reflection spectra for electrodeposited Au/Cu_2O/Au MDM stacks under unpolarized light, which are in agreement with the model predictions for the angle-resolved reflectance of ideal Au/Cu_2O/Au MDM stacks shown in Figures 4.7d-f. Angle-resolved reflection spectra of as-prepared MDM stacks was performed with a spectroscopic ellipsometer (M-2000, J. A. Woollam Co.). The smallest incident angle measurable with this instrument was 45°. Thus, the measured spectra in Figure 4.7a-c have an angular range of 45° to 60°. However, reflectance spectra simulations for 0° to 60° viewing angles are reported to illustrate the wide range of angle insensitivity for our structural colors. The reflection valleys are almost invariant with respect to the incident angle up to ± 60°, due to the high refractive index of the Cu_2O cavity material which elicits a very small refracted angle into the structure.[115, 118, 154] Figure 4.7g presents a set of electrodeposited CMY structural color films viewed at various angles under ambient white light. In these images, the color purity of the films is unchanged at the different viewing angles, which addresses one of the key challenges facing many structural color designs.[16, 155-157]

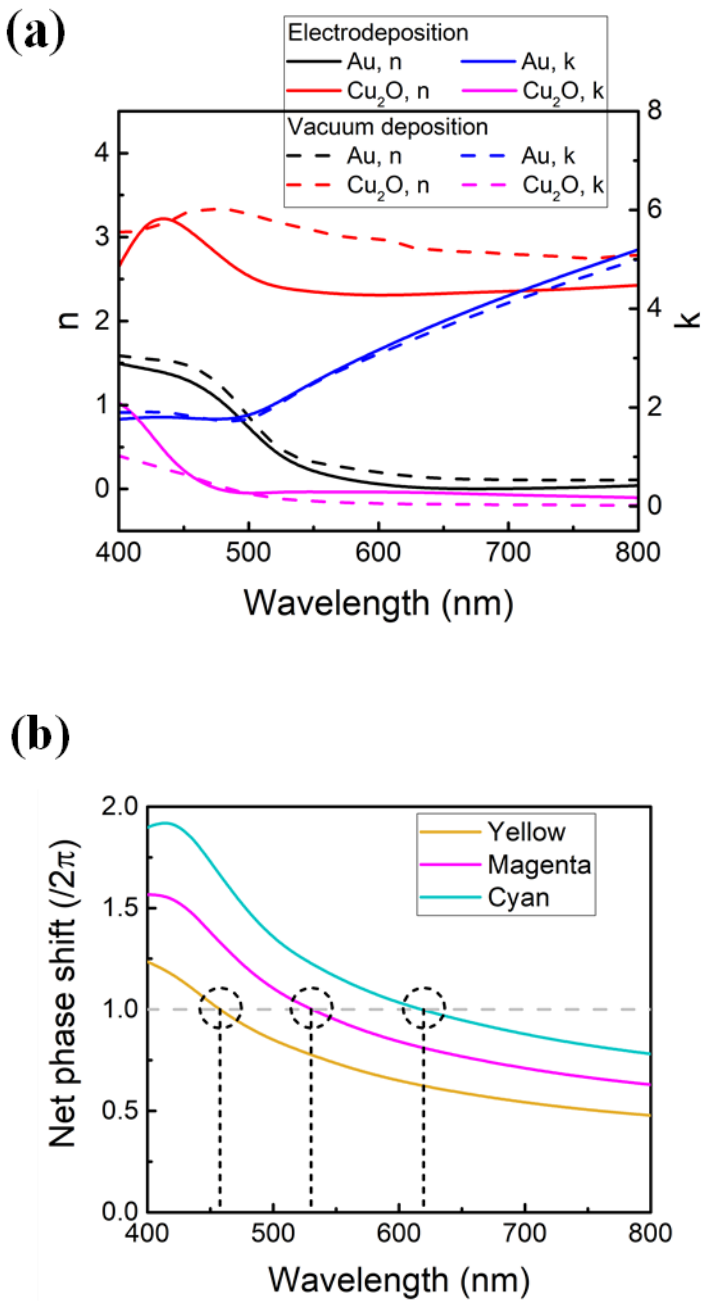

Figure 4.6 a) Refractive indices of Au and Cu_2O deposited by different methods. b) Net phase shift analysis of CMY colored MDM films. Absorption resonances that generate color defined by the reflection valleys occur when the net phase shift is equal to 2π.

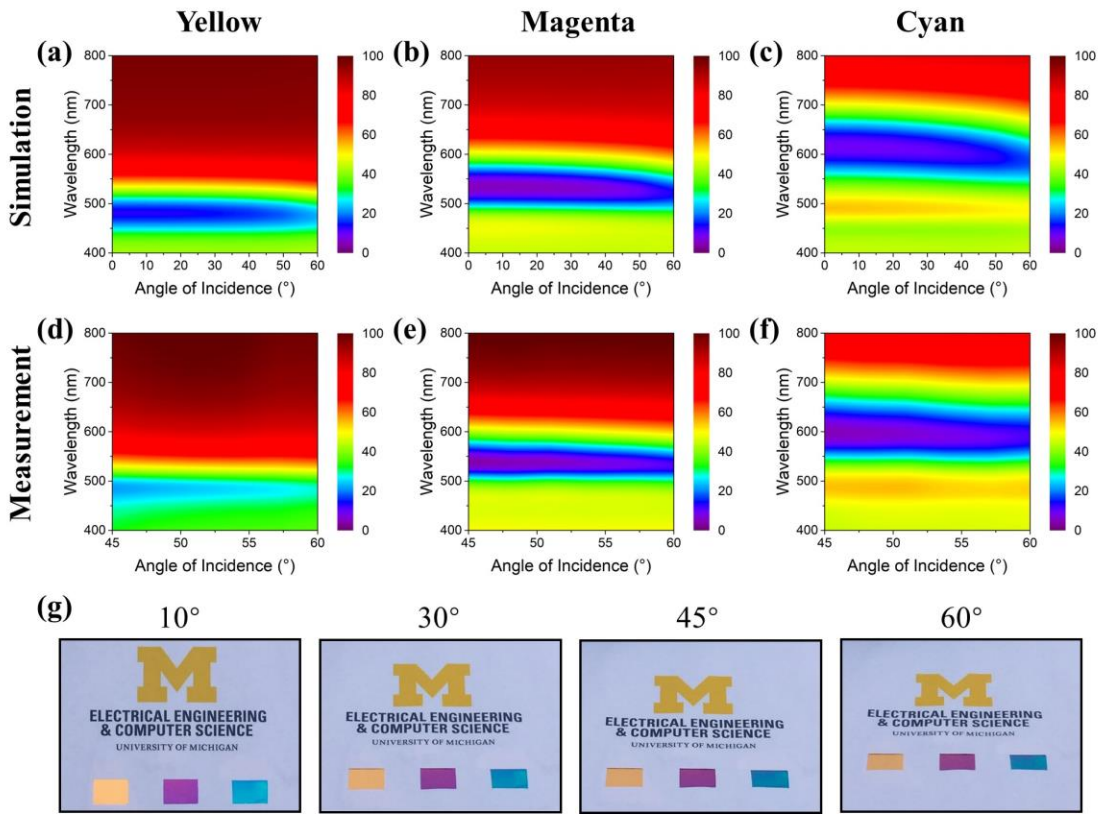

Figure 4.7 a-c) Simulated angle-resolved reflection spectra of CMY colored devices under unpolarized light illumination. d-f) Corresponding measured angle-resolved reflection of fabricated devices. g) Photographs of fabricated CMY samples taken at various observation angles demonstrating the angle-invariant performance of these devices. Each sample measured 1.5 cm × 1.0 cm.

4.5 Structural Colors on Curved Surfaces

A final test of the unique merits of electrodeposition as methodology for MDM color films was carried out on an irregularly shaped substrate. When performed carefully, electrodeposition can yield films that follow closely the contours of any electrode shape. To demonstrate the control afforded by the cumulative process developed here, Au/Cu_2O/Au MDM stacks were deposited on a working electrode consisting of stainless-steel spoons. Figure 4.8 shows the resultant glossy and

uniform color appearance of CMY colors on the curved and rough surfaces of these spoons. In these images, the curved profile of the spoon in effect illustrates reflectance over a wide range of viewing angles. The homogeneity and consistency of the colors, in addition to the lustrous appearance, directly validate the electrodeposited MDM approach. It must be noted that CMY colors are also obtained by directly electrodepositing Cu_2O followed by a thin Au layer on the stainless-steel spoon. In this case, the spoon surface takes the role of the bottom metal reflector in the MDM F-P resonator. In addition, a further advantage of these electrodeposited MDM films on the stainless-steel spoons was noted in an adhesion test. A standard peel test using adhesive tape[158] was applied on the as-prepared MDM coatings. These MDM films remained strongly adhered to stainless steel without obvious mechanical damage.

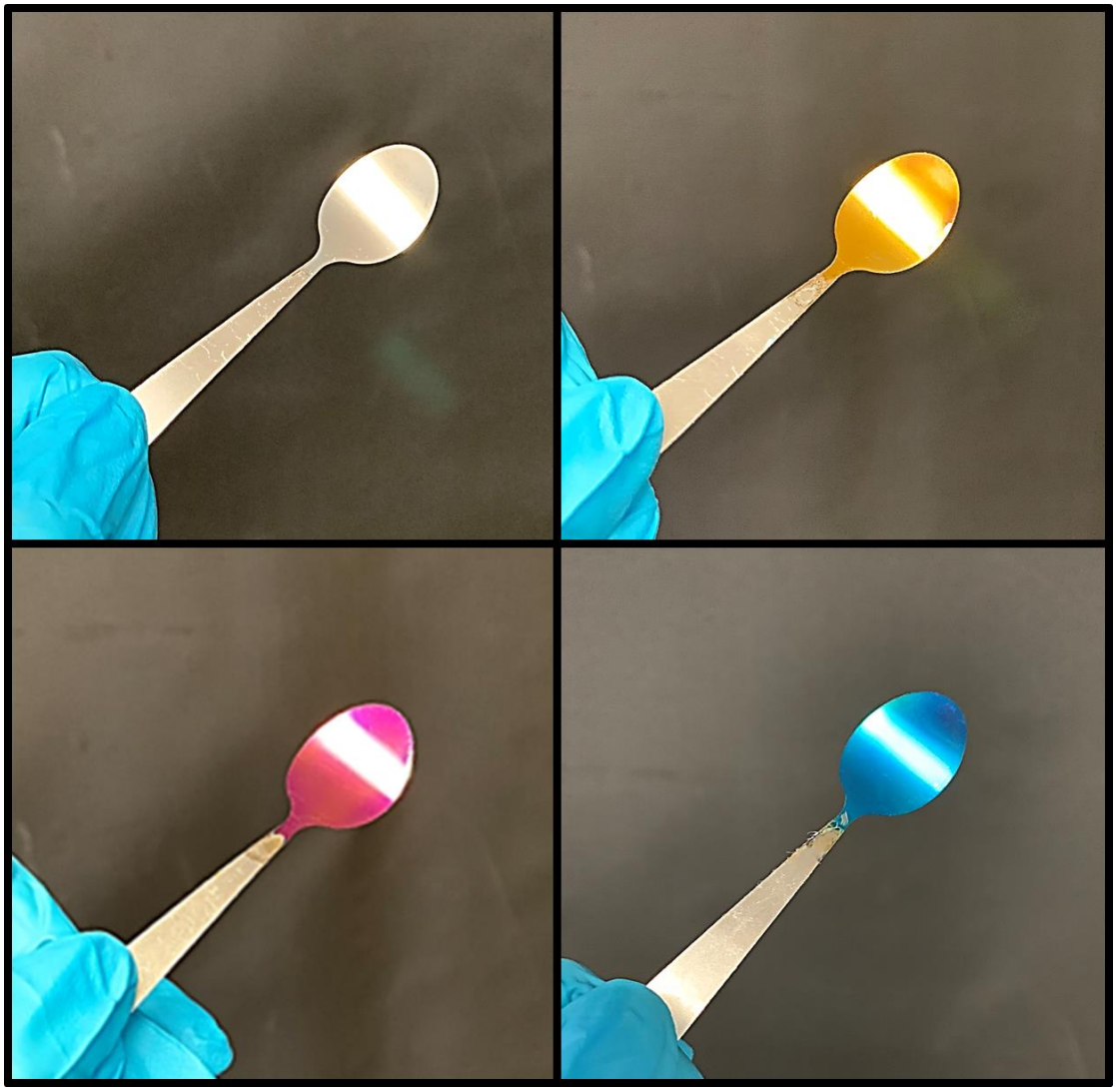

Figure 4.8 Photographs of stainless-steel spoons (top-left) without and with electrodeposited MDM structural colors on the curved and rough surfaces. The coated areas were approximately 6 cm^2.

4.6 Flexible Structural Color Films

Electrodeposition of MDM films can further be extended to achieve flexible structural colors for aesthetic applications. In this section, we demonstrate electrodeposition of inverted MDM structures on a flexible and transparent polyethylene terephthalate (PET) films. Figure 4.9 illustrates the design schematic for the solution processed flexible structural colors. In this structure, unlike the structural color devices presented in the previous sections, the color is observed from the transparent substrate (i.e. PET) side. Figure 4.9 illustrates the design schematic of the electrodeposited structural color films comprised of multilayer Au/Cu_2O/Cu/Ag MDM stacks on a flexible PET film. Here, a thin Au film sputtered onto the PET film serves two purposes: (1) it acts as the top ultra-thin metal layer of the asymmetric metal-dielectric-metal Fabry-Perot cavity, and (2) it serves as a conducting film on PET, thereby enabling the PET film to serve as the working electrode for subsequent electrodeposition processes. It must be noted that, Au can be replaced with other metals that are compatible with subsequent Cu_2O electrodeposition process.

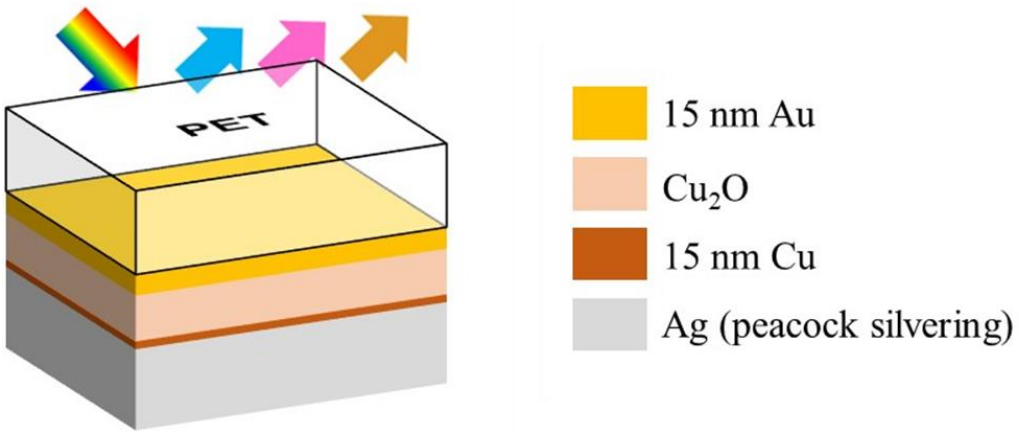

Figure 4.9 Design schematic of the solution processed flexible structural colors comprised of inverted MDM stacks on a transparent PET film.

PET films were degreased by sequentially sonicating for 5 minutes each in isopropyl alcohol and water, and then dried under a nitrogen (N_2) gas stream. For this demonstration, Ti(3nm)/Au(15nm) was deposited on the PET films using a DC magnetron sputtering (LAB 18, Kurt J. Lesker Company). All electrochemical depositions were performed in a three-electrode cell in lab ambient and $T \leq 50$ °C, similar to the process described in section 4.3. Using the conducting PET film as the working electrode, Cu_2O thin-films were electrodeposited from alkaline Cu(II)-citrate solutions. The Cu_2O electrodeposition process is already described in detail in section 4.3.3. Kapton tape was used to define the total active area of these working electrodes in contact with the solution. The cathodic current density during the deposition was set to 0.05 to 0.075 mA/cm^{2,} and Cu_2O films of different thickness was obtained by performing growths for different durations. Electrodepositions performed at T = 50 °C and under convection resulted in uniform Cu_2O electrodeposition (~ 0.05 – 0.1 nm/s).

Ag was deposited as the thick metal reflector by the peacock silvering process.[159] This process involves the use of four solutions: Silver solution (contains the silver diammine complex precursor), Activator solution (contains NaOH and ammonium hydroxide (NH_4OH) to control the pH of the plating solution), Reducer Solution (contains an invert sugar compound to reduce the precursor in solution) and a Sensitizer Solution (contains a stannous chloride ($SnCl_2$) reducing agent to improve uniformity of the Ag plating). Prior to the Ag deposition step, the sample needs to be immersed in the sensitizer solution to adsorb the reducing agent ($SnCl_2$) on the surface of the sample. However, the sensitizer solution is composed of HCl that etches the Cu_2O layer. For this reason, a protective Cu film was electrodeposited between the Cu_2O and the Ag layer using equation *4.2*. 15 nm Cu was electrodeposited on Cu_2O using a cathodic current density of j = 1 mA/cm^2 for t = 20 s, while all other parameters were similar to those used for the Cu_2O

electrodepositions. Next, the silvering process was initiated by soaking the sample in the sensitizer solution for 1 minute and then rinsed with DI water. This was immediately followed by dipping the sample in a bath containing equal parts of the Silver, Activator and Reducer solutions for 1 minute. Finally, the samples were rinsed with DI water and dried under a N_2 gas stream.

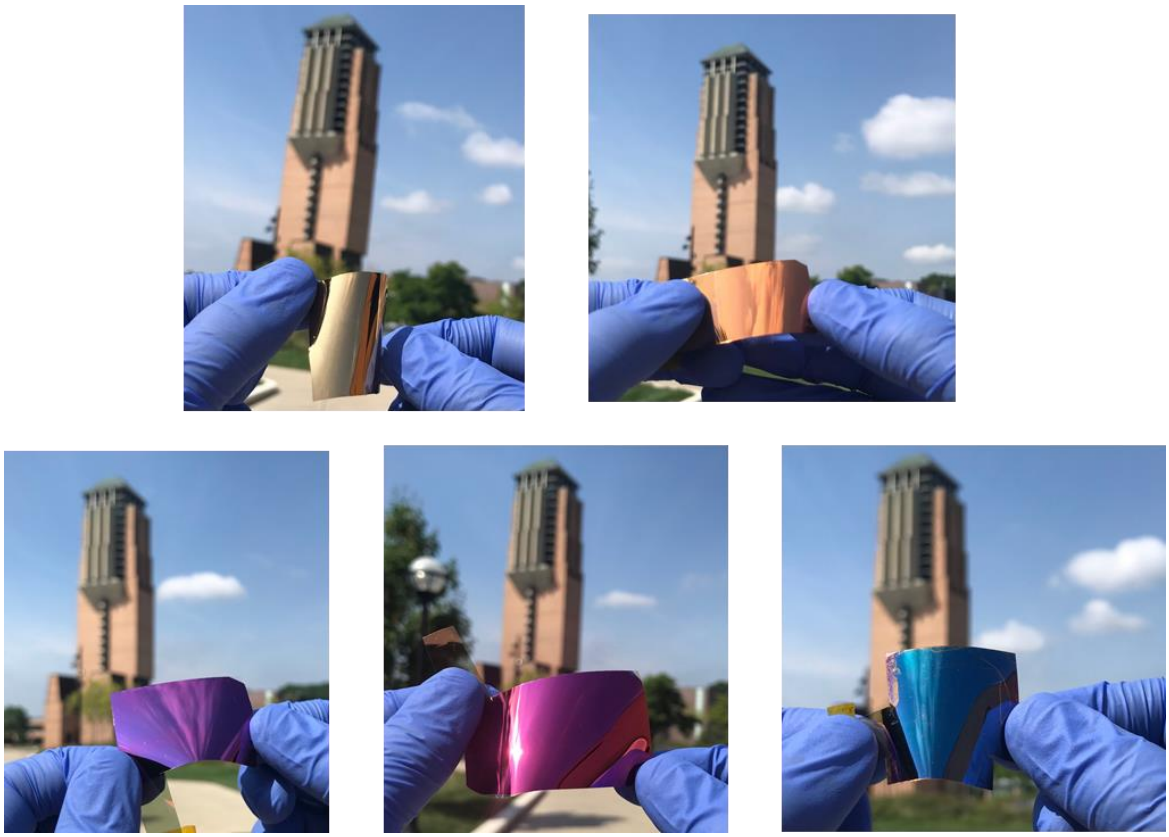

Figure 4.10 Photographs of MDM layers deposited on flexible PET. The thickness of the dielectric cavity layer is varied to achieve a wide range of colors.

For this demonstration, the thickness of the Au, Cu and Ag layers were fixed at 15 nm, 15 nm and ~ 200 nm, respectively, while the thickness of the dielectric cavity layer (Cu_2O) was intentionally varied to obtain the desired colors. Figure 4.10 presents the photographs of the

fabricated structural colors as seen through the transparent PET film. The color is stable after several bending tests, but more complete and informative tests are ongoing. Also, the colors of the electrodeposited MDM films are clearly insensitive to the viewing angles, as the appearance of samples are uniform even after bending. It must be noted that the Ag peacock silvering step can be replaced with a Cu electroplating process, provided the electroplating condition doesn't reduce or etch away the underlying layer. Efforts are ongoing in this regard with positive results.

The results presented here demonstrate a novel, low-cost approach to color any given transparent plastic film. The structural colors presented here have the added advantage of possessing a protection on both sides, i.e., PET film on the top side and a thick metal film on the back side.

A final note should be made regarding the specific components employed here. In principle, electrodeposition of MDM layers can be performed with a wide variety of different metal and dielectric layers. The Cu_2O dielectric layer represents a significant improvement in terms of safety over prior demonstrations of electrodeposited structural colors. Specifically, electrodeposited chromium oxide films have been used as interference color coatings on metal surfaces[138, 140, 160, 161] because film thicknesses up to 500 nm can be readily obtained.[162, 163] However, the toxicity of chromium electrolytes is substantial and such solutions are considered extremely potent pollutants.[164] In contrast, the copper citrate solution used here is comparatively benign, closely mirroring the composition of a common colorimetric solution used to test for sugars in water.[165] Still, it is conceivable that other dielectrics that can be readily electrodeposited including amorphous silicon,[166] titanium oxide,[167] and zinc oxide[168] could be used to form cavity layers in MDM structures. Doing so may facilitate the electrodeposition of other coinage metals such as Ag, Cu, and Al that would lead to similar reflectance and brightness properties.

4.7 Conclusion

In summary, a novel and facile method for MDM structural color films that can be performed entirely under ambient conditions with a simple bench-top set up has been demonstrated. The designs of these structural colors are based on asymmetric MDM F-P resonators. The thickness of the sandwiched Cu_2O dielectric layer can be readily tuned by electrodeposition parameters so as to generate any arbitrary CMY color. The high refractive index of electrodeposited Cu_2O results in stable, angle-insensitive color up to ± 60°. This electrodeposition tactic has been applied both to flat, curved, and flexible substrates and is readily scalable since expensive ancillary equipment is not required. These aspects cumulatively open up new avenues for development and implementation MDM structural color films.

Chapter 5

Dynamically Tunable Multi-State Structural Color Filters using Electrochromic Thin-Films[†]

5.1 Introduction

As highlighted in the previous chapter, color is one of the basic elements of life; without it the world around us would be dull and unappealing. Each day tons of organic dyes and colored elements have been consumed. But most pigments cannot withstand high temperature or severe chemical conditions; some have environmental concerns; the color of dyes can fade over time, accelerated by strong light. In recent years, structural colors based on optical interference effects of layered structures and resonance of nanostructures have received tremendous amount of interest due to their various advantages over traditional colorant-based pigmentations. The specific optical response of a structural color device is predetermined by the structure and design of the device. Tunability in the optical response of these devices is highly desired and has recently gathered significant interest.[169] Tunable colors are highly desired for a variety of applications including,

[†] All experiments, data analysis, and figure construction for this chapter were performed by Saurabh Acharya. Zhengmei Yang performed the E-field distribution simulation. L. Jay Guo was the principal investigator for the project.

passive displays, e-papers, decorative coatings, chemical and biological sensors, and encryption. Many schemes based on phase change or morphology change have been proposed. Metal hydrides are a class of materials examined for tunable applications.[170, 171] These materials undergo crystalline phase transitions, altering their electronic structures which in turn induces dynamic optical properties. It is an excellent approach to tackle the holy grain of encryption, which is to hide and reveal sensitive information on demand. The color tunability in reversible Ag-electrodeposition based multicolor devices are driven by the reversible deposition and dissolution process of a metal on a transparent substrate, and the optical state is dictated by the dynamic change in morphology of the deposited Ag nanoparticles.[172-174] Tunable properties of structural colors by dynamic alteration of the structure geometry have also been proposed by emulating the phenomenon observed in certain aquatic vertebrates.[175] But all these works suffer from one or many of the following issues: slow switching, poor cycling lifetime and reliability, limited tunability, angle-sensitive appearance, low brightness, etc. On the other hand, dynamic color-tuning where the structural color device responds to the nature of incident polarization has also been proposed in polarization-sensitive spectral filters,[176, 177] but this requires additional components to control and tune the incident light which is not practical for some of the applications listed above.

Approaches that produce a wide range of tunable colors at low-power and fast speed is highly desired. Phase change materials integrated into an optical cavity has been recently explored for this purpose.[178] However, severe localized heat required for stable switching operation and complicated structures (consisting of a stack of seven or more layers) required to realize tunability between four colored states limits the congruence of this approach for a variety of applications. Similarly, embedding an electro-optical (EO) active material in the structural color design allows

one to electrically tune the optical structure for applications where the large voltage bias required to modulate the EO material is not an issue.[179-181] In both these cases, a large external perturbation is required to induce a change in refractive index of a thin-film, which in turn produces tunability in the optical response of the color filter.

In comparison, electrochromic materials are a very well-studied class of materials who's the refractive index can be constantly changed by application of a small electrochemical perturbation.[182-190] Researchers have been able to complete the color palette using purely electrochromic materials.[191-193] However, the electrochromic community's focus has been on generating films that can be tuned from a transparent or neutral state to a colored state.[191, 193-197] Multi-color tunability using a single electrochromic layer has not been demonstrated and different electrochromic materials are required to complete the color palette. Electrochromic films also suffer from low brightness; however they do offer the advantages of fast to moderate switching speed, long-term switching stability, and low-power requirement.[193, 197]

In this chapter, data describing a simple approach to generate tunable color filters by incorporating an electrochromic layer into a subwavelength layered optical cavity is presented. As a demonstration, a four-layer asymmetric dielectric-absorber-dielectric-metal (DADM) Fabry-Pérot (F-P) cavity is shown, producing multi-state bright reflective colors from a single device. The absorption wavelength of this F-P cavity can be controlled by tailoring the thickness of the nanocavity or the top anti-reflection coating. Here, the refractive index of the electrochromic layer was continuously varied by application of a small range of electrochemical bias (-1 V to 0.5 V), and the effect is analogous to tuning the thickness of the electrochromic layer acting as the anti-reflection coating. Tunable structural colors with low energy consumption, short response time, and high repeatability are demonstrated for multiple devices.

5.2 Tunable Optical Constants of Electrochromic Films

5.2.1 Sample preparation and Experimental Setup

Figure *5.1a* depicts a schematic view of the proposed structural color filter based on a DADM multi-layered configuration to achieve dynamically tunable and polarization-independent highly reflective colors. This is a simple asymmetric Fabry-Perot (F-P) cavity structure, consisting of a tungsten (VI) oxide (WO_3) anti-reflection (AR) overlayer, an ultra-thin absorptive layer of tungsten (W), a titanium oxide (TiO_2) spacer layer, and a thick aluminum (Al) mirror on a silica substrate. Strong interference effects excited in the top and middle dielectric layers result in high reflection of only a narrow band of wavelengths, while the absorber layer induces strong optical absorption at other wavelengths of the incident light, producing highly saturated reflective colors. By exploiting the electrochromic property of the top WO_3 film, the optical response of the designed structure can easily and quickly be modulated by changing the applied potential, achieving dynamically tunable reflective colors. Thus, the WO_3 dielectric film has the dual purpose of serving as the antireflection coating as well as an electrochromic film which imparts the tunable optical properties to the F-P cavity-based device. WO_3 was selected in this study owing to its high coloration efficiency (or optical contrast and density) and stable switching performance, but any other organic and inorganic electrochromic material can be applied to the tunable structural color scheme presented in this work. The bottom metal comprising of 5 nm/100 nm Cr/ Al was used as an optical mirror providing high reflection across the visible spectrum and was deposited on a silica substrate using DC sputtering (LAB 18, Kurt J. Lesker Company) with argon (Ar) gas pressure of 4.5 mTorr, power of 400 watts, and a deposition rate of 0.3 nm/sec. This was followed by TiO_2 thin-film deposition using an e-beam evaporator (EvoVac, Angstrom Engineering) with a chamber pressure of $2x10^{-6}$ torr and deposition rate of 0.3 nm/sec. An absorber layer of ultra-thin

W was deposited using DC sputtering with Ar gas pressure of 5 mTorr, power of 400 watts, and a deposition rate of 0.22 nm/sec. Lastly, the top electrochromic WO_3 AR layer was prepared by DC reactive sputtering using a metallic W target. During sputtering, the power was set to 300 watts, oxygen (O_2) gas flow was maintained at a 40% of Ar gas flow rate, while the Ar gas pressure was set to 6 mTorr. Detailed analysis of the function of each of these layers will be discussed in the following paragraphs. Once the asymmetric DADM structure is fabricated, tunable structural colors were realized by using a standard three-electrode electrochemical cell and immersing the sample in an acetonitrile solution containing 100 mM lithium perchlorate ($LiClO_4$) at ambient conditions. The working electrode was connected to the W absorber layer, while a saturated calomel electrode (SCE) and platinum (Pt) mesh electrode were used as the reference and counter electrodes respectively. A computer controlled potentiostat (Solartron Analytical 1287A, AMETEK Scientific Instruments) was used throughout to apply the potential and measure current between the electrodes.

5.2.2 Spectroscopic Ellipsometry of Electrochromic WO_3 Films

Figure *5.1b* shows the continuous variation of the refractive index (including the real part *n* and the imaginary part *k*) of the electrochromic WO_3 film with an applied potential, representing varying degrees of electrochromism. A 50 nm thick WO_3 film was grown using the reactive sputtering process described above on a degenerately doped n^+-Si substrate. The electrochromic change was again performed in the three-electrode electrochemical setup mentioned above. Here the conductive n^+-Si substrate was used as the working electrode. The refractive index of the WO_3 film was characterized using a spectroscopic ellipsometer (M-2000, J. A. Woollam Co.). As the Li^+ ions are driven into the WO_3 film by application of a negative potential to the working electrode,

the oxidation state of the W^{6+} ion in the WO_3 lattice is reduced as per the following lithiation reaction:

$$WO_3 + xLi^+ + xe^- \rightarrow Li_xWO_3 \qquad (5.1)$$

altering their electronic structure and subsequently inducing a change in their optical properties. The magnitude of applied potential dictates the depth to which the Li^+ ions are driven into the WO_3 film and this varying degree of electrochromic change along the depth of the film gives rise to the continuous range of optical states for the WO_3 film. The refractive index for E = -1.2 V vs. *SCE* (blue plot) corresponds to the completely colored state (semi-transparent blue) of WO_3, while that for E = 0.5 V vs. *SCE* (orange plot) corresponds to the bleached state (transparent). The ultra-thin WO_3 film utilized in this study allows us to completely lithiate and delithiate the WO_3 film by applying only a small potential. The huge difference in the optical constants in Figure *5.1b* illustrates several clear advantages of using electrochromic films for tunable color purposes: (1) tunability between a large number (> 6) of colors owing to continuous optical states of the electrochromic film (2) very small potential (and power) required to tune between optical states (3) easily reconfigurable high-quality optical properties. Accordingly, these measurements illustrate the motivation to incorporate electrochromic films into the F-P cavity based DADM structure and the ability to generate multi-state color tuning from a single pixel or device is discussed below.

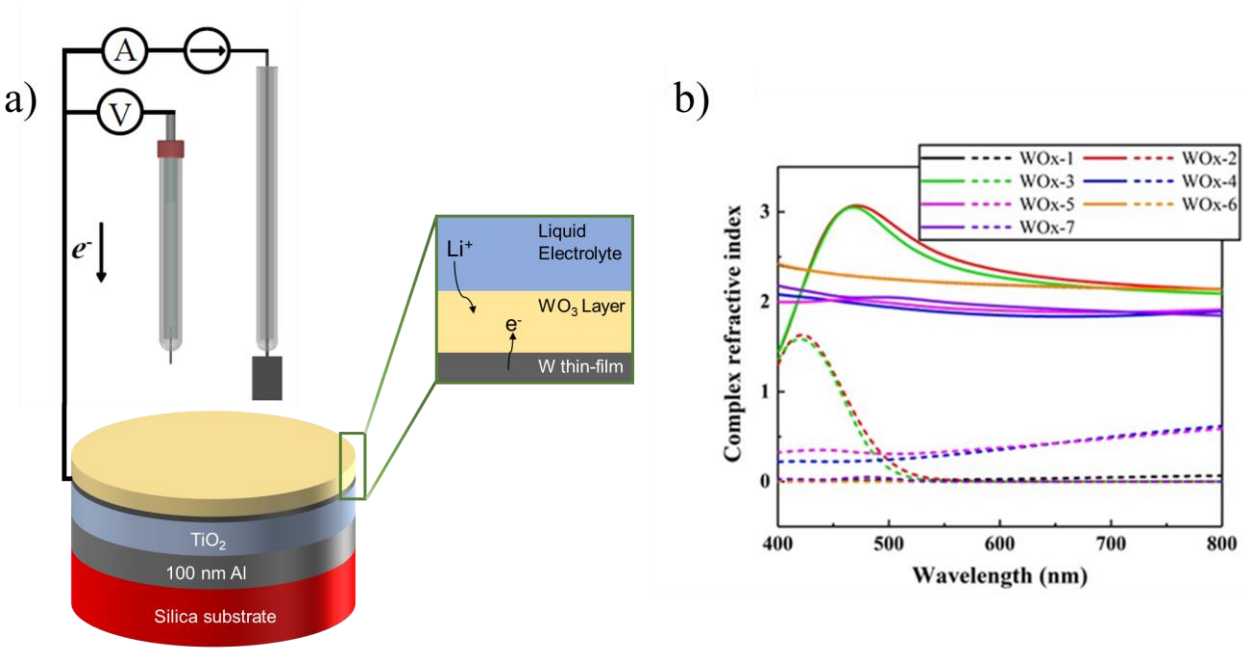

Figure 5.1 a) Design schematic of the proposed tunable structural color device comprised of multi-layer DADM stacks. b) Refractive indices of the WO_3 film for varying degrees of electrochromic change.

5.3 Design Principle and Optical Characterization of Tunable Structural Colors

For a proof-of-concept demonstration of tunable color change, the thickness of the bottom Al reflector was 100 nm, whereas the TiO_2 spacer layer, W absorber layer, and WO_3 AR layer was set to 142 nm, 15 nm, and 48 nm, respectively. Transitions between different colored states of the device was realized by dynamically varying the refractive index of the WO_3 AR layer, while the thickness of the individual layers were unaltered. Although transitions between multiple (> 4) colored states are possible due to the large variation in the refraction index of electrochromic materials (Figure *5.1b*), we restrict this study to transitions between 3 colored states for simplicity

of discussion. The measured reflectance spectra of the DADM structure discussed above is presented in Figure *5.2a*. Reflectance spectra were measured at normal incidence using a thin-film measurement instrument (F20, Filmetrics) integrated with a spectrometer and a white light source. The magenta plot corresponds to the optical state of the structural color device after being exposed to E = -0.25 V vs. *SCE*. An electrochemical change on application of E = -0.9 V vs. *SCE* in the electrochemical cell results in a reversible transition in the reflectance to the brown plot, while further application of E = -1.2 V vs. *SCE* results in a reversible transition to the blue plot. Figure *5.2b* show the optical images of three reconfigurable colored states of the same DADM structure, demonstrating large-area uniform tunable color change. The corresponding color coordinates evaluated from the measured reflection spectra are shown on the CIE 1931 chromaticity diagram in Figure *5.2c*. It can be seen that the color coordinates for the magenta (0.51, 0.24), brown, and blue (0.22, 0.16) covers a wide area of the CIE chromaticity diagram. In principle, the proposed approach for achieving tunable structural color filters can be used to obtain a wide range of color tunability from a single device or pixel, while maintaining high brightness and color purity in the visible wavelength region.

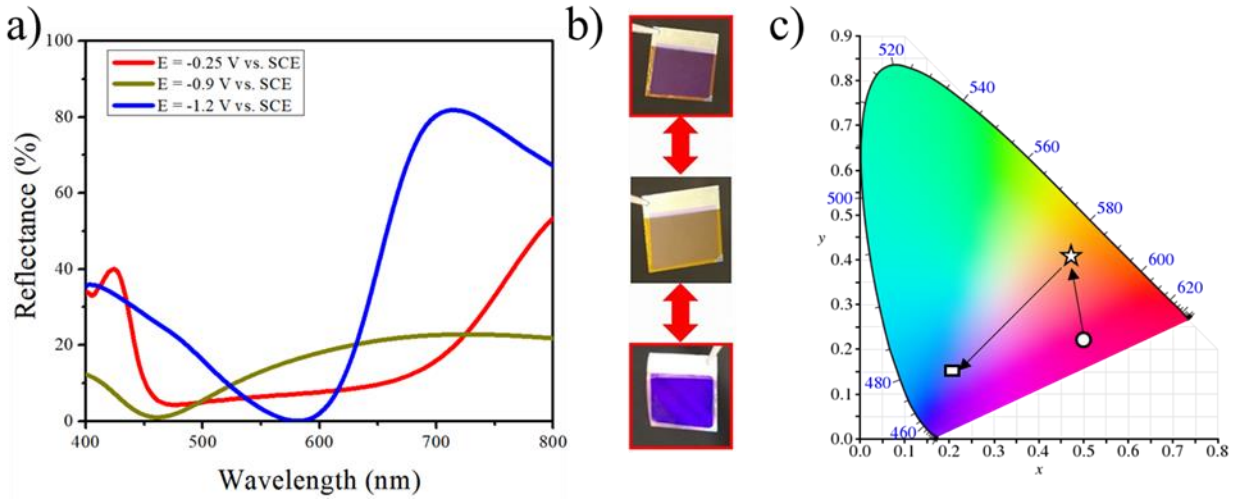

Figure 5.2 a) Measured reflection spectra of three different colored states of the DADM device. b) Photographs of corresponding reconfigurable colored states of the DADM device. The size of each sample is 1.5 cm × 2.0 cm. c) The calculated chromaticity coordinates corresponding to the reflection spectra shown in (a) in the CIE 1931 chromaticity diagram.

To explain the physical reason for color change in our structural color device, we take the example of the structure provided in Figure *5.1a* and consider the case of magenta (E = -0.25 V vs. *SCE*)) to blue (E = -1.2 V vs. *SCE*) color transition. For ease of understanding, the refractive index of the WO_3 thin-film is replotted in Figure *5.3b* for the two potential conditions that result in magenta and blue colors for the DADM thin-film structure. From Figure *5.2a*, for magenta color, the peak reflection wavelength is centered at λ_c= 670 nm, while the off-peak wavelength at λ_0= 415 nm, corresponding to the blue spectrum, is suppressed. In the simple DADM thin-film structure, the purpose of the 100 nm thick Al film is to act as an optical mirror to provide high reflection and prevent any light transmission. The thickness of the spacer TiO_2 layer was set to 142 nm), corresponding to the half-wave optical thickness of λ_c= 670 nm (high reflection for red wavelengths). The thickness of the top WO_3 dielectric layer acting as the AR layer is fixed at 48

nm, which corresponds to the quarter-wave optical thickness of λ_0 = 415 nm (for suppressing blue). Lastly, a 15 nm thick W film is used as the absorber layer to achieve high absorption at the off-peak wavelengths. For the case of magenta color corresponding to E = -0.25 V vs. *SCE*, the electric field distribution in Figure *5.3c* illustrates a strong optical resonance in the anti-reflection layer centered at λ = 425 nm and λ = 630 nm. It can be seen that this enhanced electric field leaks into the W absorber layer in the wavelength range of λ = 425 to 600 nm, resulting in high absorption in the W layer in this range and giving rise to the perceived color of the device. The electric field distribution inside the DADM structure exhibits a strong first order F-P cavity resonance mode resulting in high reflection in the red spectrum, but it also exhibits second order resonance modes resulting in a finite reflection in the blue spectrum. However, the reflection in the blue spectrum is relatively small, and so the device shows a magenta appearance. Another way to explain the color appearance is by looking at the net phase shift experienced by the incident light through the DADM structure. Figure *5.3e* provides the net phase shift calculated using the measured refractive indices for both the potential conditions, which includes reflection phases at each interface and the accumulated propagation phase within the top WO_3 AR layer. The net phase shift within the structure for (E = -0.25 V vs. *SCE*) is close to zero for the wavelength range of λ = 425 to 600 nm, thus resulting in high absorption in the W layer in this wavelength range.

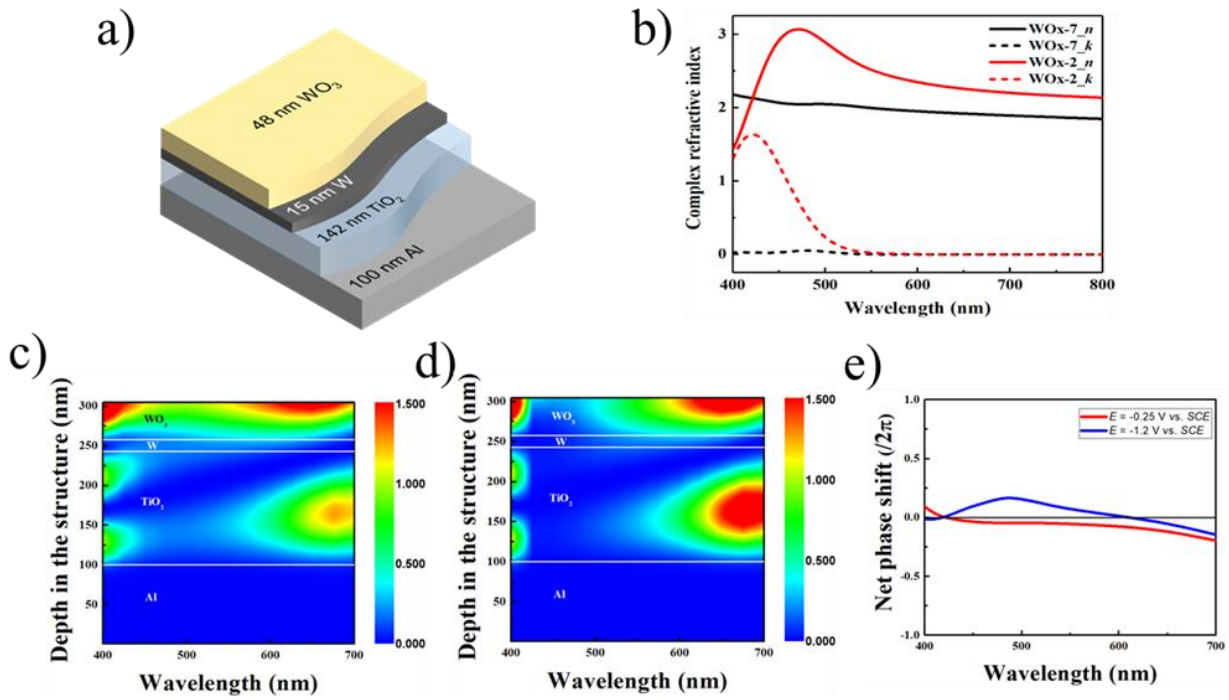

Figure 5.3 a) Design schematic of the tunable structural color device under study. b) Refractive indices of the WO_3 corresponding to E = -0.25 V vs. *SCE* and E = -1.2 V vs. *SCE*. c-d) The wavelength-dependent electric field distributions inside the structure shown in (a) for its magenta and blue colored optical states. e) Calculated total phase shift in the WO_3 AR layer as a function of wavelength.

Now when the n and k values of the WO_3 thin-film are altered on application of a potential E = -1.2 V vs. *SCE*, the anti-reflection resonance condition becomes unsatisfied for most of the short wavelengths, thereby increasing the device reflection at these wavelengths (Figure *5.2a*). As can be seen in the electric field distribution in Figure 5.3d, two anti-reflection resonance modes at λ = 425 nm and λ = 620 nm are excited within the WO_3 layer. However, the resonance mode at λ = 425 nm is relatively weak, and the resultant electric field leaking into the W absorber layer is very small. Thus, the device exhibits a single absorption peak at λ = 590 nm (Figure *5.2a*) corresponding to the anti-reflection resonance mode at λ = 620 nm. Therefore, after instituting the

color change, the reflection in the blue color spectrum was increased while the reflection in the red color spectrum was not altered significantly, and the device color was tuned from magenta to blue.

5.4 Stability and Cycling Performance of Tunable Structural Color

Long term switching stability of inorganic electrochromic materials has been demonstrated previously and is a very attractive feature for tunable photonic devices. The switching stability of the proposed tunable structural color devices was also examined in this study. Figure *5.4b* shows the charge/discharge amount as a function of time for the DADM structure when exposed to 100 switching cycles of periodic potential wave (Figure *5.4a*). The charge cycle was set to t = 20 s at E = -1.5 V vs. *SCE*, while the discharge cycle was set to t = 30s at E = 0.5 V vs. *SCE*. These measurements were performed using a three-electrode electrochemical setup as discussed above. This plot represents the Li^+ ions driving in (charge) and out (discharge) of the WO_3 layer, so the current cycling measured here translates to the color cycling performance of the structural color device. The fully discharged and charged states corresponds to the magenta and blue colored appearance of the device, respectively. There is a small variation in the peak current magnitude in the charging (reduction) and discharging (oxidation) periods during the 100 switching cycles presented in Figure *5.4b*, however the total charge passed (area under the curve) during each cycle is consistent among all cycles. Additionally, Figures *5.4c* and *5.4d*, provide the zoomed in version of the first and last few cycles of the 100 switching cycles, demonstrating no degradation in the cycling performance. These data clearly illustrate the excellent cycling performance of the tunable DADM device. From the reduction peaks in Figure *5.4c*, which show the charge amount required to tune the device from a magenta to blue appearance after switching the applied potential from

0.5 V to -1.5 V vs E(SCE), the value of Q = 2.23 mC/cm^2 can be obtained. Similarly, the amount of charge needed to return the appearance back to its initial magenta appearance can be calculated from the oxidation peak as Q = 2.06 mC/cm^2. The very small amount of charge required to actuate a color change in the proposed structure stems from the ultra-thin nature of the electrochromic thin-film used in the structure. Thus, the proposed tunable color devices exhibit the important property of being highly efficient in terms of power consumption and also show impressive coloration efficiency, which is defined as the extent of change in optical density caused by a finite charge amount during the redox reaction in an electrochromic material.

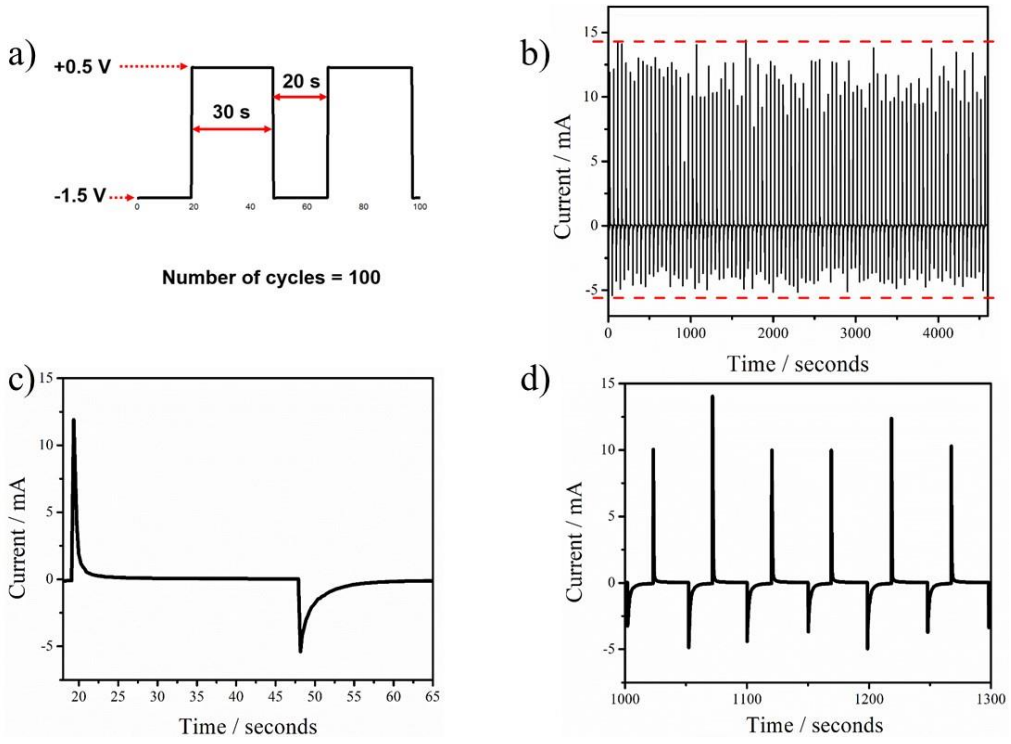

Figure 5.4 a) Potential waveform applied to the DADM structure for the cycling test. b) Measured current as a function of time on application of the potential waveform depicting 100 charge and discharge cycles. c) Zoomed-in version of the charge and discharge current corresponding to the first cycle. d) Charge and discharge current corresponding to the 20th to 25th cycles.

Even though we selected a charging and discharging time of t = 20 s and t = 30 s, respectively, this is in no means representative of the minimum time required to induce color change. A conservative charging/discharging time was selected for the cycling test presented above, but it can be seen from the reduction and oxidation plots that majority of the charge is passed within the initial few seconds of each cycle. Figure *5.5* shows the cycling performance is not altered even as we reduce the charge/discharge time by up to an order of magnitude lower. The exact switching time can be calculated from the plots in Figure *5.4c* and *5.4d* (and Figure *5.5*). The proposed device switches from the magenta to the blue state in 3 seconds, and it takes 1 second to return to its original magenta-red colored appearance. Again, the fast switching time between the multiple optical states of the tunable DADM structure is a direct consequence of the ultra-thin thickness of the WO_3 layer utilized in this structure. We expect the switching time for tunable structural color devices incorporating an electrochromic layer to further reduce to the millisecond range by optimizing the conductivity of the electrolyte utilized.[198] As a final demonstration of the stability of our proposed tunable structural color device, appearance of the perceived color before and after the cycling test was also examined. As shown in Figure *5.6,* the spectra as well as the photograph of the DADM structure from Figure *5.2b* in its blue color state shows no measurable difference even after 1000 switching cycles.

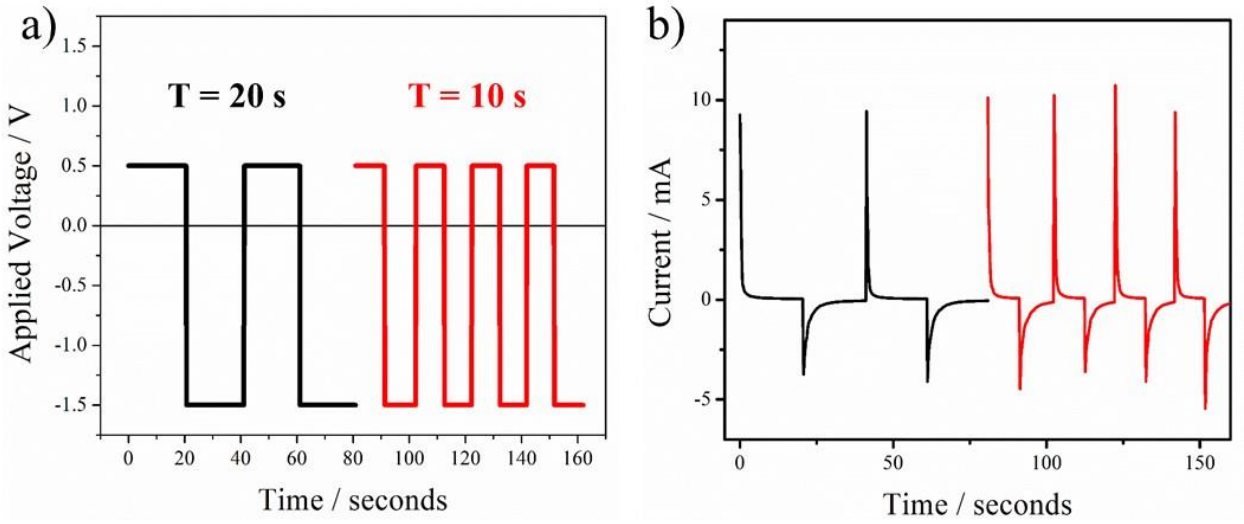

Figure 5.5 a) Potential waveform with varying time periods applied to the DADM structure. b) Corresponding current response to the potential waveform in (a) demonstrating no change in the cycling performance of the device.

The electrochromic community have developed highly efficient solid electrolytes with ionic conductivities comparable to or higher than those of conventional liquid electrolytes, opening a path towards all-solid-state electrochromic devices.[199-202] The results demonstrated in this work highlight the effectiveness of embedding electrochromic materials in structural color devices to generate low-power and multi-state tunable colors. Using the concept of solid electrolytes, this work can further be extended to generate entirely solid-state tunable color devices. The only requirement for the solid electrolyte in this case would be that it needs to be thin (< 100 nm), in order to not excite additional resonance modes in the structural color device that can impede the color appearance of the device.

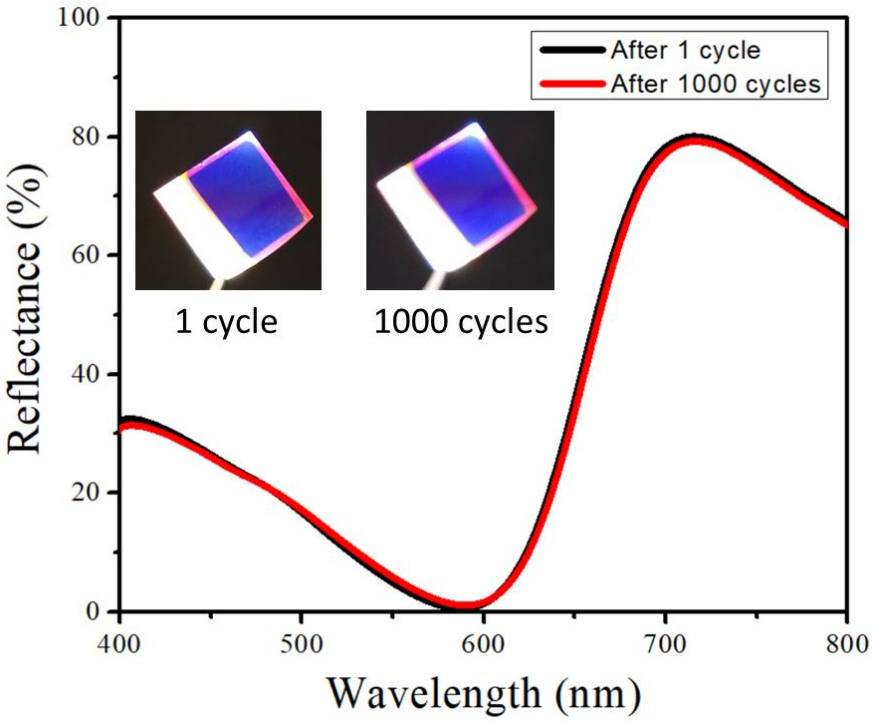

Figure 5.6 Measured reflectance of the DADM device in its blue colored optical state after the 1st and 1000th cycle. Insets are photographs the corresponding device. The size of each sample is 1.5 cm × 2.0 cm.

5.5 Conclusion

In summary, we have demonstrated a simple design technique for generating reconfigurable tunable structural colors with multiple optical colored states using a facile electrochemical approach. The tunable structural colors are designed based on multilayer DADM F-P resonators, where an electrochromic thin-film is used as the top dielectric layer. The refractive index of the electrochromic thin-film is readily modulated on application of a small potential bias in the presence of metal ions so as to induce a reconfigurable color change. The electrochromic tactic applied here has the important advantage of low-power consumption while demonstrating multiple colored states covering a wide area of the CIE chromaticity diagram. The proposed

devices exhibit excellent stability and switching performance, where high brightness and color purity of the tunable colors was maintained even after 1000 cycles. Further investigations are needed to incorporate solid-electrolyte thin-films into the structure presented here in order to realize all-solid-state low-power consumption multi-state tunable structural colors based on similar design principles.

Chapter 6

Accuracy of Kinetic Measurements at Individual Recessed Ultramicroelectrodes (UMEs)†

6.1 Introduction

With the development of micro- and nanoelectrochemical platforms, the scope of studying charge transfer processes has drastically increased.[203, 204] At inlaid disk-shaped ultramicroelectrodes (UMEs) and nanoelectrodes, radial diffusion and fast mass transport conditions at the smallest of electrodes have enabled accurate and precise measurements of fast electron transfer kinetics and mechanisms.[205-210] This is simplified through the knowledge of an analytical expression for the full steady state response of an inlaid disk UME which can be used to fit experimental results for the heterogeneous electron transfer rate constant, k^0, and the transfer coefficient, α.[211, 212] For example, the facile fabrication of inlaid disk electrodes through laser-pulling,[206] electrochemical etching,[213] or a combination of the two,[208] have resulted in electrodes on the scale of several nanometers. Figure 6.1 illustrates a schematic of an iridium (Ir) UME. However, the fabrication methods for inlaid UMEs typically require materials that are available in

† All finite-element simulations presented in this chapter were performed by Saurabh Acharya. Data analysis and figure construction for this chapter were performed by Saurabh Acharya and Mitchell Lancaster (equal contributing). Stephen Maldonado was the principal investigator for this project.

a wire format, have melting points compatible with heat sources and desired insulating materials.[214] Metals such as platinum and gold fit these requirements well, but semiconductors in general are incompatible with the aforementioned fabrication methods.

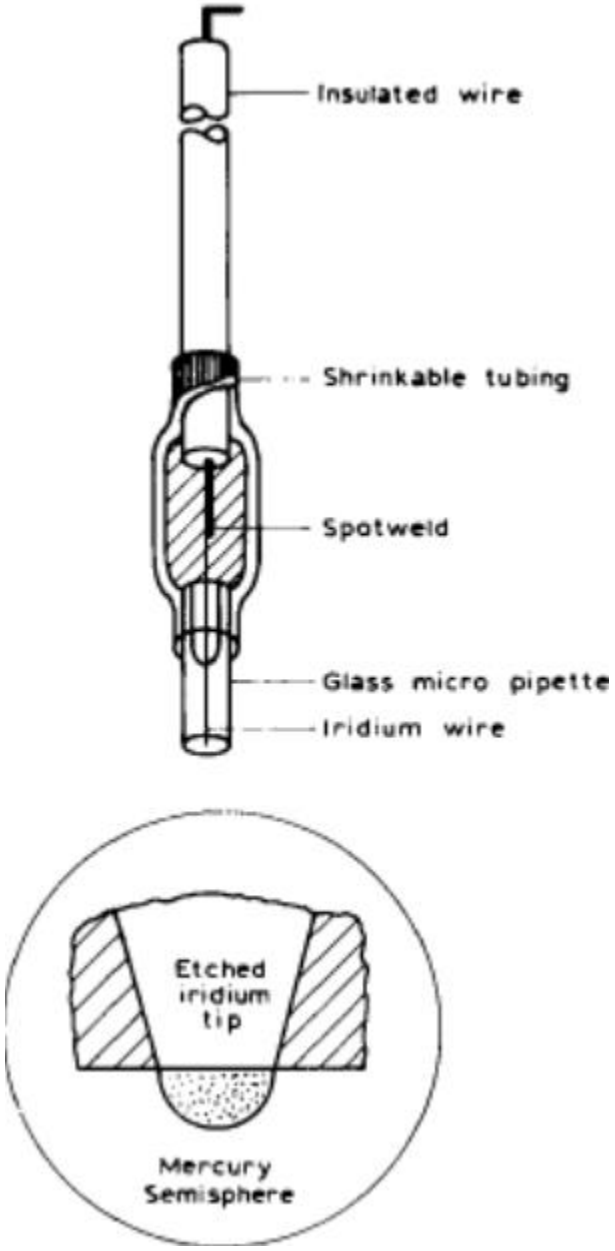

Figure 6.1 Design schematic of an inlaid UME using an Ir wire. (Kounaves, S.P., *Platinum Metals Rev.*, 1990, 34 (3), 131-134)

A surprisingly unexplored concept in semiconductor electrochemistry is to employ recessed semiconductor ultramicroelectrodes (SUMEs). In contrast to inlaid UMEs, recessed SUMEs can readily be fabricated with essentially any electrode material through common photolithographic methods. Theoretical and experimental examinations of the diffusion-limited (steady-state) current for recessed disk electrodes of different geometries have been conducted,[215-220] and the full voltammetric response has been simulated,[219, 221, 222] but an encompassing analytical expression describing the full voltammetric response has not yet been presented. This is partially due to the difficulty in describing the transport conditions within the well and at the mouth of the recession for the wide variety of recession/radius ratio geometries possible. Thus, there is a need for a broader and more rigid study that would help guide the fabrication and use of SUMEs for accurate charge-transfer measurements at semiconductor/liquid junctions.

To solve this issue, in this chapter, finite element simulations are used to explore the possibility of using a recessed UME geometry in which the difference in diffusion conditions between it and an inlaid UME are essentially negligible. This would allow accurate use of the already available expression for the voltammetric response of an inlaid disk UME for specific combinations of recessed UME recession depth and electrode radius. The accuracy of using inlaid disk transport assumptions for recessed disk UMEs as a function of recession depth (L), electrode radius (r), the standard heterogeneous rate constant (k), and the transfer coefficient (α) is presented.

6.2 Simulated Voltammetric Responses of Individual Inlaid and Recessed UMEs

6.2.1 Simulations

COMSOL Multiphysics (v4.4) was used to simulate the transport of redox species to the electrode surface for the model geometry shown in Figure 6.2. In this work the electrode radius, r, was either 50 µm, 5 µm, or 0.5 µm. For each electrode size, the recession depth, L, was varied between 0-10 µm. Only diffusion-controlled transport was considered, as an unstirred solution with a large concentration of supporting electrolyte was assumed. Relevant parameters and constants are shown in Table 6.1.

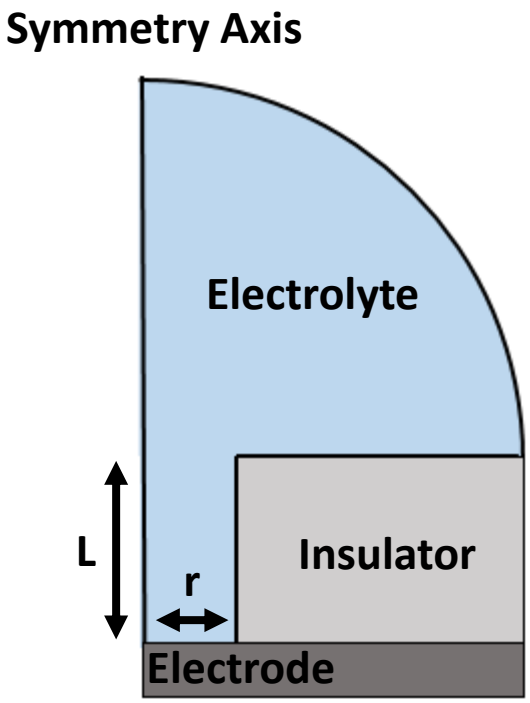

Figure 6.2 Two-dimensional geometrical model for the recessed disk ultramicroelectrode simulations. L represents the recession depth and r denotes the exposed electrode radius. The hemispherical electrolyte boundary is not drawn to scale.

The simulated voltammetric responses of individual inlaid and recessed UMEs in this work involve a one-electron transfer process:

$$O + e^- \rightleftharpoons R \tag{6.1}$$

The forward and reverse heterogeneous rate constants, k_f and k_b, are described through Butler-Volmer kinetics by:

$$k_f = k^0 \, exp\left[-\alpha \frac{F}{RT}(E - E°)\right] \tag{6.2}$$

$$k_b = k^0 \, exp\left[(1 - \alpha) \frac{F}{RT}(E - E°)\right] \tag{6.3}$$

where k^0 is the standard heterogeneous rate constant, α is the transfer coefficient, F is the Faraday constant, R is the molar gas constant, T is the temperature, E is the applied potential, and E° is the formal/standard potential. Diffusion in this system can be described through Fick's second law in two-dimensional cylindrical coordinates:

$$\frac{\partial c}{\partial t} = D\left(\frac{\partial^2 c}{\partial r^2} + \frac{1}{r}\frac{\partial c}{\partial r} + \frac{\partial^2 c}{\partial z^2}\right) \tag{6.4}$$

where c is concentration, t is time, r is the direction radial from the electrode surface, and z is the direction normal to the electrode surface. The boundary conditions are as follows. Initially, the concentration of the oxidized form of the redox couple, c_O, is equivalent to the bulk concentration, c*, and the reduced form of the redox couple, c_R, is not present:

$$c_O = c^* \tag{6.5}$$

$$c_R = 0 \tag{6.6}$$

These conditions hold throughout the model geometry. An infinite domain was used as the electrolyte boundary where the concentration of both species approached their bulk values at all time instants. Once a potential is applied to the electrode the flux of the oxidized and reduced species can be described through:

$$D_O \left[\frac{\partial c_O}{\partial t}\right] = -D_R \left[\frac{\partial c_R}{\partial t}\right] \quad (6.7)$$

where D_O and D_R are the diffusion coefficients of the oxidized and reduced forms of the redox species present in solution, respectively. The flux to all insulator/electrolyte boundaries is zero and described by:

$$D_O \left[\frac{\partial c_O}{\partial t}\right] = 0 \quad (6.8)$$

A Butler-Volmer formalism can be used to describe the current, i, at all points on the electrode surface through:

$$D_O \left[\frac{\partial c_O}{\partial t}\right] = k_f c_O - k_b c_R = \frac{i}{FA} \quad (6.9)$$

with the other variables being as defined above. Because the disk shape may have non-uniform accessibility depending on the geometry, the current is integrated over the entirety of the electrode radius to obtain the total current across the interface:

$$i_{tot} = 2\pi F D_O \int_0^r \frac{\partial c_O}{\partial t} r \, dr \quad (6.10)$$

To accurately resolve current near the electrode surface and insulator boundaries, a custom, fine mesh was used near the electrode surface and insulator/electrolyte boundaries. Absolute limiting currents of the simulated voltammograms for electrodes with no recession were within ~1% of the Cottrell prediction for all simulations in this work. Extraction of kinetic parameters

requires a normalized current response, so all simulated voltammetric responses shown in this text are normalized to cathodic limiting current values.

Table 6.1 Parameters used for finite element simulations.

Symbol	Definition	Simulation Value
L	Recession Depth	0-10 μm
r	Electrode Radium	0.5, 5, or 10 μm
c*	Bulk Concentration of Oxidized Species	1 mM
E°	Standard/Formal Potential	0 V vs. Reference
D_O	Oxidized Species Diffusion Coefficient	$1x10^{-5}$ cm/s
D_R	Reduced Species Diffusion Coefficient	$1x10^{-5}$ cm/s
K	Heterogenous Rate Constant	1, 0.01, 1e-5 cm/s
T	Temperature	298 K

6.2.2 Fitting

The voltammetric response of an inlaid disk electrode for a quasi-reversible redox system has been described by the classical "Bond-Oldham-Zoski" equation[211, 212]

$$\frac{J}{J_L} = \theta^{-1}\left[1 + \frac{\pi}{\theta\kappa}\left(\frac{2\kappa\theta+3\pi}{4\kappa\theta+3\pi^2}\right)\right]^{-1} \quad (6.11)$$

where J is the current density and J_L is the limiting current density at large negative overpotentials, κ and θ are parameterized terms relating kinetics and transport through

$$\theta = 1 + \frac{D_O k_b}{D_R k_f} \quad (6.12)$$

$$\kappa = \frac{\pi k_f}{4D_O} \qquad (6.13)$$

where k_f, k_b, D_O and D_R have the same meaning as described above. This expression was chosen for this work as it has been a common means to fit the entire voltammetric response for an inlaid disk ultramicroelectrode for direct determination of the heterogeneous rate constant and transfer coefficient for an electron transfer process. A recent modification to Equation *6.11* has been made to account for poised solutions,[212] eliminating E° as an unknown variable. However, here it is assumed the standard/formal potential is known (see Table 6.1).

6.3 Results and Discussion

Figure 6.3 shows the simulated voltammetric responses of a 50, 5 and 0.5 µm radius UME with recession depths between 0 µm and 10 µm for rate constants of (a) 1 cm/s, (b) 0.01 cm/s, and (c) $1x10^{-5}$ cm/s and transfer coefficients of 0.5. These values were chosen to approximate reversible, quasi-reversible, and irreversible electrons transfer kinetics, respectively. The general trend is that, as the rate constant decreases and/or as the L/r ratio increases, deviations from the inlaid disk case become apparent, especially for the slowest of charge transfer processes. Two observations are apparent – (1) There is an overall shift in the voltammetric responses to more positive potentials as the rate constant is decreased (2) For a given rate constant, the half-wave potentials of the voltammetric responses shift more negative as the L/r ratio is increased.

For a reversible reaction with a rate constant of 1 cm/s, the shape of the normalized responses of 50 and 5 µm radius UMEs are relatively insensitive to the geometry of the recession (L/r ratio) (Figure 6.3 a (I), b (I) and c (I)). Here, the half-wave potential for all recession depths are essentially the same as the standard potential for the redox reaction. However, the simulated

response for a 0.5 µm UME shows dependence on the recession depth. In this case, there is a slight shift of the curves to a less positive half wave potential for all recession depths with an increase in slope with larger L/r. This suggests the voltammetric response of recessed UMEs shows some sensitivity to reversible kinetics at the largest of L/r ratios.

For both a quasi-reversible and an irreversible reaction with a rate constant of 0.01 cm/s and $1x10^{-5}$ cm/s respectively, the half-wave potential is shifted more positive from the standard potential for the redox reaction for all three radii UMEs with L = 0, however the degree of this positive shift gets stronger as the radius of the electrode is reduced. Additionally, as the L/r ratio increases, the deviation of the simulated responses from the inlaid disc UME becomes more significant and the curves become increasingly less positive with steeper slopes (Figure 6.3 a (I & II), b (I & II), c (I & II)). This indicates a decrease in the overpotential required to drive the simulated reaction. These shifts as a function of recession depth describe the movement of the classical steady-state voltammetric curves for quasi-reversible and irreversible charge transfer with an increasing charge transfer rate constant. This result indicates an increase in the apparent rate constant relative to the inlaid disk case for increasing recession depths.

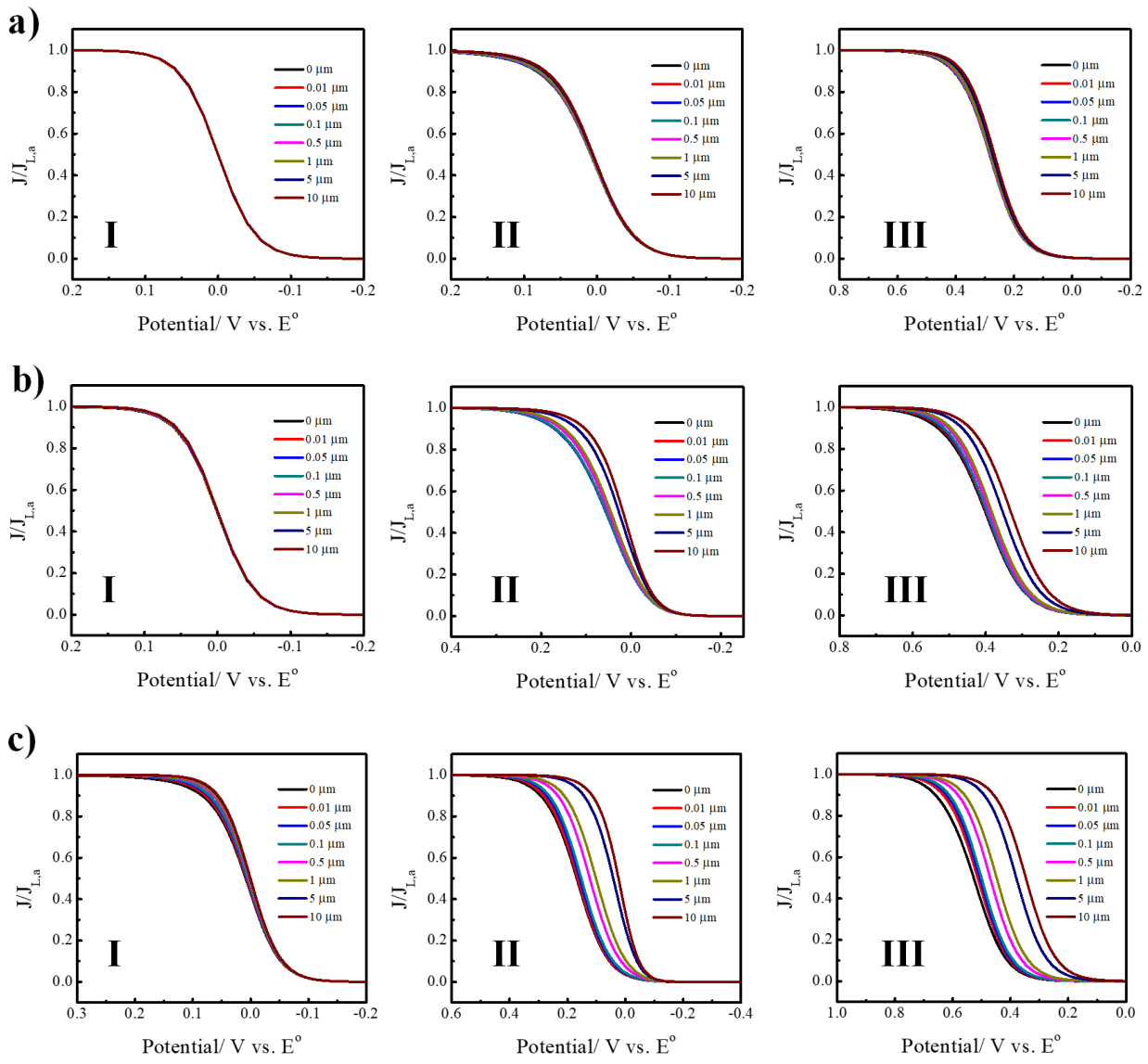

Figure 6.3 Normalized simulated voltammetric response for (a) 50 µm (b) 5 µm and (c) 0.5 µm disk UMEs with recessions depths of 0-10 µm. The simulated heterogeneous rates constants were (I) 1 cm/s (II) 0.01 cm/s and (III) 10^{-5} cm/s. For these simulations, α=0.5.

To assess the accuracy of rate constant determinations with recessed UMEs, the voltammetric responses presented in Figures 6.3 were fit to equation 6.*11*, and the apparent rate constant, k^0_{fit}, extracted was compared to the input rate constant for the simulations, k^0_{sim}, as a

function of L/r ratio. Figure 6.4a shows the deviation of the apparent rate constant from the simulated rate constant as a function of L/r ratio for 50 µm, 5 µm, and 0.5 µm UME radii. For this case, the simulated rate constant was approximately quasi-reversible, at 0.01 cm/s. At an L/r ratio of zero (i.e. an inlaid disk electrode) the rate constant ratio was near 1, indicating no deviation in the fitted value compared to the "true" rate constant. As the recession depth increases, the rate constant ratio steadily begins to rise, with an exception for the 0.5 µm electrodes with L/r = 0.02. At small L/r ratios (L/r < 0.02), this increase is not quite linear, but a further increase in recession depth provides an almost linear increase in the rate constant error. This emphasizes, for the quasi-reversible case, the apparent rate constants obtained from the fit are almost always larger as the electrode recession increases, but the degree of overestimation depends heavily on the electrode size. For example, at L/r = 0.1, the rate constants for 0.5 µm and 5 µm UMEs are overestimated by 5% and 17%, respectively. However, at a 50 µm UME with the same L/r ratio, the overestimation is greater than 46%.

A similar plot of the fitted to simulated rate constant ratio vs. L/r ratio for an irreversible rate constant of $1x10^{-5}$ cm/s is shown in Figure 6.4b. At L=0, only the 50 µm UME has a rate constant ratio near 1, while both the 5 µm and 0.5 µm UMEs have apparent rate constants that are overestimated. In contrast to the linear-type profile seen in Figure 6.4a, the rate constant ratio for this case initially decreases to a minimum value at 0.10 for all UME radii, before beginning a linear increase. This indicates at low recession depths the rate constant is underestimated, while at very large electrode recessions, the rate constant may be overestimated. Underestimation of the rate constants in this case, however, is unusual. Even with a lower charge transfer rate constant, the transport phenomena as a function of recession should still be applicable, although to a possibly smaller extent. A more likely explanation for this observed decrease in fitted rate constant relative

to the simulated rate constant is poor applicability of the expression for quasi-reversible electrode kinetics to an irreversible case. The limitations of using a quasi-reversible kinetic model for processes that approach reversible kinetics have been discussed elsewhere,[223] but no such description has been made for kinetic determinations near the irreversible limit.

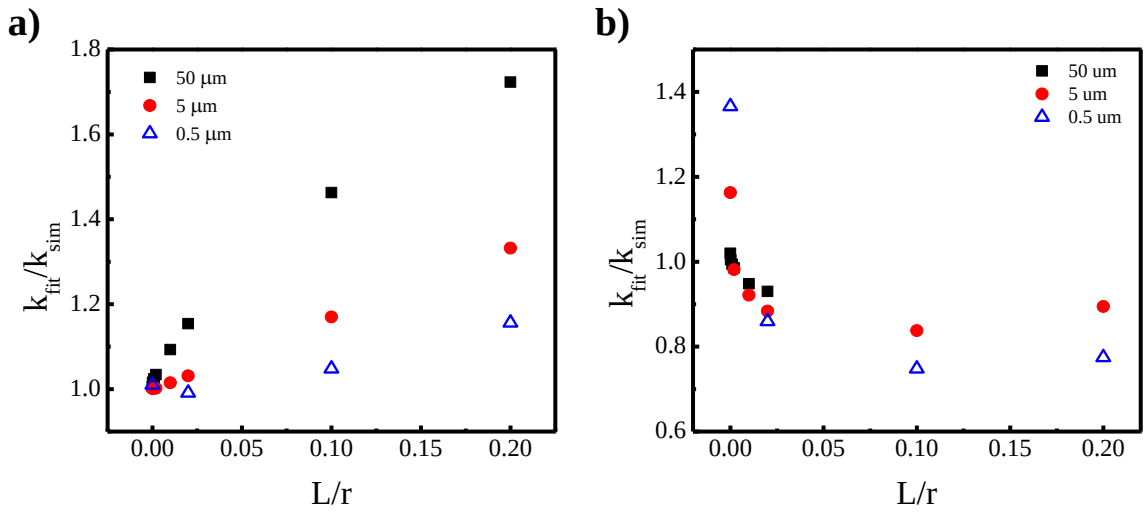

Figure 6.4 Deviation of fitted rate constant values (k_{fit}) from simulated values (a) k_{sim}=0.01 cm/s and (b) k_{sim}=0.00001 cm/s for recession-radius ratios of 0-0.2.

The cumulative data show that an increase in recession depth for recessed UMEs can result in either overestimation or underestimation of the rate constant depending on the specific recession geometry employed. For an approximately quasi-reversible rate constant of 0.01 cm/s, the fitted rate constants are typically larger than the simulated rate constant. The phenomenon of rate constant overestimation at recessed UMEs has been previously attributed to a "lagoon effect" in which electroreactant becomes trapped in the recession due to a smaller cavity entrance than electrode diameter.[224, 225] The simulations considered here are performed with geometries where the insulator walls are normal to the electrode surface, although similar overestimation can occur

in this geometry from the ability of recessed UMEs to reach a steady-state quicker than their inlaid counterparts. For these systems, the diffusion-limited current decreases with increasing recession.[215, 216] When normalized versus the limiting current value, J_L, the voltammetric response appears steeper, resulting in the larger apparent rate constants.

The results presented here provide some guidelines for the design and fabrication of recessed UME platforms for kinetic measurements through microfabrication techniques. For measurement of a quasi-reversible redox system at a 50 μm radius recessed UME, an insulating layer thickness of less than 500 nm is needed to measure rate constants within ~10% of the true value. Staying within that same error range at a 5 μm radius recessed UME would require insulating layer thicknesses no larger than approximately 350 nm. Finally, at a 500 nm radius UME, a recession depth no deeper than 75 nm would be required to avoid overestimating the rate constant by greater than 10%. The trend described shows a much slower decrease in the insulator thickness (compared to UME radius) necessary to maintain a certain error tolerance for smaller electrode radii. The physical origin of this trend is unclear, but it is unusual in the fact that the 50 μm recession curves deviate from the inlaid disk case much less than the smaller electrodes. A possible explanation is from the complex radius dependence on the recessed steady-state current.[215] Accordingly, the current magnitude difference between an inlaid disk electrode and recessed electrode with a defined L will change for different electrode radii. When normalized, these differences manifest themselves in the curves shifts shown in Figures 6.3 and 6.4.

Figure 6.5 shows how the fitted transfer coefficient, α_{fit}, is affected by increasing electrode recession depth for a "true" α value, α_{sim}, of (a) 0.25, (b) 0.5 and (c) 0.75 and k=0.01 cm/s. All three cases have a similar profile. For an inlaid disk in (a), (b) and (c), the apparent α values are within 1% of the simulated value. As the electrode becomes recessed, a sharp increase in the fitted

α is observed in both cases, but the deviation stays below 8% for $L/r < 0.2$. At larger recession depths, the apparent α begins to level out at approximately 10% deviation from the true value for all cases shown here.

For "true" transfer coefficients of 0.25, 0.5 and 0.75, the fitted value can be found within 10% if the recession depth is no larger than the electrode radius. While the tolerance for α based on UME geometry is much larger than for k, measurements of these parameters are typically coupled, suggesting the more stringent requirements for UME geometry during rate constant measurements should be followed. An interesting observation for both cases with the fitted values for α is the leveling off at about 10% for $L/r > 1$. This demonstrates a limited range of α for a single k value. The physical origin for this is unclear, but the sigmoidal shape of the voltammetric response of a UME can only tolerate a finite shift in α for a constant rate constant. The transfer coefficient strongly influences the shape of the curve at the foot and top of the wave. These areas can only be affected so much before needing the steepness and position of the curve to induce further change.

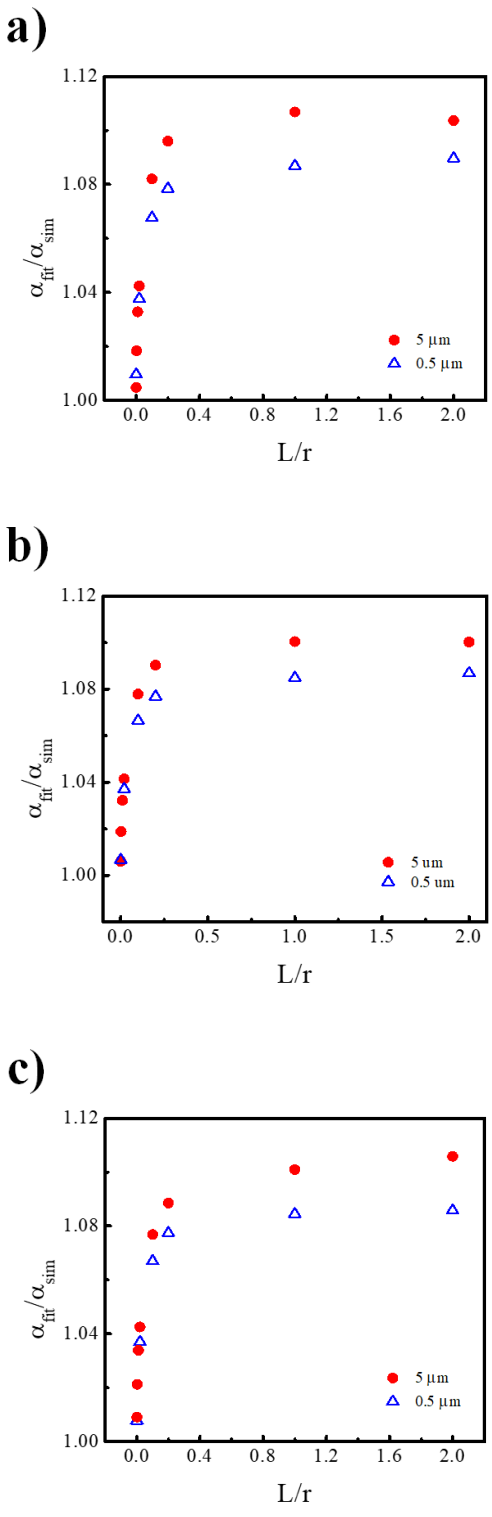

Figure 6.5 Deviation of fitted transfer coefficient values (α_{fit}) from simulated values (a) α_{sim}=0.25, (b) α_{sim}=0.5, and (c) α_{sim}=0.75 for recession-radius ratios of 0-2.0. For these simulations k=0.01 cm/s.

Although the allowable L/r ratio for measuring rate constants and transfer coefficients within a certain error range increases with decreasing electrode size, the above tolerances identify some important limitations and concerns for kinetic measurements at the smallest of recessed and inlaid UMEs. First, for the fabrication of recessed UMEs by common photolithographic methods, the smallest recession depth is defined by the smallest thickness of the insulating layer in which no tunneling occurs. For example, a high-quality SiO_x layer will be completely insulating (assuming a minimum number of defects) at a thickness of at least 10 nm. Although this work does not explicitly approach dimensions that small, it can be estimated from the results that the minimum radius of electrodes in which the apparent rate constant is within 10% of the true value would be no less than ~50 nm.

A second insight this work affords with regards to kinetic measurements is the importance of characterizing the electrode geometry, especially at electrochemically etched and laser pulled nanoelectrodes. With the recent push to measure extremely fast rate constants through the fabrication of < 20 nm electrodes, the characterization of the electrode/insulator interface has become challenging. A recent application of atomic force microscopy (AFM) has been shown to enable precise characterization of these nanoelectrodes.[226] At small size scales, any recession is bound to have a significant effect on the accuracy of rate constants measured. Although electrode recession sometimes cannot be avoided, it is important to recognize the possible error introduced into kinetic measurements by the chosen platform. Using characterization techniques such as AFM, coupled with the above analysis of recession geometry effects on measurement kinetic parameters, should allow for a better-defined error tolerance and possibly, more accurate rate constant and transfer coefficient measurements.

6.4 Conclusion

To summarize, the work described in this chapter explicitly describes the magnitude of error associated with using an individual recessed disk UME for kinetic measurements. Through finite element simulations it is shown the rate constant could be overestimated or underestimated depending on the recession geometry. The degree of rate constant deviation from an inlaid disk electrode depends largely on both the electrode size and recession depth. The transfer coefficient shows lower error over small recession depths, but the error levels out as the recession depth increases. The accuracy of kinetics parameter determination with recessed electrodes shown here should allow for design and fabrication of UMEs that either minimize error associated with extracted rate constants and transfer coefficients or have known error values associated with the fitted parameters. Such a description will allow the use of recessed UMEs with appropriate geometries for accurate kinetic measurements and will thus open the doors for use of rarely-utilized electrode materials for charge transfer kinetics studies.

Chapter 7

Semiconductor Ultramicroelectrodes (SUMEs): Platforms for Studying Charge-Transfer Processes at Semiconductor/Liquid Interfaces

Acharya, S.*; Lancaster, M.*; Maldonado, S. *Anal. Chem.*, **2018**, *90 (20)*, 12261-12269 [†]

7.1 Introduction

Unlike in a metal, the surface concentration of charge carriers in a semiconductor electrode is a complex function of the applied potential.[59, 227] This aspect substantially convolutes the influences of charge-transfer kinetics and mass transport on voltammetry with semiconductor electrodes, rendering the established methods for analyzing voltammetry data useless. Although the rotating disk motif can impart well-defined mass transport conditions to macroscopic semiconductor electrodes,[37, 228-230] such platforms are sufficiently cumbersome that repetitive studies where bulk (e.g. doping, mobility, charge-carrier lifetimes) and surface (e.g. roughness,

[†] Experiments, data analysis, and figure construction for this chapter were performed by Saurabh Acharya and Mitchell Lancaster (equal contributing). Saurabh Acharya prepared all SUME platforms. Stephen Maldonado was the principal investigator for this project.

chemical functionality, trap state density) properties are systematically varied are precluded. Consequently, new electrochemical strategies are needed to advance fundamental and applied understanding of charge transfer at semiconductor/electrolyte junctions.

The previous chapter detailed the recessed UME geometries for which the inlaid UME transport assumptions are still valid. In this chapter, we specifically apply the findings of the previous chapter to semiconductor ultramicroelectrodes (SUMEs) to develop a platform to accurately study charge-transfer processes at semiconductor/liquid junctions. Employing SUMEs greatly simplifies the voltammetry analysis, as the interplay between mass transport and charge-transfer kinetics can be well defined. We fabricate, demonstrate and validate a specific type of SUME platform amenable for detailed study and widespread use for any semiconductor material. Specifically, we demonstrate that a small, circular pinhole photolithographically patterned in a thin dielectric coating on an otherwise flat, clean single-crystalline semiconductor substrate can act as a recessed disk ultramicroelectrode (Figure 7.1). This design is advantageous because (*1*) it can be used with any semiconductor material available in planar form, (*2*) it obviates the need to mechanically process (polish) the semiconductor surface, and (*3*) it can be mass-produced for repetitive measurements. Further, this design is amenable to precise and facile control of electrode dimensions, a factor that can be exploited intentionally if care is taken during fabrication.

Herein, this chapter reports the quantitative and analytical utility of pinhole SUME platforms for studying charge-transfer processes at semiconductor/electrolyte contacts. Several aspects of SUMEs are discussed, including an explicit description of how the doping concentration, charge-transfer kinetics, mass transport, and the extent of depletion within the semiconductor impact voltammetric responses of n-type SUMEs.[231] Experimentally measured responses of SUMEs prepared with single-crystalline n-Si are also provided, highlighting their sensitivity

towards the dynamic nature of the Si/water interface. In addition, the responses of n-Si SUMEs are analyzed to elucidate measurements of interfacial charge-transfer rate constants of Si in aqueous electrolytes.

7.2 Experimental Methods: Fabrication of SUMEs, Electrochemical Measurements and Reorganization Energy Calculation

7.2.1 SUME Fabrication

All substrate wafers were subject to the RCA cleaning process with a final dip in BHF for 30 seconds prior to initial use. The wafers were immediately introduced into a Spin Rinse Drier (Verteq SRD, Class One Equipment) and transferred into a low pressure chemical vapor deposition (LPCVD) furnace (Tempress Systems) for 150 nm silicon oxynitride (SiO_xN_y) deposition at a rate of 2.2 nm/min and T = 850 °C. Alternatively, for thicker insulator deposition, 600 nm silicon oxide (SiO_2) was deposited on the wafers by plasma-enhanced chemical vapor deposition (PECVD) (Ultradep 2000, GSI Lumonics) at a deposition rate of 18.6 nm/min and T = 350 °C, followed by rapid thermal annealing (Jetfirst RTP 150, Jipelec) in N_2 (g) at T = 800 °C for 5 minutes. Back ohmic contacts were formed by depositing Ti(10 nm)/Au(120 nm) using an e-beam evaporator (Evovac, Angstrom Engineering). Immediately prior to this step, back side SiO_xN_y from the LPCVD deposition was wet etched in BHF for 15 minutes (etch rate = 10 nm/min) while the SiO_xN_y on the top surface was protected by spincoating 1.5 μm of S1813 with a softbake at T = 110 °C for 4 minutes. Following back contact deposition, the top protective S1813 film was removed by immersing the wafer in Nano-Strip. The substrates were vapor primed with hexamethyldisilazane (HMDS) in a YES-310TA (E) oven and SPR 220 3.0 was then immediately

spincoated to an average thickness of 2.18 µm. The films were soft baked for 90 seconds at T = 115 °C. Projection photolithography (GCA Autostep 200, RZ Enterprises, Inc.) was used to expose (λ = 365 nm) the coated substrate through custom photolithography masks containing dies with r =1.5, 5, and 10 µm features at the center of individual dies. The pattern was then transferred to the underlying SiO_xN_y or SiO_2 film by reactive ion etching (RIE) (APS Dielectric Etch Tool, STS) with C_4F_8 (g). The etch rate was adjusted to 177.6 nm/min for SiO_xN_y and to 353.4 nm/min for SiO_2. To prevent any possible plasma damage to the Si surface in the SUME region, the RIE etch was stopped with 10-20 nm of SiO_xN_y or SiO_2 left in the features, which was then removed by wet etching in BHF. The wafers were diced into individual dies and the SPR 220 3.0 film was dissolved off in acetone and rinsed in 2-propanol prior to further use. This procedure produced SUMEs as shown in Figure 7.1b.

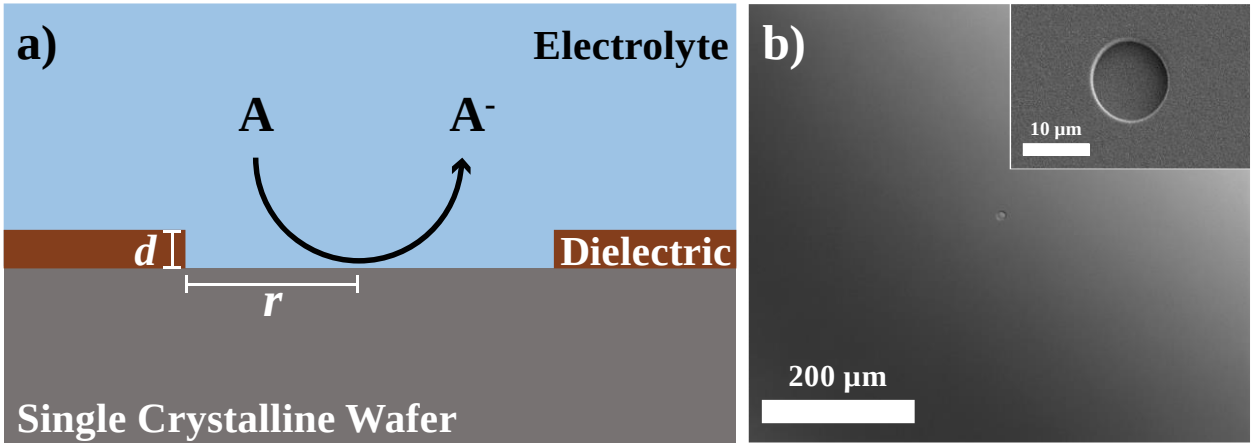

Figure 7.1 a) Cross-sectional view of an idealized SUME platform based on a defined pinhole in a thin dielectric coating on a planar semiconductor electrode. b) Large-area optical image of an n-Si SUME with r = 5 µm. Inset: Scanning electron micrograph at higher magnification of the same SUME.

7.2.2 Electrochemical Measurements

All voltammetric experiments were performed using CHI420A and CHI760C (CH Instruments) potentiostats in a custom-built, dark Faraday cage. The fabricated SUMEs were etched in BHF immediately before being placed in an open-air Teflon cell and sealed with a Viton o-ring (ID = 2.9 mm, McMaster-Carr). A three-electrode configuration with a Ag/AgCl (Sat'd KCl) reference and a flame-cleaned Pt wire counter electrode was used throughout.

Impedance (Mott-Schottky) measurements were taken using a Solartron 1286 electrochemical interface coupled to a model 1250 impedance analyzer (Ametek). A 10 mV sinusoidal AC potential with frequencies from 10 Hz to 52 kHz was applied over DC potentials ranging from -0.15 V to 0.7 V. Immediately before each measurement, bare n-Si electrodes (0.19 cm^2) were etched in BHF for 1 minute. The impedance data was fit with the Mott-Schottky equation to determine the flat-band potential of the semiconductor/electrolyte contact, E_{fb}

$$C_{sc}{}^{-2} = \frac{2}{q\varepsilon\varepsilon_o N_d A^2}\left(E - E_{fb} - \frac{k_B T}{q}\right) \tag{7.1}$$

where q is the unit coulombic charge, ε is the static dielectric constant of the bulk semiconductor, ε_o is the permittivity of free space, N_d is the bulk dopant concentration, A is the area of electrode exposed to solution, E is the applied DC bias, k_B is Boltzmann's constant, and T is temperature. From E_{fb}, the conduction band energy was calculated using the effective density of states in the conduction band, N_c

$$E_{cb} = E_{fb} + k_B T \ln\left(\frac{N_d}{N_c}\right) \tag{7.2}$$

where N_c = 2.8 x 10^{19} cm^{-3} for Si. The reported conduction band energies were averages from three different electrodes with the error corresponding to the standard deviations of those

measurements. To influence the band energetics at the semiconductor/electrolyte interface, both macroscopic and microscopic (SUME) n-Si electrodes were immersed in 5 mM $K_4Fe(CN)_6$ under ambient light for 5 minutes, followed by corresponding impedance and voltammetry measurements, respectively.

7.2.3 Reorganization Energy Calculation

The total reorganization energy for a redox couple at a semiconductor electrode, λ_{sc}, can be considered as the sum of inner-sphere, $\lambda_{sc,i}$, and outer-sphere, $\lambda_{sc,o}$ components[232]

$$\lambda_{sc} = \lambda_{sc,i} + \lambda_{sc,o} \tag{7.3}$$

which represent changes in bond lengths/angles and changes in solvation around the outer-coordination sphere, respectively. In the case of heterogenous charge-transfer reactions, the inner sphere contribution at a Si electrode can be approximated by half the inner-sphere reorganization energy for the corresponding homogeneous self-exchange reaction, $\lambda_{se,i}$.[232] The value $\lambda_{se,i}$, in turn, can be calculated by subtracting the self-exchange outer-sphere reorganization energy ($\lambda_{se,o}$) from the self-exchange total reorganization energy (λ_{se}), giving

$$\lambda_{sc} = \frac{\lambda_{se} - \lambda_{se,o}}{2} + \lambda_{sc,o} \tag{7.4}$$

where λ_{se} for $Ru(NH_3)_6^{3+}$, MV^{2+}, and $Co(sep)_3^{3+}$ are measurable quantities of 1.6,[233] 0.6,[234] and 2.6 eV,[234] respectively. $\lambda_{se,o}$ can be separately estimated by *eq 7.5*[232]

$$\lambda_{se,o} = \frac{q}{4\pi\varepsilon_0}\left(\frac{1}{a_i} - \frac{1}{2a_i}\right)\left(\frac{1}{{n_{H_2O}}^2} - \frac{1}{\epsilon_{H_2O}}\right) \tag{7.5}$$

where ε_0 is the permittivity of free space, a_i is the ionic radius of the redox probe (3.4,[235] 3.6,[234] and 4.5 Å[234] for $Ru(NH_3)_6^{3+}$, MV^{2+}, and $Co(sep)_3^{3+}$, respectively), n_{H2O} is the refractive index of water (1.34[236]), and ϵ_{H2O} is the static dielectric constant of water (78.46).[236] Similarly, $\lambda_{sc,o}$ can be calculated by *eq 7.6*,[237]

$$\lambda_{sc,o} = \frac{q}{8\pi\varepsilon_0}\left[\frac{1}{a_i}\left(\frac{1}{{n_{H_2O}}^2} - \frac{1}{\epsilon_{H_2O}}\right) - \frac{1}{2a_i}\left(\left(\frac{{n_{Si}}^2 - {n_{H_2O}}^2}{{n_{Si}}^2 + {n_{H_2O}}^2}\right)\frac{1}{{n_{H_2O}}^2} - \left(\frac{\epsilon_{Si} - \epsilon_{H_2O}}{\epsilon_{Si} + \epsilon_{H_2O}}\right)\frac{1}{\epsilon_{H_2O}}\right)\right] \tag{7.6}$$

where n_{Si} and ϵ_{Si} are the refractive index (3.8)[238] and static dielectric constant (11.7)[236] of Si, respectively.

7.3 Predicted Characteristics of Non-Degenerately Doped SUME Responses Under Depletion Conditions

This section explicitly describes how the doping concentration, charge-transfer kinetics, mass transport, and the extent of depletion within the semiconductor impact voltammetric responses of n-type Si SUMEs.

At sufficiently slow scan rates, the voltammetric response of an ultramicroelectrode far from any physical obstruction attains a steady-state *J-E* response that follows spherical rather than linear diffusional transport. Because the current tends to a limiting value when diffusion outpaces kinetics, the steady-state shape necessarily describes the competition between precisely defined mass transport and charge-transfer kinetics. One approach to interpret the voltammetric responses of disk ultramicroelectrodes is through finite-element[216] or numerical modeling[220] of the transport. Although descriptive and quantitative, this approach does not readily afford simple prediction of the features of a SUME electrode. A more convenient alternative method is through the analytical expressions described by the "Bond-Oldham-Zoski" equation.[211, 212] This expression was already introduced in the previous chapter (*eqs 6.11-6.13*), but is repeated below for consistency and ease of readability. In this analysis, the normalized current (i.e. dividing the measured current by the mass transport-limited cathodic current, $J_{L,c}$) follows *eq 7.7*,

$$\frac{J}{J_{L,c}} = \frac{1}{\theta\left[1+\frac{\pi}{\theta\kappa}\left(\frac{2\kappa\theta+3\pi}{4\kappa\theta+3\pi^2}\right)\right]} \qquad (7.7)$$

where θ & κ are dimensionless numbers that relate to the diffusion of the redox species and the governing rate constants at the electrode/electrolyte interface as shown in *eqs 7.8* and *7.9.*

$$\theta = 1+\frac{D_A}{D_{A^-}}\frac{k_b}{k_f} \qquad (7.8)$$

$$\kappa = \frac{\pi r k_f}{4D_A} \qquad (7.9)$$

In *eqs 7.8* and *7.9*, D_A and D_{A-} are the diffusion coefficients of the oxidized and reduced form of the redox couple, k_f is the rate constant for the reduction of *A* to A^-, and k_b is the rate constant for the oxidation of A^- to *A*. Typically, the potential dependence is ascribed by applying the Butler-Volmer formalism (*eqs 6.2* and *6.3*) to the values of k_f and k_b.[239] However, this approach assumes that the densities of charge carriers are constant and that the rate constants depend on potential. In a non-degenerately doped semiconductor electrode operating under depletion conditions, this is however not true and a different approach is needed to evaluate the rate constant terms.[23, 240]

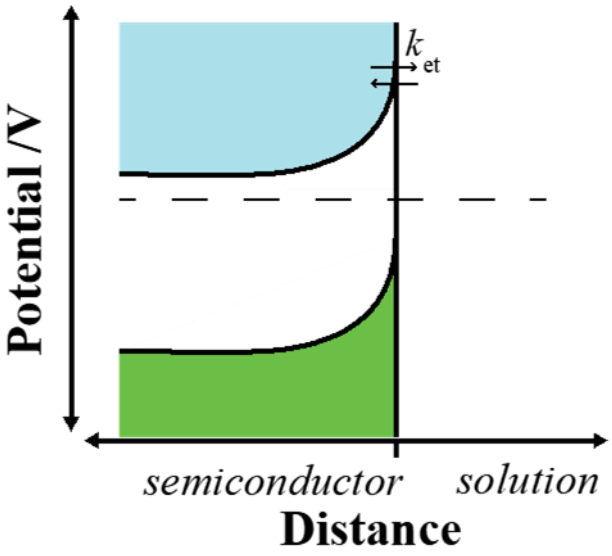

Figure 7.2 A schematic diagram depicting charge-transport process at a semiconductor/liquid junction.

For a non-degenerately doped n-type semiconductor electrode in the dark, the following expressions for k_f and k_b are appropriate in an unpoised electrolyte containing just one type of dissolved, reducible species, *A*. (Analogous expressions can be written for oxidation of A^- in the dark at a p-type semiconductor).

$$k_f = k_{et} n_s(E) \tag{7.10}$$

$$k_b = k_{et} n_{s,E^{0\prime}} \tag{7.11}$$

$$n_s(E) = n_{s,E^{0\prime}} e^{\frac{-q}{\gamma k_B T}(E - E^{0\prime})} \tag{7.12}$$

$$n_{s,E^{0\prime}} = N_{cb} e^{\frac{q}{k_B T}(E_{cb} - E^{0\prime})} \tag{7.13}$$

In these equations, $n_s(E)$ is the surface concentration of electrons (majority carriers) at potential E, $n_{s,E^{0\prime}}$ is the surface concentration of electrons at the formal potential ($E^{0'}$) of the redox species, N_{cb} is the effective density of states at the conduction band edge, E_{cb} is the conduction band edge potential, k_{et} ($cm^4\ s^{-1}$) is the rate constant for electron transfer from the conduction band edge of the semiconductor, and γ is the ideality factor of the semiconductor/electrolyte interface. All other terms have their usual meanings. Two implicit assumptions in *eqs 7.10-7.13* is that all the applied potential drops within the space charge region of the semiconductor and that charge-transfer occurs exclusively through one band (i.e. the conduction band for n-type materials).

With *eqs 7.7-7.13*, the steady-state voltammetric response of an n-type SUME can be readily understood as a function of E_{cb}, k_{et}, $E^{0'}$, and γ in the same manner that a single voltammetric response of a metal ultramicroelectrode is routinely modeled for the values of the charge transfer coefficient (α), the standard rate constant (k^0), and $E^{0'}$.[211, 239, 241] Importantly, although the term γ superficially has an analogous effect in describing current-potential responses as α does in Butler-Volmer kinetic theory, its meaning here is physically different. That is, γ is a quantitative measure of the quality of the semiconductor/electrolyte interface[242, 243] and has a value of precisely '1' when all of the applied potential is used to drive interfacial charge-transfer by thermionic emission of majority carriers at the band edge. Several distinct factors (e.g. potential drop at the double layer,[244] mass transport resistance,[245] the presence of charge traps at the surface[26]) can elicit $\gamma > 1$.

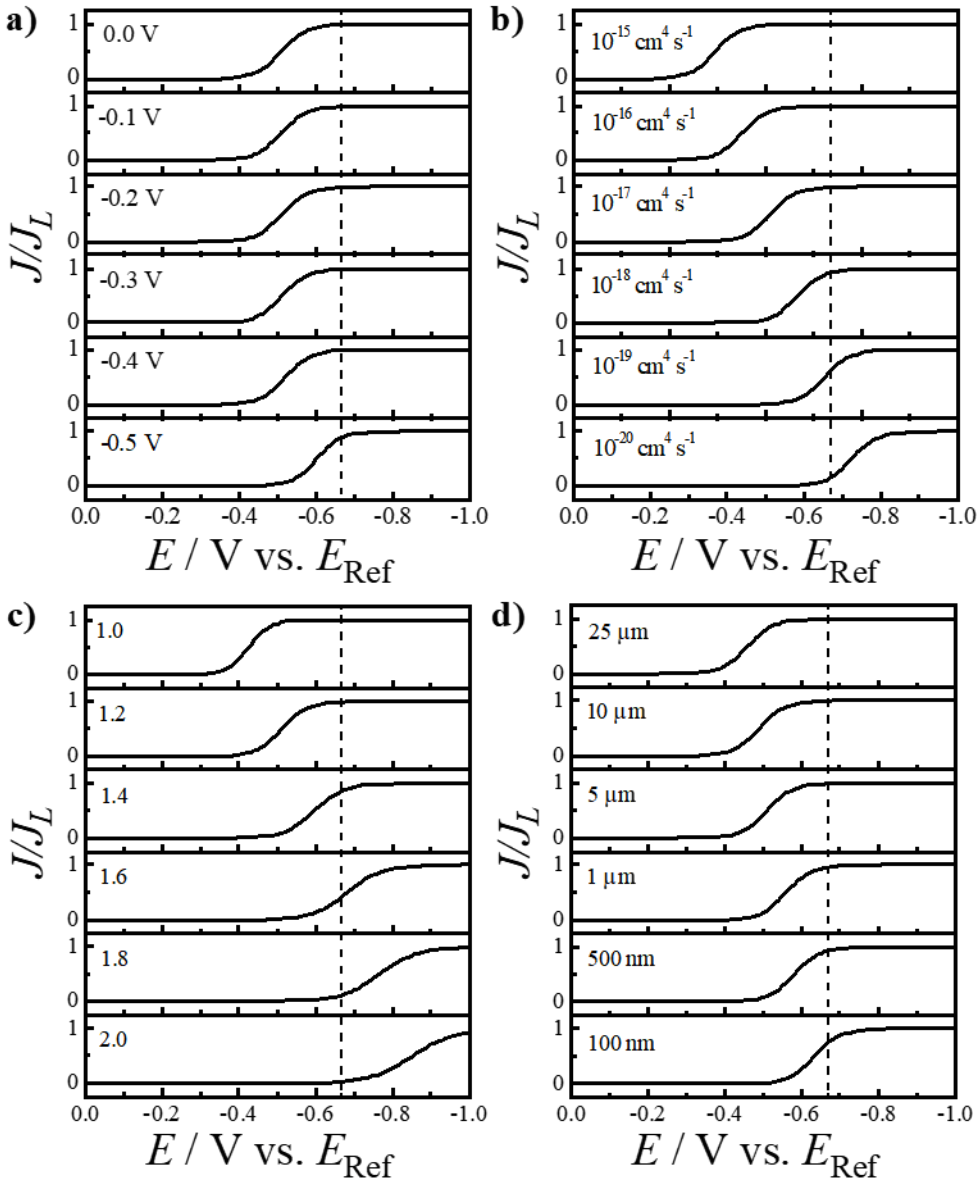

Figure 7.3 Modeled steady-state voltammetric responses of non-degenerately doped n-type SUME (N_D = 1 x 10^{15} cm^{-3}) based on equations *7.1-7.6* as a function of variation in the electron transfer rate constant (k_{et}), the standard potential of the redox couple ($E^{0'}$), the ideality factor (γ), and the disk radius (r). a) Variation in $E^{0'}$ with E_{cb} = -0.68 V, k_{et} = 10^{-17} cm^4 s^{-1}, γ = 1.2, and r = 5 µm. b) Variation in k_{et} with E_{cb} = -0.68 V, γ = 1.2, $E^{0'}$ = 0 V, and r = 5 µm. c) Variation in γ with E_{cb} = -0.68 V, k_{et} = 10^{-17} cm^4 s^{-1}, $E^{0'}$ = 0 V, and r = 5 µm. d) Variation in r with E_{cb} = -0.68 V, k_{et} = 10^{-17} cm^4 s^{-1}, γ = 1.2, and $E^{0'}$ = 0 V.

Figure 7.3 displays the predicted trends in voltammetric responses using the Bond, Zoski, and Oldham approach[239] while using our derived expression for k_f and k_b for n-type Si SUMEs with N_D = 1 x 10^{15} cm^{-3}. In these figures, the conduction band edge potential is denoted by the vertical dashed lines. Figure 7.3a illustrates the response for an n-type Si SUME as a function of $E^{0'}$. The most obvious and striking feature is that in strong contrast to metal ultramicroelectrodes, the normalized voltammetric responses are wholly *independent* of $E^{0'}$ when $E^{0'}$ is far from E_{cb} if all other model parameters are the same. The rationale is that in semiconductor electrodes, the surface concentration of majority carriers (electrons) depends on the potential with respect to E_{cb} rather than $E^{0'}$.[23, 246] As a result, the position of a single voltammetric response for a SUME gives little information on $E^{0'}$ but can be understood more readily in relation to E_{cb}. This feature has been a confounding aspect of conventional voltammetry with semiconductor macroelectrodes,[32-36, 38, 39] but is clear in the responses of SUMEs. In fact, for a non-degenerately doped SUME, voltammetric responses that are near $E^{0'}$ imply that $E^{0'}$ is near E_{cb}.

Figure 7.3b shows the predicted response at an n-type SUME for various redox couples with the same $E^{0'}$ values but different k_{et} values. Here, the position of the normalized voltammetric response with respect to the band edge is *strongly* sensitive to the value of k_{et}. Hence, the mere position of the current-potential response of a SUME is an indicator of the respective charge-transfer rate constant. Figure 7.3c presents the predicted sensitivity of n-type SUMEs towards variations in γ. Two aspects are readily apparent when γ is larger than 1. First, the voltammetric response is broadened significantly and the current onset is less steep, e.g. the potential at J/J_L = 0.5 occurs further from the potential of current onset when γ > 1. Accordingly, the shape of the voltammetric response is an immediate indicator of the quality of semiconductor/electrolyte interface. Second, the broadening incurred by γ > 1 shifts the entire, normalized voltammetric

response towards more negative potentials. This aspect means that estimation of k_{et} from the position of the voltammetric response cannot be performed without also assessing the value of γ. Figure 7.3d highlights how the normalized steady-state current-potential curves shift as a function of *r*. Smaller values of *r* result in higher attainable absolute current densities and also shift the normalized current-potential responses towards more negative potentials. Again, estimation of k_{et} from the position of the voltammetric response also cannot be performed without direct knowledge of *r* beforehand.

7.4 Analysis of Measured Characteristics of Si SUMEs

7.4.1 n-Si SUME Response Characteristics

Figure 7.4 highlights the measured doping- and size-dependent voltammetric responses of n-Si SUMEs with *r* = 1.5, 5, and 10 μm in an aqueous 0.1 M KCl electrolyte with dissolved $Ru(NH_3)_6^{3+}$ ($E^{0'}$ = -0.145 V vs. *E*(Ag/AgCl)). These curve shapes are dependent on the heterogeneous charge transfer rate constant, k_{et}, the conduction band energy, E_{cb}, and the surface quality, *γ*, which describes the dominant mode of recombination at the interface. Figure 7.4a shows a comparison of sigmoidal voltammetric responses for two separate Si SUMEs with *r* = 5 μm but different doping levels (i.e. non-degenerate vs degenerate doping). Tunneling of charge-carriers from the bulk through the narrow width of the depletion layer in the semiconductor is extensive in degenerately doped semiconductors, resulting in response characteristics similar to metallic electrodes.[247] The positions of the steady-state responses for the non-degenerately and degenerately doped SUMEs were significantly different. The voltammetric response of the degenerately doped n-Si SUME was centered at *E* = -0.25 V, i.e. close to the formal potential of

$Ru(NH_3)_6^{3+}$ as expected for a metallic ultramicroelectrode.[248] In contrast, the response of the non-degenerately n-Si SUME was shifted significantly to more negative potentials. Based on the trends shown in Figure 7.3 and a value of E_{cb} = -0.677 V (*vide infra*), these data implied $k_{et} > 10^{-17}$ cm^4 s^{-1}.

A common feature in both degenerately doped and non-degenerately doped Si SUME responses was appreciable capacitive currents, even at a scan rate of only 0.005 V s^{-1}. This residual capacitive current arose from the large total junction area (~ 0.07 cm^2) of the thin dielectric layer with the electrolyte. Similar stray capacitances were previously observed in metal-insulator-electrolyte nanoband electrodes when the dielectric does not fully screen the charge between the underlying electrode and electrolyte.[249, 250]

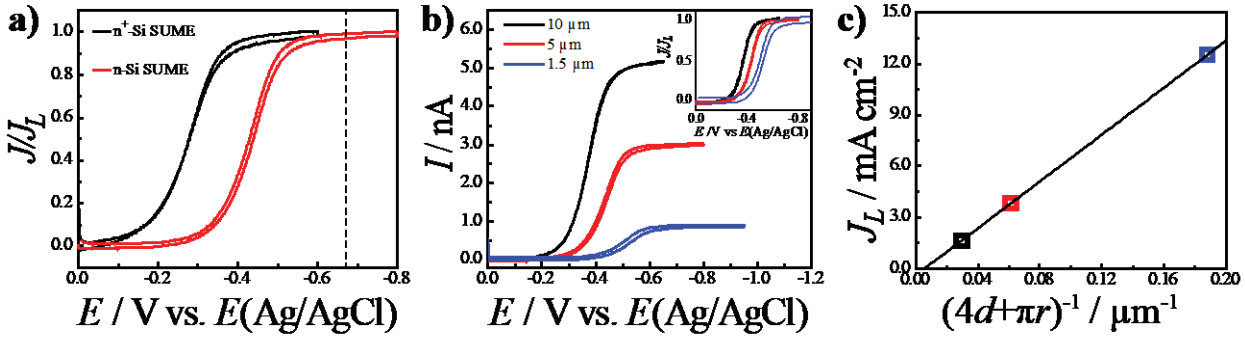

Figure 7.4 a) Normalized experimental voltammetric responses of 5 μm n$^+$-Si and n-Si SUMEs to 2 mM $Ru(NH_3)_6^{3+}$. The dashed line indicates the conduction band location determined from separate impedance measurements. Scan rate: at 5 mV s^{-1} b) Size-dependent voltammetry for n-Si SUMEs in 2 mM $Ru(NH_3)_6^{3+}$. The inset shows the normalized version of these plots. Scan rate: 5 mV s^{-1}. c) Plot showing the mass transport-limited current density for the curves in b) as a function of inverse radius.

Figure 7.4b compares the responses of n-Si SUMEs with different values of r in the same electrolyte, where the steady-state current magnitudes clearly tracked with r. Similarly, the normalized current-potential responses (Figure 7.4b inset) shifted as predicted from Figure 7.3. It must be noted that, for SUMEs with smaller r values, the dielectric thickness was similarly adjusted to maintain ratios of $d/r < 1$. That is, for SUMEs with r = 10 µm, a dielectric thickness of 0.6 µm was used while for SUMEs with r = 1.5 µm a thinner dielectric thickness of 0.150 µm was employed. Doing so resulted in the background capacitance being more pronounced in the voltammetry for the smallest SUMEs. The mass transport-limited current density tracked linearly with $(4d+\pi r)^{-1}$ (Figure 7.4 c), in accord with predictions for recessed disk ultramicroelectrodes described by *eq 7.14*,[211]

$$J_{L,c} = mq[A] = \frac{4D}{4d+\pi r} q[A] \qquad (7.14)$$

where m is the mass transfer coefficient, $[A]$ is the concentration of the species being reduced in solution, D is the diffusion coefficient of the species A, r is the electrode radius, and d is the dielectric thickness. The attainable mass transport rate at each SUME can be compared with the corresponding rotation rate needed for a rotating disk electrode to reach the same value (assuming a kinematic viscosity of 8.8 x 10^{-3} cm^2 s^{-1}, Table 7.1).[251] Notably, at r = 1.5 µm, the equivalent rotation rate (~140,000 rpm) is significantly larger than what is typically achievable with mechanical rotators, underscoring a potent advantage of SUMEs for enabling measurements at high current densities.

Table 7.1 Mass transport-limited current density and equivalent RDE rotation rate for n-Si SUMEs[a]

r / μm	J_L / mA cm^{-2}	Equiv. RDE Rate / rpm
10	1.64	2317
5	3.83	12663
1.5	12.5	135450

[a] Assuming a kinematic viscosity of 8.8 x 10^{-3} cm^2 s^{-1}

7.4.2 Sensitivity of SUME Response Towards Conditions at the Semiconductor/Liquid Interface

Some aspects of the steady-state voltammetric response for the reduction of $Ru(NH_3)_6^{3+}$ changed over time. Figure 7.5a shows the normalized voltammetric responses for a non-degenerately doped n-Si SUMEs as a function of time after first immersion of the electrode in the aqueous electrolyte. Cyclic sweeps were performed every 40-50 minutes with the electrode held in solution at open circuit between scans. Over the course of nearly 5 h, the shape of the current-potential response was unchanged while the response shifted to progressively more negative potentials, suggesting either a change in k_{et} and/or a shift in E_{cb}. Using the potential where the current was half the value of the mass transport-limited current, $E_{1/2}$, as a metric, Figure 7.5b shows the voltammetric responses shifted by just 45 mV over nearly 5 h. Corresponding measurements with degenerately doped n$^+$-Si SUMEs also showed time-dependent voltammetric responses. However, the shape of the normalized current-potential response changed noticeably in addition to shifting towards more negative potentials, reminiscent of metal ultramicroelectrodes with a tunneling barrier at the electrode surface.[252]

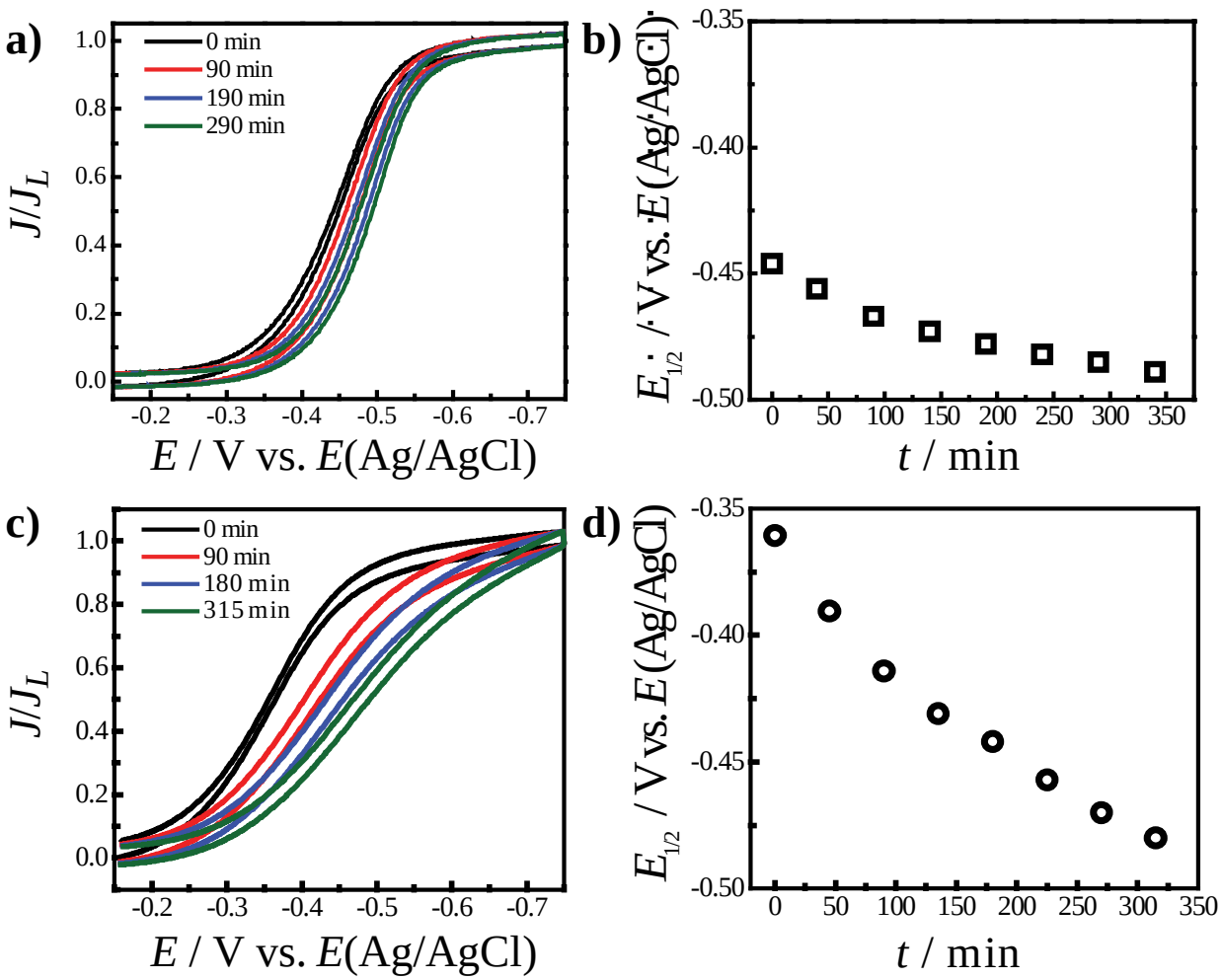

Figure 7.5 Time-dependence of normalized steady-state voltammetric responses of a) non-degenerately doped and c) degenerately doped Si SUMEs in 0.1 M KCl containing 2 mM $Ru(NH_3)_6^{3+}$ over time. Scan rate: 10 mV s^{-1}, r = 5 μm. Half-wave potentials of the SUME response for b) non-degenerately doped and d) degenerately doped Si SUMEs as a function of time.

The measured steady-state current-potential responses for the reduction of $Ru(NH_3)_6^{3+}$ at n-Si SUMEs shown here acted as a probe of the Si/water interface. The subtle, negative shift in the voltammetry in Figure 7.5 strongly implies that the surface of n-Si in water progressively changed over time. The most plausible cause was the growth of an appreciable surface oxide, as the oxidation of Si in water is well known.[253] Chemical oxidation of non-degenerate Si by water

yields a ~2 Å oxide (SiO_x) over 300 minutes[253] which could act as an additional tunneling barrier that slows heterogeneous charge transfer. Assuming that the observed 45 mV shift corresponded to solely a diminution in k_{et}, that shift implied a decrease in k_{et} by a factor of ~5. Such attenuation is consistent with tunneling through a thin SiO_x layer.[203,254] The changes seen with n^+-Si SUMEs further corroborates the contention that the voltammetric changes tracked the slow growth of surface oxide. The current flow at degenerately doped semiconductor interfaces is predominantly by tunneling of majority carriers through the space-charge region rather than thermionic emission at the band edge.[230] Accordingly, such current flow should be strongly affected by introducing another tunneling process. That is, a surface oxide imposes a second tunneling process in series, thereby lowering the probability that a charge-carrier escapes from the semiconductor into the solution and introducing an additional overpotential penalty for attaining the same current density. If the slow growth of surface oxide was instead just changing E_{cb}, tunneling through the space-charge layer within the semiconductor would be largely unaffected since small changes in band edge energetics do not alter the space-charge layer thickness. Hence, the voltammetric responses from both the non-degenerately and degenerately doped Si SUMEs are consistent with a thin surface oxide growing over time.

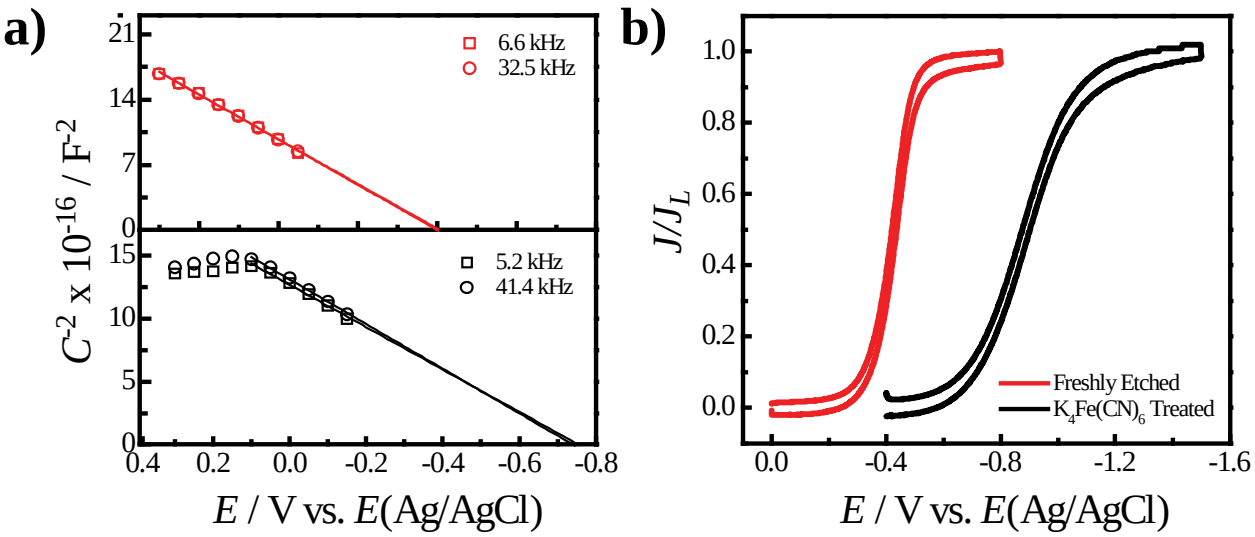

Figure 7.6 a) Mott-Schottky plots for freshly etched and oxidized 0.19 cm^2 n-Si electrodes in 0.1 M KCl. b) Voltammetric responses of freshly etched and treated non-degenerately doped n-Si SUMEs in 0.1 M KCl containing 2 mM $Ru(NH_3)_6^{3+}$. Scan rate: 10 mV s^{-1}, r = 5 µm.

Figure 7.6 tracks the effect of intentional oxidation of n-Si SUMEs on the voltammetric response for the reduction of $Ru(NH_3)_6^{3+}$. Following the process of Morrison,[255] a chemical surface oxide was grown quickly by soaking freshly etched n-Si SUMEs in aqueous solutions of $K_4Fe(CN)_6$ for 5 minutes. Figure 7.6a presents impedance measurements of the potential-dependence of the squared reciprocal capacitance of macroscale n-Si electrodes before and after treatment. A freshly etched n-Si electrode yielded linear data that indicated the conduction band edge was positioned at E = -0.407 ± 0.023 V in 0.1 M KCl(aq). After treatment in the ferrocyanide solution, the reciprocal capacitance measurements showed a plateau at positive potentials, consistent with the formation of a thick surface oxide.[256] The x-axis intercept implied a significant band edge shift to E = -0.74 V. Figure 7.6b shows the corresponding steady-state voltammetric responses for the reduction of $Ru(NH_3)_6^{3+}$ with n-Si SUMEs before and after treatment in the same manner. After surface oxidation, the steady-state voltammetric response of the n-Si SUME in

Figure 7.6b changed significantly and differently in comparison to Figure 7.5a. The voltammetric response shifted by more than 400 mV. More notably, the voltammetric shape broadened significantly.

The voltammetry data in Figure 7.6 for n-Si SUMEs illustrate the response characteristics when a thick surface oxide is present. The short 5 minutes immersion in aqueous ferrocyanide significantly distorted the steady-state voltammetry for the reduction of $Ru(NH_3)_6^{3+}$. In this case, the voltammetry shifted substantially, implying more than an order of magnitude attenuation of k_{et}. The clear change in γ further indicated that this oxide sufficiently impeded charge transfer. In total, the combined data of Figures 7.5 and 7.6 argue that the electrochemical response for the reduction of $Ru(NH_3)_6^{3+}$ is strongly and tractably sensitive to the evolving chemistry of a Si/water interface. Further, these data indicate that over short timescales (e.g. $t < 5$ minutes), the voltammetric responses of freshly etched n-Si SUMEs for the reduction of outer-sphere redox probes like $Ru(NH_3)_6^{3+}$ are sufficiently stable to permit analyses of charge-transfer kinetics, even in water.

7.4.3 Potential Drop Across the Semiconductor/Liquid Interface

In depletion, a common assumption is all of the applied potential, E, is dropped entirely across the space charge region of the semiconductor. In practice, the applied potential is actually distributed across both the semiconductor space charge region and the solid/liquid interface. For a semiconductor electrode, these two potential drops arise from the respective capacitances being linked in series. The corresponding fractions of the applied potential that are distributed across each can be determined numerically.[240, 244] The absolute value of the space charge capacitance for lightly doped Si in depletion and weak accumulation conditions can be determined from the following equation,[244]

$$C_{sc} = \left(\frac{q^2 N_d \varepsilon \varepsilon_0}{2k_B T}\right)^{1/2} \left(e^{\frac{q(\Delta E_{SC})}{k_B T}} - 1\right)\left(e^{\frac{q(\Delta E_{SC})}{k_B T}} - \frac{q(\Delta E_{SC})}{k_B T} - 1\right)^{-1/2} \quad (7.15)$$

where ΔE_{sc} is the built in potential within the space charge region and all the other terms are as defined previously. This expression simplifies to *eq 7.1* for just depletion conditions. Using a double layer capacitance of 5 μF/cm^2, the fraction of the applied potential dropped across the space charge region in Si for the systems reported here was determined and is shown Figure 7.7. These values were then used in the fitting analyses for the second column of fitted k_{et} and γ values in Table 7.2.

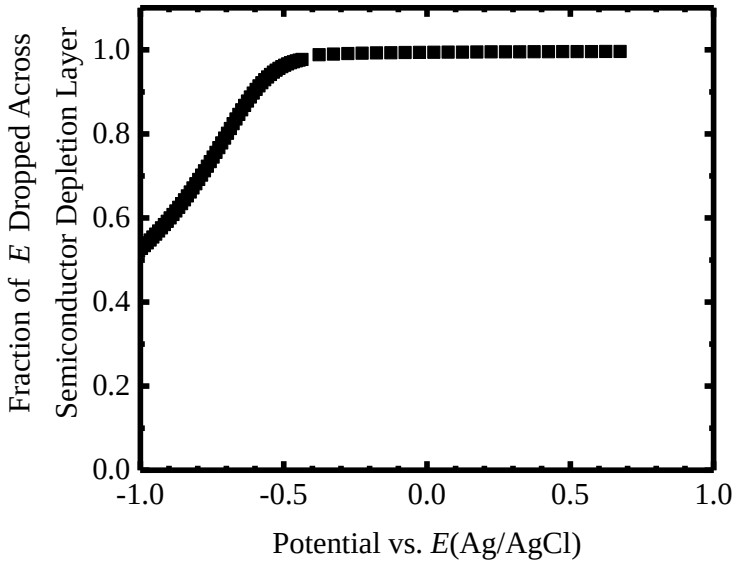

Figure 7.7 Fraction of potential dropped across space charge region in n-Si with N_d = 1.6 x 10^{15} cm^{-3} immersed in water with an ionic strength of 0.1 M as a function of the applied potential.

7.4.4 Kinetic Analyses with SUMEs

For an ideal interface between a non-degenerate semiconductor and liquid electrolyte with a dissolved outer-sphere redox species, the rate of charge transfer should have a first order dependence on both the acceptor concentration in solution and the surface concentration of electrons, *eq 7.16*.[23]

$$J(E) = qk_{et}n_s(E)[A] \qquad (7.16)$$

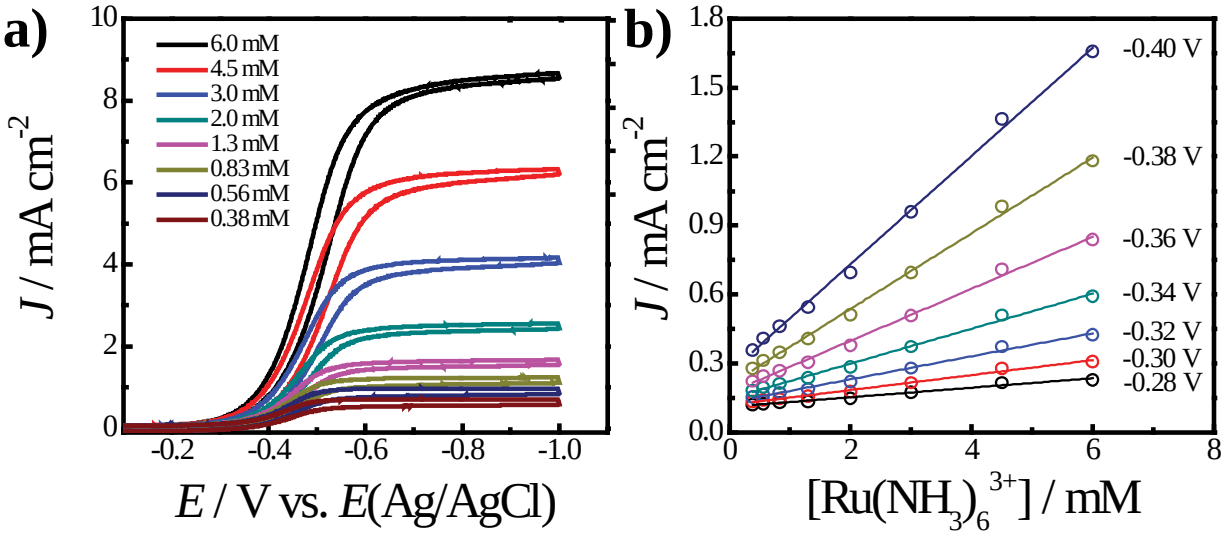

Figure 7.8 a) Concentration-dependent voltammetric response to $Ru(NH_3)_6^{3+}$ for a 5 µm n-Si SUME. The scan rate was 10 mV s^{-1}. b) Plot of the voltammetric wave position at E = -0.28, -0.30, -0.32, -0.34, -0.36, -0.38, and -0.40 V vs. E(Ag/AgCl) as a function of concentration.

The sensitivity of the voltammetric responses of n-Si SUMEs towards the reduction of $Ru(NH_3)_6^{3+}$ at different concentrations was determined. Figure 7.8 shows the steady-state voltammetric responses collected with a n-Si SUME with r = 5 µm over a range of concentrations of $Ru(NH_3)_6^{3+}$. At every concentration, a sigmoidal shape was obtained with the limiting currents

within 5% of the expected mass transport-limited current predicted by *eq 7.14*. A test of *eq 7.16* requires observation of a linear correlation between current and concentration at a fixed potential. Accordingly, Figure 7.8b shows a plot of the measured current densities as a function of the concentration of $Ru(NH_3)_6^{3+}$ at several potentials near the onset of the voltammetric response, i.e. far from the mass transport-limited regime. At every potential, the current-concentration slope was linear but with a distinct magnitude due to the potential dependence of $n_s(E)$, in agreement with *eq 7.16*.

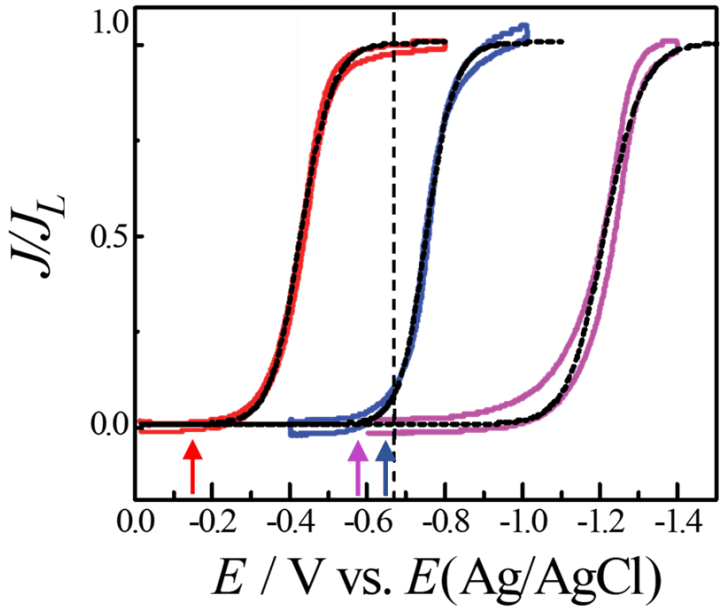

Figure 7.9 Normalized voltammetric responses of n-Si SUMEs with r = 5 μm in separate 0.1 M KCl aqueous solutions containing either (red) 2 mM $Ru(NH_3)_6^{3+}$, (blue) 2 mM MV^{2+}, or (purple) 2 mM $Co(sep)_3^{3+}$. The corresponding best fit line for each measurement is shown in black. The dashed line indicates the conduction band edge determined from separate impedance measurements. Color-coded arrows show the standard potential for each redox couple. Scan rate: 5 mV s^{-1}.

Based on these observations, the steady-state voltammetric responses at n-Si SUMEs for three outer-sphere redox couples were analyzed to determine their respective k_{et} values. Table 7.2

summarizes the relevant electrochemical properties for $Ru(NH_3)_6^{3+}$, methylviologen dication (MV^{2+}), and $Co(sep)_3^{3+}$. The color-coded arrows and the dashed vertical line on the x-axis of Figure 7.9 denote $E^{0'}$ for each redox species and E_{cb} in this electrolyte, respectively. The reorganization energies for heterogeneous reduction at n-Si listed in Table 7.2 were determined from published values of the reorganization energies for self-exchange reactions and the method described by Marcus (Section 7.2.3).[237] $Ru(NH_3)_6^{3+}$ and MV^{2+} have comparably small reorganization energies but differ substantially in $E^{0'}$. $Co(sep)_3^{3+}$ has an intermediate $E^{0'}$ value but a considerably larger reorganization energy. Figure 7.9 displays representative measurements of the steady-state voltammetric responses for n-Si SUMEs with r = 5 μm for these redox couples, with overlaid fits from *eqs 7.7-7.13* (Section 7.3) with only k_{et} and γ as adjustable parameters (Table *7.1*). Fits for the data for $Ru(NH_3)_6^{3+}$ and MV^{2+} were performed both without and with correction for the change in the fraction of the applied potential that was dropped within the semiconductor at potentials more negative than the flat-band potential (i.e. mild accumulation). That is, when the majority carrier density is large enough to make the space-charge capacitance comparable to or larger than the Helmholtz capacitance (Figure 7.7),[240, 244] a larger fraction of the applied potential is dropped at the semiconductor/liquid interface instead of within the semiconductor. For the 10^{15} cm^{-3} doping density used here, the effect is comparatively small. When this aspect was included, the fits yielded slightly lower k_{et} values (Table 7.2). Nevertheless, the fits for MV^{2+} and $Co(sep)_3^{3+}$ in Figure 7.9 yielded substantially smaller k_{et} values than for $Ru(NH_3)_6^{3+}$ (Table 7.2) regardless of the use of this correction.

Table 7.2 Relevant Parameters for and Results of Data Fitting of Steady-State Voltammetric Responses for the Reduction of Outer-Sphere Redox Couples at n-Si in 0.1 M KCl (aq)[a]

Redox Couple	$E^{\circ\prime}$ / V vs. E(Ag/AgCl)[b]	λ_{sc} / eV[c]	k_{et}[d] / cm^4 s^{-1}	γ[d]	k_{et}[e] / cm^4 s^{-1}	γ[e]
$Ru(NH_3)_6^{3+}$	-0.145	0.91	$(5.9 \pm 1.2) \times 10^{-16}$	1.5 ± 0.1	$(2.9 \pm 0.8) \times 10^{-16}$	1.5 ± 0.8
MV^{2+}	-0.625	0.64	$(1.1 \pm 0.3) \times 10^{-22}$	1.2 ± 0.1	$(1.8 \pm 0.3) \times 10^{-22}$	1.3 ± 0.1
$Co(sep)_3^{3+}$	-0.580	1.38	$(3.5 \pm 4.6) \times 10^{-23}$	1.8 ± 0.1	*NA*	*NA*

[a] Data obtained with n-Si SUMEs with $r = 5$ μm

[b] Values obtained from Reference [234]

[c] Calculation of reorganization energies described in the Supporting Information

[d] Results from fitting raw data

[e] Results from fitting data corrected for potential drop across the semiconductor/liquid interface as detailed in the Section 7.4.3

The utility of SUMEs for kinetic measurements are clear in the presented data. The pinhole SUME platform enabled reliable, rapid, and verifiable measurement of k_{et} for dissolved redox couples from simple steady-state voltammetry. Interpretable data was even obtained with dilute concentrations as low as 10^{-4} M. For macroscopic electrodes, mass-transfer resistance even at 10^{-3} M is often severe enough to distort the current-potential response, complicating measurements with sparingly soluble redox couples. With SUMEs and the data fitting approach presented here, the interplay between charge-transfer kinetics and mass transfer is sufficiently defined that quantitative measurements are possible at any concentration.

The magnitude of the value of k_{et} measured here (10^{-16} cm^4 s^{-1}) stands in contrast to the much smaller (10^{-22} cm^4 s^{-1}) rate constant value for the reduction of $Ru(NH_3)_6^{3+}$ at Si electrodes in water previously inferred from microwave photoconductivity measurements.[257] However, the measurements here were direct, reproducible, and conformed well to expectations from the Marcus-Gerischer framework for heterogeneous charge transfer,[232, 258]

$$k_{et} = k_{et,max}\, e^{\frac{-\left(\left(E_{cb}-E^{0'}\right)+\lambda_{sc}\right)^2}{4\lambda k_B T}} \qquad (7.17)$$

where $k_{et,max,}$ is the rate constant at optimal exoergicity. The value of $k_{et,max}$ is believed to have a value of 10^{-16} - 10^{-17} $cm^4\ s^{-1}$.[246] Given the reorganization energy, λ_{sc}, for $Ru(NH_3)_6^{3+}$ in water (Table 1) and the value of E_{cb} relative to $E^{0'}$, the measured rate constant for electron transfer from the band edge of freshly etched Si to freely dissolved $Ru(NH_3)_6^{3+}$ in water is expected to be very close to $k_{et,max,}$ consistent with what was measured here. This point merits special attention since it counters a long-standing conventional wisdom in semiconductor electrochemistry. Specifically, the instability of Si in water has long been assumed to preclude the possibility of tractable and quantitative voltammetric measurement of charge-transfer kinetics. This measurement, in conjunction with the aforementioned meta-stability of the Si/water interface (*vide supra*), clearly establish that voltammetry with n-Si electrodes yields results in accord with the dominant microscopic theory of charge transfer.

Measurements of k_{et} for MV^{2+} and $Co(sep)_3^{3+}$ are also generally in agreement with *eq 7.17* but their interpretation is more nuanced. Both redox couples elicited voltammetric responses that were shifted to even more negative potentials than the response for $Ru(NH_3)_6^{3+}$. This observation implies substantially smaller values of k_{et} for both these redox couples, in accord with the predictions from *eq 7.17* since both the reduction of MV^{2+} and $Co(sep)_3^{3+}$ occur with a much smaller driving force than their respective λ_{sc} values (Table 7.2). Still, the specific values of each respective rate constant are convoluted because of two factors. First, both have some degree of chemical 'interference'. The potential window for the voltammetric response for the $MV^{2+/+}$

process was limited by the onset of the current response for the $MV^{+/0}$ reduction. Separately, the current response for the $Co(sep)_3^{3+/2+}$ redox couple was shifted sufficiently negative that concurrent cathodic hydrogenation of Si likely occurred to some extent (i.e. H_2 diffuses into Si surfaces at extreme negative potentials in water).[259, 260] We separately saw evidence of this when the n-Si SUMEs were biased more negative than -1.0 V. This process likely contributed to the notable hysteresis in the voltammetric response for the $Co(sep)_3^{3+/2+}$ couple. Second, some or all of the voltammetric responses for the reduction of MV^{2+} and $Co(sep)_3^{3+}$ occurred at potentials negative of the conduction band edge, i.e. the n-Si SUMEs were operating under progressively more accumulated conditions. In this regime, the potential-dependence of n_s is more complex since the Boltzmann approximation is less accurate and the Fermi-Dirac function must be used. That is, the applied potential is distributed across both the space charge layer of the semiconductor and the double layer in solution, imparting some potential dependence to E_{cb}. The presented analyses apply rigorously to non-degenerately doped semiconductors operating under depletion and mild accumulation conditions, but it is less clear how the specific shapes of the steady-state voltammetric responses should appear when the electrode becomes strongly accumulated. Accordingly, more precise estimates of the values of k_{et} for the reduction $Co(sep)_3^{3+}$ specifically require further theoretical development.

7.5 Practical Attributes of Recessed SUMEs

The collective data provided in this chapter speak to three points. First, SUMEs based on the shallow recessed disk motif show tractable steady-state voltammetric response characteristics.

Second, such SUMEs are useful for assessing the interfacial character of semiconductor/solution contacts. Third, quantitative kinetic measurements with these SUMEs are readily possible.

Recessed SUMEs comprised of an intentional pinhole with defined dimensions in a thin dielectric coating on a semiconductor substrate offers several tangible advantages for study. First, such SUMEs are naturally compatible with the use of semiconductor single-crystalline wafers/epifilms where the relevant material properties (e.g. doping levels/profiles, charge-carrier mobilities, crystallinity) are fully known. Accordingly, it was straightforward to compare and understand the response characteristics of degenerately and non-degenerately doped SUMEs in Figure 7.4. In contrast, such studies are not feasible with the more 'traditional' design of an ultramicroelectrode where a thin (semiconductor) filament is encased in an insulating shroud.[214, 241] This motif has been previously attempted with ZnO nanorod SUMEs with limited success.[261] The difficulty lies in knowing (and controlling) the semiconductor material properties precisely since they strongly influence heterogeneous charge transfer.[59, 230] Further, since the radius of thin semiconductor filament can strongly affect the shape of the depletion layer within the semiconductor in complex manners, a detailed understanding of current flow in a semiconductor filament ultramicroelectrode is substantially complicated.[262, 263]

Second, the steady-state current-potential responses of the SUME platforms described here are readily interpretable. As detailed in Figure 7.3, the current-potential responses are dependent on k_{et}, r, $E^{0'}$, and E_{cb} based on the defined interplay between kinetic and mass transport-limited current fluxes at small disk electrodes. Interpretation of current-potential data is not always as easy or even feasible for other electrochemical strategies that probe current flow at small areas. For example, scanning electrochemical microscopy (SECM)[264, 265] has been used to assess current flow at semiconductor/liquid contacts.[247] However, understanding the feedback current in SECM of

semiconductors is made difficult by contributions from the lateral surface conductivity (i.e. along the plane of the semiconductor/electrolyte interface). That is, unlike in a metal, the charge conductivity of a semiconductor can be very different along the surface plane as compared to normal to the surface plane.[59] If sufficiently high, surface conductivity could cause the feedback current in SECM to be sensitive to redox processes (e.g. corrosion)[266, 267] occurring away from the area probed by the tip. Since lateral surface conductivity of a semiconductor is strongly sensitive to the extent of depletion/inversion/accumulation in the semiconductor,[268, 269] deciphering the SECM feedback response at a semiconductor is not straightforward.[270]

Third, the SUME platforms shown here are compatible with use in any solvent/electrolyte system. Although the studies here were limited to aqueous electrolytes, nothing prohibits the use of these SUMEs in non-aqueous electrolytes, where richer tests of charge-transfer theory are possible.[37, 271, 272] In fact, the lower surface tension of non-aqueous solvents may facilitate better wetting into the recessed disk cavity.[236] This same aspect complicates the use of scanning electrochemical cell microscopy (SECCM)[273] for making small area semiconductor/electrolyte contacts. In that method, a small junction is made by wetting a substrate with a microscopic hanging liquid drop that has counter and reference electrodes, as first described by Koval and co-workers[274] and more recently advanced by Unwin and co-workers.[273] The difficulty in controlling the stability, wetting, and spreading of non-aqueous liquids is well-documented[275] and a major impediment to its use for studying the details of semiconductor electrochemistry.

Still, certain aspects of the pinhole SUME platform merit mention. The specific composition and design of the dielectric layer should be further developed. If other 'low *k*' dielectric films are employed, the background capacitance might be further be minimized. Fortunately, the pinhole SUME platform is compatible with any substrate, insulator (e.g. SiN_x,

SiO_xN_y, SiO_2, Al_2O_3, PDMS, etc.), and deposition method (e.g. spin-coating, chemical vapor deposition, atomic layer deposition) provided the dielectric can be properly patterned. The dielectric layer used here resulted in a noticeable level of background capacitance, particularly for the smallest *r* value. Although not disruptive in this work, it is conceivable such a background capacitance could obfuscate the use of SUMEs with smaller *r* values. The issue is that thicker dielectric layers will decrease the background capacitance but necessarily increase the recession depth of the SUME. Deeper recession depths complicate mass transport since inside the recession mass transport will be linear rather than radial.[215, 216, 224] The approach followed in the previous chapter can be used as a guide to determine the critical threshold L/r ratio when the normalized steady-state voltammetric responses of the recessed UMEs appreciably deviate from the data fitting approach of Bond, Oldham, and Zoski. Any over-estimation of the k_{et} values reported here due to the recession is likely minimal. For a solution of 2 mM $Ru(NH_3)_6^{3+}$, the recessed SUMEs with r = 5 μm have a current density of 3.83 mA cm^{-2}, compared to the expected 3.98 mA cm^{-2} for an equivalent inlaid disk case.

Also, while using the photolithographic fabrication approach, care was needed to avoid compromising the exposed semiconductor electrode surface. Specifically, a previous work similarly attempted to make arrays of ultramicroelectrodes on Si through a combination of photolithographic patterning and dry etching.[276] However, they reported behavior more consistent with metal electrodes rather than the unique characteristics of a non-degenerate semiconductor electrode detailed here. Issues in their fabrication, including reliance on destructive dry etches, likely destroyed their semiconductor surface. In this work, the semiconductor surfaces were protected during the low-selectivity reactive-ion etching (RIE) process by leaving a thin insulting layer on top of the SUME active area and wet-etching it off before the first measurement.

Purposely leaving this thin layer prevented unintentional dry etching of the SUME surface and allowed wet-etching to occur without appreciable undercutting. The tractability of the measurements made with the SUME platforms suggests these preventative steps preserved the integrity of the surface in two ways. First, the current for the reduction of outer-sphere redox probes was first-order with concentration. Second, the ideality factors obtained with the aqueous contacts are equivalent or lower than ideality factors measured with macroscopic electrodes under similar conditions.[277]

7.6 Conclusion

This chapter describes a comprehensive overview of the operation of non-degenerately doped SUMEs functioning under depletion conditions and a basis for evaluating their response characteristics. Akin to metal ultramicroelectrodes, SUMEs have the familiar steady-state current-potential profiles but their interpretation requires a kinetic framework different than the Butler-Volmer formalism. With this proviso and unlike the current responses from macroscopic semiconductor electrodes, the electrochemical behaviors of SUMEs towards putative outer-sphere redox couples in solution are understandable. The utility of these platforms for enabling voltammetry to inform on the static and dynamic features of semiconductor/liquid junctions has been demonstrated. Continued work in the following areas are necessary to further advance the analytical utility of pinhole SUMEs for systems based on semiconductor/liquid interfaces. First, fabrication of SUMEs with values of r smaller than the average separation distance between surface traps/defects could increase the probability of realizing semiconductor electrodes with $\gamma \rightarrow 1$. Second, global fitting of SUME steady-state voltammetric responses for multiple outer-

sphere redox couples should be explored to determine whether semiconductor band edge energetics can be identified without requiring separate impedance-based measurements. Third, further refinement of the modeling for fitting data under strong accumulation and strong inversion conditions is warranted. Doing so would further enable more comprehensive tests of Marcus theory at semiconductor/solution interfaces. Additionally, the present work only describes the current-potential responses of SUMEs in the dark. Under illumination, the voltammetric characteristics of pinhole SUMEs should also prove useful if their respective sensitivities towards the method of photogeneration, the interfacial charge-transfer kinetics, and the transport of charges can be readily distinguished. Such data would be germane to the field of photoelectrochemistry generally and potentially the operation of discrete semiconductor photocatalysts specifically.

Chapter 8

Summary and Future Directions

8.1 Summary of Present Work

This thesis investigates the fundamental and practical perspectives of electrochemistry, a branch of chemistry that has been studied since the late-eighteenth century, and demonstrates that electrochemistry can enable novel, simplistic, and cost-effective routes for realizing high-quality photonic devices in the large scale. The first section (Chapters 2 and 3) of this thesis focusses on ec-LLS. While traditional semiconductor growth techniques provide high-purity crystalline materials, they are all energy-intensive. The ec-LLS technique performs crystalline semiconductor growth in an aqueous electrolyte at ambient conditions and challenges pre-conceived notions held on the requirements for enabling epitaxial semiconductor crystal growth. Previous studies have demonstrated ec-LLS growth for a variety of group IV and III-V materials. However, in order to further develop this process, and to better understand its advantages and limitations, it is imperative to take a step back and analyze the individual factors controlling the ec-LLS growth process. In chapter 2, the effect of choice of liquid metal on the crystalline and electrical nature of ec-LLS grown Ge crystals was analyzed. Further insights were obtained on the solvent-trapping growth mode of ec-LLS using a combination of electrical characterization techniques and atom probe tomography. Although only hyperdoped Ge crystals were obtained using the growth parameters

employed, the results evidently indicate a correlation between the solvent system utilized and subsequent metal incorporation during ec-LLS crystal growth.

Chapter 3 provides a systematic study on other critical factors affecting the ec-LLS process. It was shown that controlling the flux of the precursor species to the liquid metal electrode is an effective technique to reduce the ec-LLS growth rate and possibly drive the growth closer to equilibrium conditions. However, the data presented here imply a complicated electron transfer process between the electrode and freely dissolved precursor species. Reducing the concentration of the precursor species can further complicate this process giving rise to unpredictable anomalies. Alternatively, the concept of pulsed ec-LLS was introduced in this thesis. The motivation for pursuing this approach is to drive the ec-LLS growth under near-equilibrium conditions by electrochemically 'titrating' discrete amounts of Ge^0 into the liquid metal droplet. Further work and characterization are still needed to optimize this approach. Lastly, high-efficiency broad-band optical absorbers based on ec-LLS grown Ge nanowires were realized at ambient conditions on a variety of support substrates.

The second section (Chapters 4 and 5) of this thesis explores the prospect of using electrochemical methods for fabricating structural color filters. Chapter 4 demonstrates electrodeposition of multi-layered metal/dielectric structures to realize ambient-condition processing of structural colors on substrates of arbitrary shape, size, and roughness. Reducing manufacturing costs and increasing the ease of scalability have made the implementation of structural colors more practical for aesthetic and optical coating applications. In chapter 5, electrochemically tunable structural color filters exhibiting dynamic reconfigurability between multiple colored states while operating under low-power conditions were demonstrated for aesthetic and passive display applications.

The last section (Chapters 6 and 7) of this thesis introduces SUMEs as new platforms for accurately investigating charge transfer processes at semiconductor/liquid interfaces. Methods were reported for interpreting their electrochemical response characteristics in the absence of illumination. Radial diffusion was reconciled with the diode equation to describe the full voltammetric response, allowing direct determination of heterogeneous charge-transfer rate constants and surface quality. The voltammetric responses of n-type Si SUMEs were assessed and showed prototypical UME characteristics with obtainable current densities higher than those of conventional macroscopic electrodes. The SUME voltammetry proved highly sensitive to both native and intentionally grown oxides, highlighting their ability to precisely track dynamic surface conditions reliably through electrochemical measurement. Subsequently, electron transfer from the conduction band of n-Si SUMEs to aqueous $Ru(NH_3)_6^{3+}$ was determined to occur near optimal exoergicity. In total, this work validates the SUME platform as a new tool to study fundamental charge-transfer properties at semiconductor/liquid junctions.

8.2 Ongoing and Future Work

Despite the progress presented in this cumulative work, there are still several avenues available for further development which are summarized below.

8.2.1 All-Solid-State Tunable Structural Color Filters

The ability to cover the CIE chromaticity chart using an individual structural color device is highly desired for display and sensing applications. In this thesis, an approach to generate dynamically reconfigurable and tunable structural color devices is proposed and demonstrated by making use of electrochromic materials. The color change was induced by exposing the device to

a liquid electrolyte containing Li^+ or Zn^{2+} ions in the presence of an applied potential or electric field. In order to take this proof of concept demonstration closer towards real-world applications, this work needs to be extended to achieve all-solid-state tunable structural color devices. One obvious and plausible approach is to replace the liquid electrolyte with a high ionic conductivity solid-electrolyte. Alternatively, this section proposes two other approaches to achieve all-solid-state tunable colors without compromising on any of the advantages demonstrated in Chapter 5. All these approaches are based on the same principle: electrochemically altering the optical constants of the cavity layer in the structural color devices, which in turn modifies the absorption peak position resulting in a different colored appearance.

In-depth hydrogen profiling has revealed a significant uptake of hydrogen in evaporated SiO_2 films.[201, 202] Evaporated insulator films contain pin-holes and channels that allow atoms or molecules from the ambient environment to diffuse into or through these films. SiO_2 films have already been demonstrated to be an effective solid-electrolyte in all-solid-state electrochromic devices.[187] The first proposed approach in this section is based on a F-P cavity-based MDM structure, wherein the cavity layer is composed of three sequential dielectric films (Figure 8.1). Hydrogen can be introduced into the structure by exposing the evaporated SiO_2 to a controlled humidity environment during the fabrication process. The two metal layers in the MDM structure also function as the anode and cathode of this electrochromic device. Cathodic electrochromic materials (e.g. WO_3) become absorptive (partially colored) as they are reduced, while anodic electrochromic materials (e.g. $Ir(OH)_2$) become absorptive as they are oxidized. Thus, when a negative bias is applied to the bottom metal layer of the proposed structure in Figure 8.1, the cathodic electrochromic layer can get reduced by consuming H^+ ions that are driven out from the oxidized anodic electrochromic layer. As a result, both electrochromic layers become more

absorptive and can significantly alter the optical constants of the effective cavity layer, eventually tuning the colored appearance of this device.

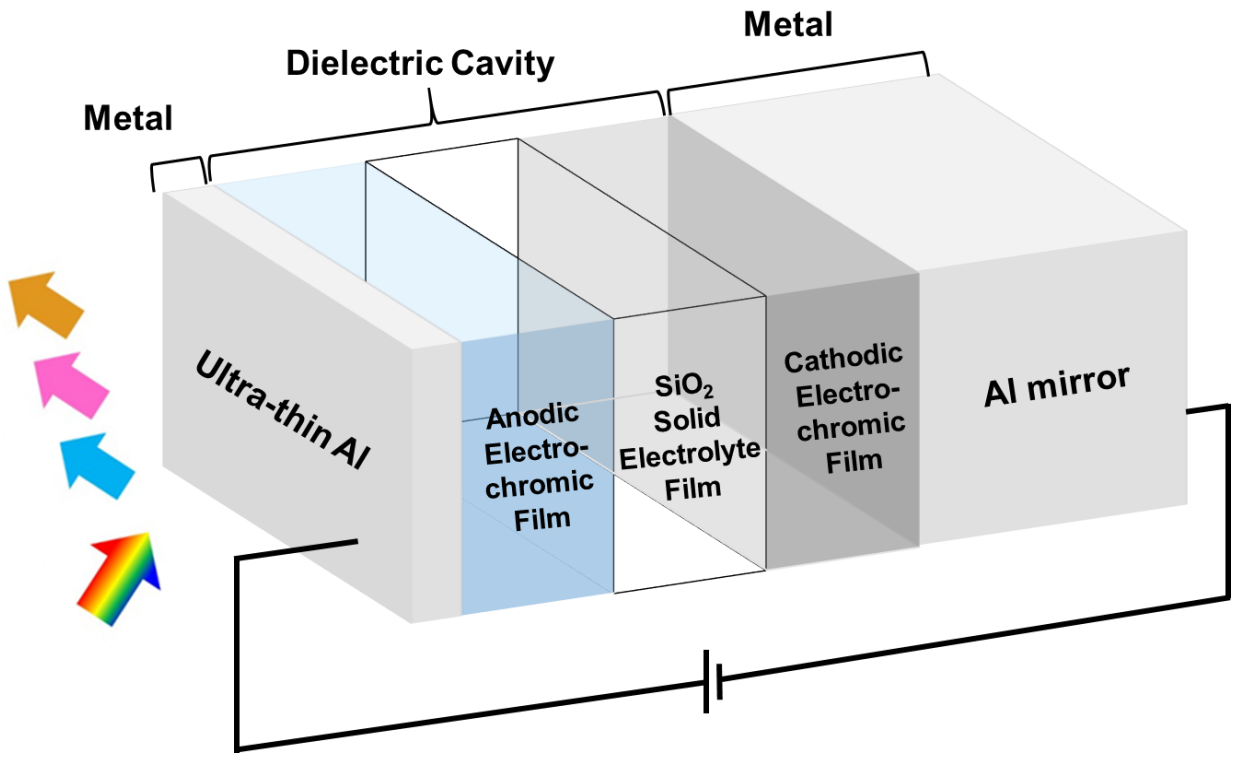

Figure 8.1 Schematic representation of the proposed tunable structural color device with an embedded SiO_2 solid electrolyte layer.

Figure 8.2 shows the schematic of the second tunable color approach proposed in this section. This structure consists of a simplistic design and can potentially be achieved with just three MDM layers. 2 nm Ti is introduced in this structure to enhance the adhesion between the Pt and the dielectric WO_3 layer. Unlike the previous approach where an external potential is applied to drive the electrochemical change, this structure utilizes the catalytic property of Pt to drive H^+

ions into or out of the electrochromic layer.[171, 278] As shown in Figure 8.2, when the device is exposed to a stream of H_2 (g), an electrochromic change can be induced through the following reactions:

$$H_2\,(g) \rightarrow 2H^+ + 2e^- \qquad (8.1)$$

$$WO_3 + xH^+ + xe^- \rightarrow H_xWO_3 \qquad (8.2)$$

Similarly, by flushing the device with O_2 (g), the original color can be restored through the following reaction:

$$Li_xWO_3 + O_2\,(g) \rightarrow WO_3 + H_2O\,(g) \qquad (8.3)$$

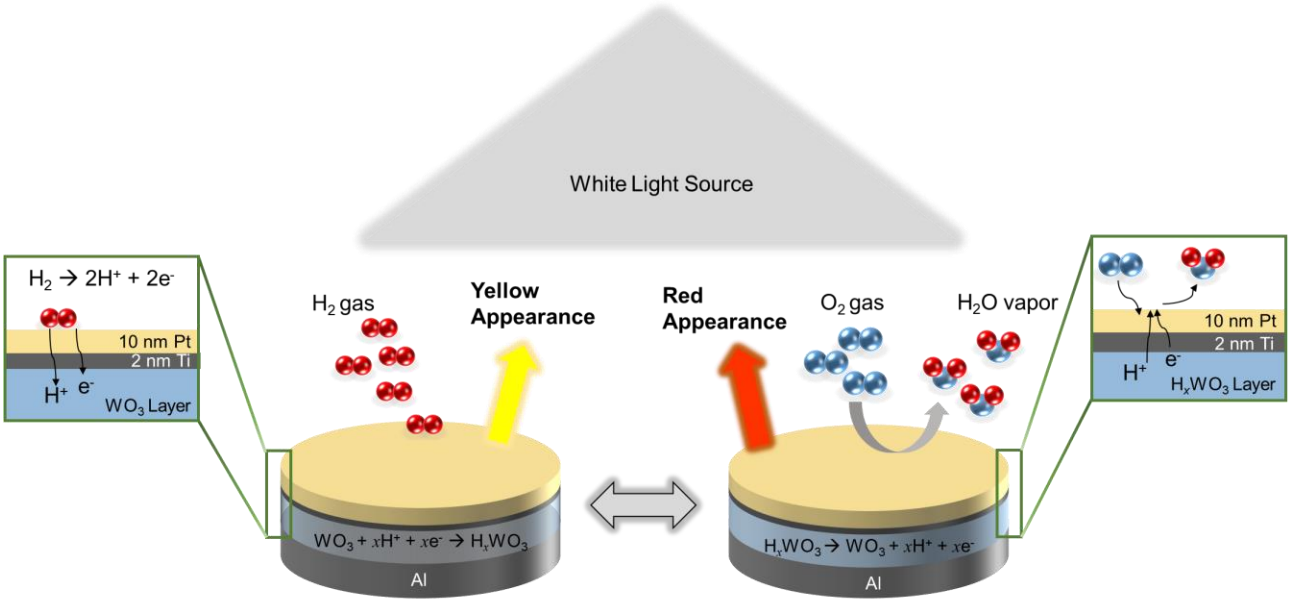

Figure 8.2 Schematic of proposed all-solid-state tunable structural color device making use of the catalytic property of Pt.

8.2.2 Harnessing the Kinetic and Diffusion Limited Regimes during Electrodeposition for Multi-Color Structural Color Deposition on Same Substrate

In the structural color design, different colors of high brightness can be achieved by simply tuning the thickness of the dielectric cavity layer. Using this concept, previous reports have demonstrated multi-colored structural color patterns on different regions of the same substrate by making use of multiple photolithography and deposition steps. These additional steps significantly increase the cost and complexity of this approach. This section proposes using a single step electrodeposition process to achieve films of different thicknesses in different regions of the substrate in a controlled and predicted manner. The cathodic current during electrodeposition, which defines the deposition rate, is proportional to the reaction rate (k) and the flux of precursor species to the reaction surface. It is possible to greatly vary the flux of the precursor species by controlling their diffusion profile. In Figure 8.3, it is proposed that by patterning pixels within the letter 'M', the radial diffusion profiles in these regions should result in faster deposition rates compared to the regions with a planar diffusion profile (letter 'U'). This way, different thicknesses of the dielectric cavity layer (e.g. 40 nm and 65 nm in this hypothetical case) resulting in different colors can be achieved in a single step in a well-defined manner. This approach is not limited to just two colors; it can be extended further to achieve the entire RGB spectrum on a single substrate by just controlling the pixel diameter and pitch in the respective regions. The large dimensions (micron scale) of the pixels in Figure 8.3 ensure they do not result in any unwanted interference effects.

Figure 8.3 Cartoon representation of multi-colored structural color films on the same substrate. Here, different thicknesses of the dielectric cavity layer (Cu_2O) resulting in different colors can be achieved using a single deposition step by controlling the diffusion profile (between liner and radial profiles) of the precursor species.

Similarly, further work needs to be done to exploit reaction kinetics during electrodeposition as a tool to achieve films of different thicknesses in different spatial regions during a single electrodeposition step. The SUME platforms introduced in this thesis can potentially prove to be useful in validating and developing this approach.

8.2.3 Ambient Condition Processing of Additive Colors

This thesis presented subtractive CMY colors using the solution-processed approach. Efforts are ongoing towards finding materials and methods to produce additive RGB colors. One approach is to use the standard MDM structure, but by selecting an absorptive material (e.g. Ni) as the top metal layer. Further work is required to ensure the electrodeposition of the top absorptive layer satisfies several constraints: uniformity over large areas while maintaining minimal thickness (i.e. < 20 nm), low surface roughness to avoid deleterious light scattering effects, and not compromising the physical and chemical integrity of the underlying dielectric film.

Bibliography

1. Cho, A. Y.; Arthur, J. R., Molecular beam epitaxy. *Progress in Solid State Chemistry* **1975,** *10*, 157-191.
2. Dupuis, R. D., Metalorganic Chemical Vapor Deposition of III-V Semiconductors. *Science* **1984,** *226* (4675), 623-629.
3. Kuphal, E., Liquid phase epitaxy. *Applied Physics A* **1991,** *52* (6), 380-409.
4. Liu, Y.; Deal, M. D.; Plummer, J. D., High-quality single-crystal Ge on insulator by liquid-phase epitaxy on Si substrates. *Applied Physics Letters* **2004,** *84* (14), 2563-2565.
5. Wagner, R. S.; Ellis, W. C., Vapor-Liquid-Solid Mechanism of Single Crystal Growth. *Applied Physics Letters* **1964,** *4* (5), 89-90.
6. Trentler, T. J.; Hickman, K. M.; Goel, S. C.; Viano, A. M.; Gibbons, P. C.; Buhro, W. E., Solution-Liquid-Solid Growth of Crystalline III-V Semiconductors: An Analogy to Vapor-Liquid-Solid Growth. *Science* **1995,** *270* (5243), 1791-1794.
7. Wang, F.; Dong, A.; Sun, J.; Tang, R.; Yu, H.; Buhro, W. E., Solution−Liquid−Solid Growth of Semiconductor Nanowires. *Inorg. Chem.* **2006,** *45* (19), 7511-7521.
8. Fahrenkrug, E.; Maldonado, S., Electrochemical Liquid–Liquid–Solid (ec-LLS) Crystal Growth: A Low-Temperature Strategy for Covalent Semiconductor Crystal Growth. *Accounts of Chemical Research* **2015,** *48* (7), 1881-1890.
9. Gu, J.; Fahrenkrug, E.; Maldonado, S., Direct Electrodeposition of Crystalline Silicon at Low Temperatures. *Journal of the American Chemical Society* **2013,** *135* (5), 1684-1687.
10. Fahrenkrug, E.; Gu, J.; Maldonado, S., Electrodeposition of Crystalline GaAs on Liquid Gallium Electrodes in Aqueous Electrolytes. *Journal of the American Chemical Society* **2013,** *135* (1), 330-339.
11. Fahrenkrug, E.; Gu, J.; Jeon, S.; Veneman, P. A.; Goldman, R. S.; Maldonado, S., Room-Temperature Epitaxial Electrodeposition of Single-Crystalline Germanium Nanowires at the Wafer Scale from an Aqueous Solution. *Nano Lett.* **2014,** *14* (2), 847-852.
12. Ma, L.; Gu, J.; Fahrenkrug, E.; Maldonado, S., Electrochemical Liquid-Liquid-Solid Deposition of Crystalline Ge Nanowires as a Function of Ga Nanodroplet Size. *J. Electrochem. Soc.* **2014,** *161* (6), D3044-D3050.

13. Kumar, K.; Duan, H.; Hegde, R. S.; Koh, S. C. W.; Wei, J. N.; Yang, J. K. W., Printing colour at the optical diffraction limit. *Nat. Nanotechnol.* **2012,** *7* (9), 557-561.
14. Xu, T.; Wu, Y.-K.; Luo, X.; Guo, L. J., Plasmonic nanoresonators for high-resolution colour filtering and spectral imaging. *Nat. Commun.* **2010,** *1*, 59.
15. Davis, M. S.; Zhu, W.; Xu, T.; Lee, J. K.; Lezec, H. J.; Agrawal, A., Aperiodic nanoplasmonic devices for directional colour filtering and sensing. *Nat. Commun.* **2017,** *8* (1), 1347.

16. Uddin, M. J.; Magnusson, R., Highly efficient color filter array using resonant Si3N4 gratings. *Opt. Express* **2013,** *21* (10), 12495-12506.
17. Kaplan, A. F.; Xu, T.; Guo, L. J., High efficiency resonance-based spectrum filters with tunable transmission bandwidth fabricated using nanoimprint lithography. *Appl. Phys. Lett.* **2011,** *99* (14), 143111.
18. Banerjee, D.; Zhang, M., Quarter-wave design criteria for omnidirectional structural colors. *J. Mod. Opt.* **2010,** *57* (13), 1180-1188.
19. Li, Z.; Butun, S.; Aydin, K., Large-Area, Lithography-Free Super Absorbers and Color Filters at Visible Frequencies Using Ultrathin Metallic Films. *ACS Photonics* **2015,** *2* (2), 183-188.
20. Yang, C.; Shen, W.; Zhang, Y.; Li, K.; Fang, X.; Zhang, X.; Liu, X., Compact Multilayer Film Structure for Angle Insensitive Color Filtering. *Sci. Rep.* **2015,** *5*, 9285.
21. Park, C.-S.; Shrestha, V. R.; Lee, S.-S.; Choi, D.-Y., Trans-Reflective Color Filters Based on a Phase Compensated Etalon Enabling Adjustable Color Saturation. *Scientific Reports* **2016,** *6*, 25496.
22. https://www.youtube.com/watch?v=nYu1ruSakRg&t=128s.
23. Gerischer, H., The Impact of Semiconductors on the Concepts of Electrochemistry. *Electrochim. Acta* **1990,** *35* (11-12), 1677-1699.
24. Meek, R. L.; Schumaker, N. E., Anodic Dissolution and Selective Etching of Gallium Phosphide. *J. Electrochem. Soc.* **1972,** *119* (9), 1148-1152.
25. Youtsey, C.; Adesida, I.; Bulman, G., Highly anisotropic photoenhanced wet etching of n-type GaN. *Appl. Phys. Lett.* **1997,** *71* (15), 2151-2153.
26. Minks, B. P.; Vanmaekelbergh, D.; Kelly, J. J., Current-Doubling, Chemical Etching and the Mechanism of 2-Electron Reduction Reactions at GaAs .2. A Unified Model. *J. Electroanal. Chem.* **1989,** *273* (1-2), 133-145.
27. Rothberg, J. M.; Hinz, W.; Rearick, T. M.; Schultz, J.; Mileski, W.; Davey, M.; Leamon, J. H.; Johnson, K.; Milgrew, M. J.; Edwards, M.; Hoon, J.; Simons, J. F.; Marran, D.; Myers, J. W.; Davidson, J. F.; Branting, A.; Nobile, J. R.; Puc, B. P.; Light, D.; Clark, T. A.; Huber, M.; Branciforte, J. T.; Stoner, I. B.; Cawley, S. E.; Lyons, M.; Fu, Y. T.; Homer, N.; Sedova, M.; Miao, X.; Reed, B.; Sabina, J.; Feierstein, E.; Schorn, M.; Alanjary, M.; Dimalanta, E.; Dressman, D.; Kasinskas, R.; Sokolsky, T.; Fidanza, J. A.; Namsaraev, E.; McKernan, K. J.; Williams, A.; Roth, G. T.; Bustillo, J., An integrated semiconductor device enabling non-optical genome sequencing. *Nature* **2011,** *475* (7356), 348-352.
28. Steinhoff, G.; Hermann, M.; Schaff, W. J.; Eastman, L. F.; Stutzmann, M.; Eickhoff, M., pH response of GaN surfaces and its application for pH-sensitive field-effect transistors. *Appl. Phys. Lett.* **2003,** *83* (1), 177-179.
29. Fujishima, A.; Honda, K., Electrochemical Photolysis of Water at a Semiconductor Electrode. *Nature* **1972,** *238*, 37-38.
30. Gratzel, M., Photoelectrochemical cells. *Nature* **2001,** *414* (6861), 338-344.
31. Smith, W. A.; Sharp, I. D.; Strandwitz, N. C.; Bisquert, J., Interfacial band-edge energetics for solar fuels production. *Energy & Environmental Science* **2015,** *8*, 2851-2862.
32. Kohl, P. A.; Bard, A. J., Semiconductor Electrodes: XVII. Electrochemical Behavior of n- and p-type InP Electrodes in Acetonitrile Solutions. *J. Electrochem. Soc.* **1979,** *126* (4), 598-603.
33. Kohl, P. A.; Bard, A. J., Semiconductor Electrodes. 13. Characterization and Behavior of n-type ZnO, CdS, and GaP Electrodes in Acetonitrile Solutions. *J. Am. Chem. Soc.* **1977,** *99* (23), 7531-7539.

34. Frank, S. N.; Bard, A. J., Semiconductor Electrodes II. Electrochemistry at n-type TiO_2 Electrodes in Acetonitrile Solutions. *J. Am. Chem. Soc.* **1975,** *97* (26), 7428-7433.
35. Nagasubramanian, G.; Wheeler, B. L.; Fan, F. F.; Bard, A. J., Semiconductor Electrodes: XLII. Evidence for Fermi Level Pinning from Shifts in the Flatband Potential of p-type Silicon in Acetonitrile Solutions with Different Redox Couples. *J. Electrochem. Soc. 129* (8), 1742-1745.
36. Chazalviel, J. N.; Truong, T. B., A Quantitative Study of Fermi Level Pinning at a Semiconductor-Electrolyte Interface. *J. Electroanal. Chem.* **1980,** *114*, 299-303.
37. Koval, C. A.; Torres, R., Detection of Hot Electrons at a p-InP/Pt Rotating Ring/Disk Photoelectrode. *J. Am. Chem. Soc.* **1993,** *115*, 8368-8375.
38. Koval, C. A.; Austermann, R. L.; Turner, J. A.; Parkinson, B. A., The Effects of Surface Energetics and Surface Oxide Layers on the Cyclic Voltammetry of Metallocenes at Nonilluminated p - InP Electrodes. *J. Electrochem. Soc.* **1985,** *132* (3), 613-623.
39. Koval, C. A.; Austermann, R. L., The Effects of Surface Energetics on the Cyclic Voltammetry of Metallocenes at Nonilluminated n-InP Electrodes. *J. Electrochem. Soc.* **1985,** *132* (11), 2656-2662.
40. DeMuth, J.; Fahrenkrug, E.; Maldonado, S., Controlling Nucleation and Crystal Growth of Ge in a Liquid Metal Solvent. *Cryst. Growth Des.* **2016,** *16* (12), 7130-7138.
41. Fahrenkrug, E.; Biehl, J.; Maldonado, S., Electrochemical Liquid–Liquid–Solid Crystal Growth of Germanium Microwires on Hard and Soft Conductive Substrates at Low Temperature in Aqueous Solution. *Chemistry of Materials* **2015,** *27* (9), 3389-3396.
42. Anderson, T. J.; Ansara, I., The Ga-In (Gallium-Indium) System. *J. Phase Equilibria* **1991,** *12* (1), 64-72.
43. Trumbore, F. A., Solid solubilities of impurity elements in germanium and silicon. *Bell Syst. Tech. J.* **1960,** *39* (1), 205-233.
44. Ogawa, H.; Guo, Q.; Ohta, K., Low temperature liquid phase epitaxy of silicon from gallium solution. *J. Cryst. Growth* **1995,** *155* (3), 193-197.
45. Martin, H.; Alois, L.; Clemens, Z.; Tomasz, W.; Peter, P.; Emmerich, B., Ultra-fast vapour–liquid–solid synthesis of Si nanowires using ion-beam implanted gallium as catalyst. *Nanotechnology* **2011,** *22* (39), 395601.
46. Seifner, M. S.; Sistani, M.; Porrati, F.; Di Prima, G.; Pertl, P.; Huth, M.; Lugstein, A.; Barth, S., Direct Synthesis of Hyperdoped Germanium Nanowires. *ACS Nano* **2018,** *12* (2), 1236-1241.
47. von den Driesch, N.; Stange, D.; Wirths, S.; Mussler, G.; Holländer, B.; Ikonic, Z.; Hartmann, J. M.; Stoica, T.; Mantl, S.; Grützmacher, D.; Buca, D., Direct Bandgap Group IV Epitaxy on Si for Laser Applications. *Chemistry of Materials* **2015,** *27* (13), 4693-4702.
48. Keck, P. H.; Broder, J., The Solubility of Silicon and Germanium in Gallium and Indium. *Physical Review* **1953,** *90* (4), 521-522.
49. Fahrenkrug, E.; Biehl, J.; Maldonado, S., Electrochemical Liquid–Liquid–Solid Crystal Growth of Germanium Microwires on Hard and Soft Conductive Substrates at Low Temperature in Aqueous Solution. *Chem. Mater.* **2015,** *27* (9), 3389-3396.
50. Carim, A. I.; Collins, S. M.; Foley, J. M.; Maldonado, S., Benchtop Electrochemical Liquid–Liquid–Solid Growth of Nanostructured Crystalline Germanium. *J. Am. Chem. Soc.* **2011,** *133* (34), 13292-13295.
51. Acharya, S.; Ma, L.; Maldonado, S., Critical Factors in the Growth of Hyperdoped Germanium Microwires by Electrochemical Liquid–Liquid–Solid Method. *ACS Applied Nano Materials* **2018,** *1* (10), 5553-5561.

52. Ma, L.; Fahrenkrug, E.; Gerber, E.; Crowe, A. J.; Venable, F.; Bartlett, B. M.; Maldonado, S., High-Performance Polycrystalline Ge Microwire Film Anodes for Li Ion Batteries. *ACS Energy Lett.* **2017,** *2* (1), 238-243.
53. DeMuth, J.; Ma, L.; Lancaster, M.; Acharya, S.; Cheek, Q.; Maldonado, S., Eutectic-Bismuth Indium as a Growth Solvent for the Electrochemical Liquid-Liquid-Solid Deposition of Germanium Microwires and Coiled Nanowires. *Crystal Growth & Design* **2018,** *18* (2), 677-685.
54. Gu, J.; Collins, S. M.; Carim, A. I.; Hao, X.; Bartlett, B. M.; Maldonado, S., Template-Free Preparation of Crystalline Ge Nanowire Film Electrodes via an Electrochemical Liquid–Liquid–Solid Process in Water at Ambient Pressure and Temperature for Energy Storage. *Nano Lett.* **2012,** *12* (9), 4617-4623.
55. Butler, J. N.; Meehan, M. L., Hydrogen evolution on gallium, indium-gallium and mercury-gallium electrodes. *Transactions of the Faraday Society* **1966,** *62* (0), 3524-3534.
56. Butler, J. N.; Dienst, M., Hydrogen Evolution at a Solid Indium Electrode. *J. Electrochem. Soc.* **1965,** *112* (2), 226-232.
57. Frumkin, A.; Polianovskaya, N.; Bagotskaya, I.; Grigoryev, N., Electrocatalysis and electrode surface properties. *Journal of Electroanalytical Chemistry and Interfacial Electrochemistry* **1971,** *33* (2), 319-328.
58. Reeves, G. K.; Harrison, H. B., Obtaining the specific contact resistance from transmission line model measurements. *IEEE Electron Device Lett.* **1982,** *3* (5), 111-113.
59. Sze, S. M.; Ng, K. K., *Physics of Semiconductor Devices*. 3rd ed.; John Wiley & Sons: Hoboken, NJ, 2006.
60. Olesinski, R. W.; Abbaschian, G. J., The Ga−Ge (Gallium-Germanium) system. *Bulletin of Alloy Phase Diagrams* **1985,** *6* (3), 258-262.
61. Cuttriss, D. B., Relation between surface concentration and average conductivity in diffused layers in germanium. *The Bell System Technical Journal* **1961,** *40* (2), 509-521.
62. Reitano, R.; Smith, P. M.; Aziz, M. J., Solute trapping of group III, IV, and V elements in silicon by an aperiodic stepwise growth mechanism. *Journal of Applied Physics* **1994,** *76* (3), 1518-1529.
63. Moutanabbir, O.; Isheim, D.; Blumtritt, H.; Senz, S.; Pippel, E.; Seidman, D. N., Colossal injection of catalyst atoms into silicon nanowires. *Nature* **2013,** *496* (7443), 78-82.
64. Wirths, S.; Buca, D.; Mantl, S., Si–Ge–Sn alloys: From growth to applications. *Prog. Cryst. Growth Charact. Mater.* **2016,** *62* (1), 1-39.
65. Gassenq, A.; Milord, L.; Aubin, J.; Pauc, N.; Guilloy, K.; Rothman, J.; Rouchon, D.; Chelnokov, A.; Hartmann, J. M.; Reboud, V.; Calvo, V., Raman spectral shift versus strain and composition in GeSn layers with 6%–15% Sn content. *Appl. Phys. Lett.* **2017,** *110* (11), 112101.
66. Biswas, S.; Doherty, J.; Saladukha, D.; Ramasse, Q.; Majumdar, D.; Upmanyu, M.; Singha, A.; Ochalski, T.; Morris, M. A.; Holmes, J. D., Non-equilibrium induction of tin in germanium: towards direct bandgap Ge1−xSnx nanowires. *Nat. Commun.* **2016,** *7*, 11405.
67. Barth, S.; Seifner, M. S.; Bernardi, J., Microwave-assisted solution–liquid–solid growth of Ge1−xSnx nanowires with high tin content. *Chemical Communications* **2015,** *51* (61), 12282-12285.
68. Seifner, M. S.; Hernandez, S.; Bernardi, J.; Romano-Rodriguez, A.; Barth, S., Pushing the Composition Limit of Anisotropic Ge1–xSnx Nanostructures and Determination of Their Thermal Stability. *Chemistry of Materials* **2017,** *29* (22), 9802-9813.
69. Kattner, U. R., Phase diagrams for lead-free solder alloys. *JOM* **2002,** *54* (12), 45-51.

70. Mei, Z.; Hua, F.; Glazer, J.; Key, C. C. In *Low temperature soldering*, Twenty First IEEE/CPMT International Electronics Manufacturing Technology Symposium Proceedings 1997 IEMT Symposium, 13-15 Oct. 1997; 1997; pp 463-476.
71. Chen, S.-W.; Wang, C.-H.; Lin, S.-k.; Chiu, C.-N.; N. Subramanian, K., *Phase Diagrams of Pb-Free Solders and Their Related Materials Systems*. 2007; Vol. 38, p 19-37.
72. Andersson, J. O.; Helander, T.; Höglund, L.; Shi, P.; Sundman, B., Thermo-Calc & DICTRA, computational tools for materials science. *Calphad* **2002,** *26* (2), 273-312.
73. Mohney, S. E.; Wang, Y.; Cabassi, M. A.; Lew, K. K.; Dey, S.; Redwing, J. M.; Mayer, T. S., Measuring the specific contact resistance of contacts to semiconductor nanowires. *Solid-State Electron.* **2005,** *49* (2), 227-232.
74. Bard, A. J.; Faulkner, L. R., *Electrochemical Methods: Fundamentals and Applications*. 2 ed.; Wiley: New York, 1980.
75. Khan, M. R.; Eaker, C. B.; Bowden, E. F.; Dickey, M. D., Giant and switchable surface activity of liquid metal via surface oxidation. *Proc. Natl. Acad. Sci.* **2014,** *111* (39), 14047-14051.
76. Wan, Z.; Zeng, H.; Feinerman, A., Reversible Electrowetting of Liquid-Metal Droplet. *J Fluids Eng.* **2006,** *129* (4), 388-394.
77. Gough, R. C.; Morishita, A. M.; Dang, J. H.; Moorefield, M. R.; Shiroma, W. A.; Ohta, A. T., Rapid electrocapillary deformation of liquid metal with reversible shape retention. *Micro and Nano Syst Lett* **2015,** *3* (1), 4.
78. Takeno, N., *Atlas of Eh-pH diagrams Intercomparison of thermodynamic databases*. National Institute of Advanced Industrial Science and Technology: 2005.
79. Yu, F.; Xu, J.; Li, H.; Wang, Z.; Sun, L.; Deng, T.; Tao, P.; Liang, Q., Ga-In liquid metal nanoparticles prepared by physical vapor deposition. *Progress in Natural Science: Materials International* **2018,** *28* (1), 28-33.
80. Alcock, C. B.; Itkin, V. P.; Horrigan, M. K., Vapour Pressure Equations for the Metallic Elements: 298–2500K. *Can. Metall. Q.* **1984,** *23* (3), 309-313.
81. Geiger, F.; Busse, C. A.; Loehrke, R. I., The vapor pressure of indium, silver, gallium, copper, tin, and gold between 0.1 and 3.0 bar. *International Journal of Thermophysics* **1987,** *8* (4), 425-436.
82. Christesen, J. D.; Pinion, C. W.; Zhang, X.; McBride, J. R.; Cahoon, J. F., Encoding Abrupt and Uniform Dopant Profiles in Vapor–Liquid–Solid Nanowires by Suppressing the Reservoir Effect of the Liquid Catalyst. *ACS Nano* **2014,** *8* (11), 11790-11798.
83. Pinion, C. W.; Christesen, J. D.; Cahoon, J. F., Understanding the vapor-liquid-solid mechanism of Si nanowire growth and doping to synthetically encode precise nanoscale morphology. *J. Mater. Chem. C* **2016,** *4* (18), 3890-3897.
84. Pinion, C. W.; Nenon, D. P.; Christesen, J. D.; Cahoon, J. F., Identifying Crystallization- and Incorporation-Limited Regimes during Vapor–Liquid–Solid Growth of Si Nanowires. *ACS Nano* **2014,** *8* (6), 6081-6088.
85. Zhang, T. F., Eli; Maldonado, S., Electrochemical Liquid-Liquid-Solid Deposition of Ge at Hg Microdroplet Ultramicroelectrodes. *J. Electrochem. Soc.* **2016,** *163* (9), D500-D505.
86. Liang, X.; Zhang, Q.; Lay, M. D.; Stickney, J. L., Growth of Ge Nanofilms Using Electrochemical Atomic Layer Deposition, with a "Bait and Switch" Surface-Limited Reaction. *J. Am. Chem. Soc.* **2011,** *133* (21), 8199-8204.
87. Crank, J., *The Mathematics of Diffusion*. Clarendon Press: Oxford, 1975.
88. Arrigan, D. W. M., Nanoelectrodes, nanoelectrode arrays and their applications. *Analyst* **2014,** *129*, 1157-1165.

89. Ross, C. A., Electrodeposited Multilayer Thin Films. *Annu. Rev. Mater. Sci.* **1994,** *24* (1), 159-188.
90. Frari, D. D.; Diliberto, S.; Stein, N.; Boulanger, C.; Lecuire, J.-M., Pulsed electrodeposition of (Bi1-xSbx)2Te3 thermoelectric thin films. *J. Appl. Electrochem.* **2006,** *36* (4), 449-454.
91. Chandrasekar, M. S.; Pushpavanam, M., Pulse and pulse reverse plating—Conceptual, advantages and applications. *Electrochim. Acta* **2008,** *53* (8), 3313-3322.
92. Inguanta, R.; Piazza, S.; Sunseri, C., Influence of electrodeposition techniques on Ni nanostructures. *Electrochim. Acta* **2008,** *53* (19), 5766-5773.
93. Qing, Q.; Jiang, Z.; Xu, L.; Gao, R.; Mai, L.; Lieber, C. M., Free-standing kinked nanowire transistor probes for targeted intracellular recording in three dimensions. *Nat. Nanotechnol.* **2013,** *9*, 142.
94. Xu, L.; Jiang, Z.; Qing, Q.; Mai, L.; Zhang, Q.; Lieber, C. M., Design and Synthesis of Diverse Functional Kinked Nanowire Structures for Nanoelectronic Bioprobes. *Nano Lett.* **2013,** *13* (2), 746-751.
95. Tian, B.; Xie, P.; Kempa, T. J.; Bell, D. C.; Lieber, C. M., Single-crystalline kinked semiconductor nanowire superstructures. *Nat. Nanotechnol.* **2009,** *4*, 824.
96. Musin, I. R.; Filler, M. A., Chemical Control of Semiconductor Nanowire Kinking and Superstructure. *Nano Lett.* **2012,** *12* (7), 3363-3368.
97. Shin, N.; Filler, M. A., Controlling Silicon Nanowire Growth Direction via Surface Chemistry. *Nano Lett.* **2012,** *12* (6), 2865-2870.
98. Dickey, M. D., Emerging Applications of Liquid Metals Featuring Surface Oxides. *ACS Appl. Mater. Interfaces* **2014,** *6* (21), 18369-18379.
99. Gao, M.; Gui, L., A handy liquid metal based electroosmotic flow pump. *Lab Chip* **2014,** *14* (11), 1866-1872.
100. Kwang-Seok, Y.; Il-Joo, C.; Jong-Uk, B.; Chang-Jin, K.; Euisik, Y., A surface-tension driven micropump for low-voltage and low-power operations. *J. Microelectromech. Syst.* **2002,** *11* (5), 454-461.
101. Li, Y.; Wang, Y.; Ryu, S.; Marshall, A. F.; Cai, W.; McIntyre, P. C., Spontaneous, Defect-Free Kinking via Capillary Instability during Vapor–Liquid–Solid Nanowire Growth. *Nano Lett.* **2016,** *16* (3), 1713-1718.
102. Tang, S.-Y.; Khoshmanesh, K.; Sivan, V.; Petersen, P.; O'Mullane, A. P.; Abbott, D.; Mitchell, A.; Kalantar-zadeh, K., Liquid metal enabled pump. *Proc. Natl. Acad. Sci.* **2014,** *111* (9), 3304-3309.
103. Solanki, A.; Crozier, K., Vertical germanium nanowires as spectrally-selective absorbers across the visible-to-infrared. *Applied Physics Letters* **2014,** *105* (19), 191115.
104. Holmberg, V. C.; Bogart, T. D.; Chockla, A. M.; Hessel, C. M.; Korgel, B. A., Optical Properties of Silicon and Germanium Nanowire Fabric. *The Journal of Physical Chemistry C* **2012,** *116* (42), 22486-22491.
105. Zhao, J.; Yu, X.; Yang, X.; Th Tee, C. A.; Yuan, W.; Yu, Y., Polarization-independent and high-efficiency broadband optical absorber in visible light based on nanostructured germanium arrays. *Opt. Lett.* **2019,** *44* (4), 963-966.
106. Zhou, L.; Tan, Y.; Wang, J.; Xu, W.; Yuan, Y.; Cai, W.; Zhu, S.; Zhu, J., 3D self-assembly of aluminium nanoparticles for plasmon-enhanced solar desalination. *Nature Photonics* **2016,** *10*, 393.

107. Zhou, L.; Tan, Y.; Ji, D.; Zhu, B.; Zhang, P.; Xu, J.; Gan, Q.; Yu, Z.; Zhu, J., Self-assembly of highly efficient, broadband plasmonic absorbers for solar steam generation. *Science Advances* **2016,** *2* (4).
108. Bian, Y.; Du, Q.; Tang, K.; Shen, Y.; Hao, L.; Zhou, D.; Wang, X.; Xu, Z.; Zhang, H.; Zhao, L.; Zhu, S.; Ye, J.; Lu, H.; Yang, Y.; Zhang, R.; Zheng, Y.; Gu, S., Carbonized Bamboos as Excellent 3D Solar Vapor-Generation Devices. *Advanced Materials Technologies* **2019,** *4* (4), 1800593.
109. Zhang, X. A.; Yu, S.; Xu, B.; Li, M.; Peng, Z.; Wang, Y.; Deng, S.; Wu, X.; Wu, Z.; Ouyang, M.; Wang, Y., Dynamic gating of infrared radiation in a textile. *Science* **2019,** *363* (6427), 619-623.
110. Shi, H.; Ok, J. G.; Baac, H. W.; Guo, L. J., Low density carbon nanotube forest as an index-matched and near perfect absorption coating. *Applied Physics Letters* **2011,** *99* (21), 211103.
111. Arsenault, A. C.; Puzzo, D. P.; Manners, I.; Ozin, G. A., Photonic-crystal full-colour displays. *Nat. Photon.* **2007,** *1*, 468-472.
112. Hong, J.; Chan, E.; Chang, T.; Fung, T.-C.; Hong, B.; Kim, C.; Ma, J.; Pan, Y.; Lier, R. V.; Wang, S.-g.; Wen, B.; Zhou, L., Continuous color reflective displays using interferometric absorption. *Optica* **2015,** *2* (7), 589-597.
113. Zhu, X.; Vannahme, C.; Højlund-Nielsen, E.; Mortensen, N. A.; Kristensen, A., Plasmonic colour laser printing. *Nat. Nanotechnol.* **2016,** *11* (4), 325-329.
114. Kim, H.; Ge, J.; Kim, J.; Choi, S.-e.; Lee, H.; Lee, H.; Park, W.; Yin, Y.; Kwon, S., Structural colour printing using a magnetically tunable and lithographically fixable photonic crystal. *Nat. Photon.* **2009,** *3* (9), 534-540.
115. Lee, K.-T.; Ji, C.; Banerjee, D.; Guo, L. J., Angular- and polarization-independent structural colors based on 1D photonic crystals. *Laser Photon. Rev.* **2015,** *9* (3), 354-362.
116. Masuda, T.; Kudo, Y.; Banerjee, D., Visually Attractive and High-Power-Retention Solar Modules by Coloring with Automotive Paints. *Coatings* **2018,** *8* (8), 282.
117. Masuda, T.; Hirai, S.; Inoue, M.; Chantana, J.; Kudo, Y.; Minemoto, T., Colorful, Flexible, and Lightweight Cu(In,Ga)Se2 Solar Cell by Lift-Off Process With Automotive Painting. *IEEE J. Photovolt.* **2018,** *8* (5), 1326-1330.
118. Ji, C.; Lee, K.-T.; Xu, T.; Zhou, J.; Park, H. J.; Guo, L. J., Engineering Light at the Nanoscale: Structural Color Filters and Broadband Perfect Absorbers. *Adv. Opt. Mater.* **2017,** *5* (20), 1700368.
119. Xu, G.; Shen, L.; Cui, C.; Wen, S.; Xue, R.; Chen, W.; Chen, H.; Zhang, J.; Li, H.; Li, Y.; Li, Y., High-Performance Colorful Semitransparent Polymer Solar Cells with Ultrathin Hybrid-Metal Electrodes and Fine-Tuned Dielectric Mirrors. *Adv. Funct. Mater.* **2017,** *27* (15), 1605908.
120. Lu, J.-H.; Lin, Y.-H.; Jiang, B.-H.; Yeh, C.-H.; Kao, J.-C.; Chen, C.-P., Microcavity Structure Provides High-Performance (>8.1%) Semitransparent and Colorful Organic Photovoltaics. *Adv. Funct. Mater.* **2017,** *28* (7), 1703398.
121. Ji, C.; Zhang, Z.; Masuda, T.; Kudo, Y.; Guo, L. J., Vivid-colored silicon solar panels with high efficiency and non-iridescent appearance. *Nanoscale Horiz.* **2019,** *in press*, DOI: 10.1039/C8NH00368H.
122. Sabnis, R. W., Color filter technology for liquid crystal displays. *Displays* **1999,** *20* (3), 119-129.

123. Xiao, M.; Li, Y.; Allen, M. C.; Deheyn, D. D.; Yue, X.; Zhao, J.; Gianneschi, N. C.; Shawkey, M. D.; Dhinojwala, A., Bio-Inspired Structural Colors Produced via Self-Assembly of Synthetic Melanin Nanoparticles. *ACS Nano* **2015,** *9* (5), 5454-5460.
124. Mihi, A.; Ocaña, M.; Míguez, H., Oriented Colloidal-Crystal Thin Films by Spin-Coating Microspheres Dispersed in Volatile Media. *Adv. Mater.* **2006,** *18* (17), 2244-2249.
125. Gao, W.; Rigout, M.; Owens, H., Self-assembly of silica colloidal crystal thin films with tuneable structural colours over a wide visible spectrum. *Appl. Surf. Sci.* **2016,** *380*, 12-15.
126. Shim, T. S.; Kim, S.-H.; Sim, J. Y.; Lim, J.-M.; Yang, S.-M., Dynamic Modulation of Photonic Bandgaps in Crystalline Colloidal Arrays Under Electric Field. *Adv. Mater.* **2010,** *22* (40), 4494-4498.
127. Park, J.-G.; Benjamin Rogers, W.; Magkiriadou, S.; Kodger, T.; Kim, S.-H.; Kim, Y.-S.; Manoharan, V. N., Photonic-crystal hydrogels with a rapidly tunable stop band and high reflectivity across the visible. *Opt. Mater. Express* **2017,** *7* (1), 253-263.
128. Li, F.; Tang, B.; Zhang, S., Iridescent structural colors from self-assembled polymer opal of polythiourethane microspheres. *Dyes Pigm.* **2017,** *142*, 371-378.
129. Gao, W.; Rigout, M.; Owens, H., Optical properties of cotton and nylon fabrics coated with silica photonic crystals. *Opt. Mater. Express* **2017,** *7* (2), 341-353.
130. Gao, W.; Rigout, M.; Owens, H., The structural coloration of textile materials using self-assembled silica nanoparticles. *J. Nanopart. Res.* **2017,** *19* (9), 303.
131. Josell, D.; Wheeler, D.; Huber, W. H.; Moffat, T. P., Superconformal Electrodeposition in Submicron Features. *Phys. Rev. Lett.* **2001,** *87* (1), 016102.
132. Ozel, T.; Zhang, B. A.; Gao, R.; Day, R. W.; Lieber, C. M.; Nocera, D. G., Electrochemical Deposition of Conformal and Functional Layers on High Aspect Ratio Silicon Micro/Nanowires. *Nano. Lett.* **2017,** *17* (7), 4502-4507.
133. Inoue, F.; Harada, Y.; Koyanagi, M.; Fukushima, T.; Yamamoto, K.; Tanaka, S.; Wang, Z.; Shingubara, S., Perfect conformal deposition of electroless Cu for high aspect ratio through-Si vias. *Electrochem. Solid-State Lett.* **2009,** *12* (10), H381-H384.
134. Gunawardena, G.; Hills, G.; Montenegro, I.; Scharifker, B., Electrochemical nucleation: Part I. General considerations. *J. Electroanal. Chem. Interfacial Electrochem.* **1982,** *138* (2), 225-239.
135. Gunawardena, G.; Hills, G.; Montenegro, I., Electrochemical nucleation: Part II. The electrodeposition of silver on vitreous carbon. *J. Electroanal. Chem. Interfacial Electrochem.* **1982,** *138* (2), 241-254.
136. Ji, C.; Acharya, S.; Yamada, K.; Maldonado, S.; Guo, L. J., Electrodeposition of Large Area, Angle-Insensitive Multilayered Structural Colors. *ACS Applied Materials & Interfaces* **2019,** *11* (32), 29065-29071.
137. Acharya, S.; Ji, C.; Guo, L. J. In *Solution-Processed Angle-Insensitive Structural Colors via Electrodeposition of Thin-Films*, Optical Interference Coatings Conference (OIC) 2019, Santa Ana Pueblo, New Mexico, 2019/06/02; Optical Society of America: Santa Ana Pueblo, New Mexico, 2019; p MD.4.
138. Hoeckelman, R. F., Optical Properties of Chromium-Plated Steel. *J. Electrochem. Soc.* **1972,** *119* (10), 1310-1315.
139. Fredj, N.; Burleigh, T. D., Transpassive dissolution of copper and rapid formation of brilliant colored copper oxide films. *J. Electrochem. Soc.* **2011,** *158* (4), C104-C110.
140. Ogura, K.; Lou, W.; Nakayama, M., Coloration of stainless steel at room temperature by triangular current scan method. *Electrochimica Acta* **1996,** *41* (18), 2849-2853.

141. Prod'homme, P.; Maroun, F.; Cortès, R.; Allongue, P., Electrochemical growth of ultraflat Au(111) epitaxial buffer layers on H–Si(111). *Appl. Phys. Lett.* **2008,** *93* (17), 171901.
142. Switzer, J. A.; Hill, J. C.; Mahenderkar, N. K.; Liu, Y.-C., Nanometer-Thick Gold on Silicon as a Proxy for Single-Crystal Gold for the Electrodeposition of Epitaxial Cuprous Oxide Thin Films. *ACS Applied Materials & Interfaces* **2016,** *8* (24), 15828-15837.
143. Mahenderkar, N. K.; Chen, Q.; Liu, Y.-C.; Duchild, A. R.; Hofheins, S.; Chason, E.; Switzer, J. A., Epitaxial lift-off of electrodeposited single-crystal gold foils for flexible electronics. *Science* **2017,** *355* (6330), 1203-1206.
144. Patricia, P.; Samantha, W.; Robert, C.; Feitosa, J. H.; Fouad, M.; Philippe, A., Epitaxial Growth of Gold on H-Si(111): The Determining Role of Hydrogen Evolution. *ChemPhysChem* **2010,** *11* (13), 2992-3001.
145. Eskhult, J.; Nyholm, L., Pulsed Galvanostatic and Potentiostatic Electrodeposition of Cu and Cu2O Nanolayers from Alkaline Cu(II)-Citrate Solutions. *J. Electrochem. Soc.* **2008,** *155* (2), D115-D122.
146. Eskhult, J.; Herranen, M.; Nyholm, L., On the origin of the spontaneous potential oscillations observed during galvanostatic deposition of layers of Cu and Cu2O in alkaline citrate solutions. *Journal of Electroanalytical Chemistry* **2006,** *594* (1), 35-49.
147. Switzer, J. A.; Hung, C.-J.; Huang, L.-Y.; Miller, F. S.; Zhou, Y.; Raub, E. R.; Shumsky, M. G.; Bohannan, E. W., Potential oscillations during the electrochemical self-assembly of copper/cuprous oxide layered nanostructures. *J. Mater. Res.* **2011,** *13* (4), 909-916.
148. Switzer, J. A.; Hung, C.-J.; Huang, L.-Y.; Switzer, E. R.; Kammler, D. R.; Golden, T. D.; Bohannan, E. W., Electrochemical Self-Assembly of Copper/Cuprous Oxide Layered Nanostructures. *Journal of the American Chemical Society* **1998,** *120* (14), 3530-3531.
149. Bohannan, E. W.; Huang, L.-Y.; Miller, F. S.; Shumsky, M. G.; Switzer, J. A., In Situ Electrochemical Quartz Crystal Microbalance Study of Potential Oscillations during the Electrodeposition of Cu/Cu2O Layered Nanostructures. *Langmuir* **1999,** *15* (3), 813-818.
150. Mishina, E. D.; Nagai, K.; Nakabayashi, S., Self-Assembled Cu/Cu2O Multilayers: Deposition, Structure and Optical Properties. *Nano Letters* **2001,** *1* (8), 401-404.
151. Beverskog, B.; Puigdomenech, I., Revised Pourbaix diagrams for copper at 25 to 300°C. *J. Electrochem. Soc.* **1997,** *144* (10), 3476-3483.
152. Petterson, L. A. A.; Roman, L. S.; Inganäs, O., Modeling photocurrent action spectra of photovoltaic devices based on organic thin films. *J. Appl. Phys.* **1999,** *86* (1), 487-496.
153. Drobny, V. F.; Pulfrey, L., Properties of reactively-sputtered copper oxide thin films. *Thin Solid Films* **1979,** *61* (1), 89-98.
154. Ji, C.; Lee, K.-T.; Guo, L. J., High-color-purity, angle-invariant, and bidirectional structural colors based on higher-order resonances. *Opt. Lett.* **2019,** *44* (1), 86-89.
155. Zulian, L.; Emilitri, E.; Scavia, G.; Botta, C.; Colombo, M.; Destri, S., Structural Iridescent Tuned Colors from Self-Assembled Polymer Opal Surfaces. *ACS Appl. Mater. Interfaces* **2012,** *4* (11), 6071-6079.
156. Park, H. J.; Xu, T.; Lee, J. Y.; Ledbetter, A.; Guo, L. J., Photonic Color Filters Integrated with Organic Solar Cells for Energy Harvesting. *ACS Nano* **2011,** *5* (9), 7055-7060.
157. Park, C.-H.; Yoon, Y.-T.; Lee, S.-S., Polarization-independent visible wavelength filter incorporating a symmetric metal-dielectric resonant structure. *Opt. Express* **2012,** *20* (21), 23769-23777.
158. Chalker, P. R.; Bull, S. J.; Rickerby, D. S., A review of the methods for the evaluation of coating-substrate adhesion. *Mater. Sci. Eng. A* **1991,** *140*, 583-592.

159. Peacock, W. Method of making mirrors. US2363354A, Nov 21 1944.
160. Fujimoto, S.; Shibata, T.; Wada, K.; Tsutae, T., The electrochemical conditions for coloured film formation on type 304 stainless steel with square wave polarization. *Corrosion Science* **1993,** *35* (1), 147-152.
161. Hogg, S. W.; Smith, G. B., The unusual and useful optical properties of electrodeposited chrome-black films. *Journal of Physics D: Applied Physics* **1977,** *10* (13), 1863-1869.
162. Junqueira, R. M. R.; Loureiro, C. R. d. O.; Andrade, M. S.; Buono, V. T. L., Characterization of interference thin films grown on stainless steel surface by alternate pulse current in a sulphochromic solution. *Mater. Res.* **2008,** *11* (4), 421-426.
163. Evans, T. E., Film formation on stainless steel in a solution containing chromic and sulphuric acids. *Corrosion Science* **1977,** *17* (2), 105-124.
164. Sørensen, P. A.; Kiil, S.; Dam-Johansen, K.; Weinell, C. E., Anticorrosive coatings: a review. *J. Coat. Technol. Res.* **2009,** *6* (2), 135-176.
165. Benedict, S. R., A reagent for the detection of reducing sugars. *J. Biol. Chem.* **1909,** *5* (5), 485-487.
166. Fulop, G. F.; Taylor, R. M., Electrodeposition of semiconductors. *Annu. Rev. Mater. Sci.* **1985,** *15* (1), 197-210.
167. Natarajan, C.; Nogami, G., Cathodic electrodeposition of nanocrystalline titanium dioxide thin films. *J. Electrochem. Soc.* **1996,** *143* (5), 1547-1550.
168. Lincot, D., Electrodeposition of semiconductors. *Thin Solid Films* **2005,** *487* (1), 40-48.
169. Graham-Rowe, D., Tunable structural colour. *Nature Photonics* **2009,** *3*, 551.
170. Palm, K. J.; Murray, J. B.; Narayan, T. C.; Munday, J. N., Dynamic Optical Properties of Metal Hydrides. *ACS Photonics* **2018,** *5* (11), 4677-4686.
171. Duan, X.; Kamin, S.; Liu, N., Dynamic plasmonic colour display. *Nature Communications* **2017,** *8*, 14606.
172. Araki, S.; Nakamura, K.; Kobayashi, K.; Tsuboi, A.; Kobayashi, N., Electrochemical Optical-Modulation Device with Reversible Transformation Between Transparent, Mirror, and Black. *Advanced Materials* **2012,** *24* (23), OP122-OP126.
173. Onodera, R.; Tsuboi, A.; Nakamura, K.; Kobayashi, N., Coloration mechanisms of Ag deposition-based multicolor electrochromic device investigated by morphology of Ag deposit and its optical properties. *Journal of the Society for Information Display* **2016,** *24* (7), 424-432.
174. Tomoko Sugita, K. N., Norihisa Kobayashi, Improvement of Chroma and Theoretical Analysis of Silver DepositionBased Multicolor Electrochromic Device. *SID 2019 DIGEST* **2019**.
175. Luo, Z.; Evans, B. A.; Chang, C.-H., Magnetically Actuated Dynamic Iridescence Inspired by the Neon Tetra. *ACS Nano* **2019**.
176. Raj Shrestha, V.; Lee, S.-S.; Kim, E.-S.; Choi, D.-Y., Polarization-tuned Dynamic Color Filters Incorporating a Dielectric-loaded Aluminum Nanowire Array. *Scientific Reports* **2015,** *5*, 12450.
177. Park, J.; Kang, J.-H.; Kim, S. J.; Liu, X.; Brongersma, M. L., Dynamic Reflection Phase and Polarization Control in Metasurfaces. *Nano Letters* **2017,** *17* (1), 407-413.
178. Jafari, M.; Guo, L. J.; Rais-Zadeh, M., A Reconfigurable Color Reflector by Selective Phase Change of GeTe in a Multilayer Structure. *Advanced Optical Materials* **2019,** *7* (5), 1801214.
179. Aalizadeh, M.; Serebryannikov, A. E.; Khavasi, A.; Vandenbosch, G. A. E.; Ozbay, E., Toward Electrically Tunable, Lithography-Free, Ultra-Thin Color Filters Covering the Whole Visible Spectrum. *Scientific Reports* **2018,** *8* (1), 11316.

180. Mirshafieyan, S. S.; Gregory, D. A., Electrically tunable perfect light absorbers as color filters and modulators. *Scientific Reports* **2018,** *8* (1), 2635.
181. Kim, S. J.; Brongersma, M. L., Active flat optics using a guided mode resonance. *Opt. Lett.* **2017,** *42* (1), 5-8.
182. Granqvist, C. G., *Handbook of Inorganic Electrochromic Materials*. Elsevier Science B.V.: Amsterdam, 1995.
183. Svensson, J. S. E. M.; Granqvist, C. G., Electrochromic tungsten oxide films for energy efficient windows. *Solar Energy Materials* **1984,** *11* (1), 29-34.
184. Talledo, A.; Granqvist, C. G., Electrochromic vanadium–pentoxide–based films: Structural, electrochemical, and optical properties. *Journal of Applied Physics* **1995,** *77* (9), 4655-4666.
185. Bange, K.; Gambke, T., Electrochromic Materials for optical switching devices. *Advanced Materials* **1990,** *2* (1), 10-16.
186. Somani, P. R.; Radhakrishnan, S., Electrochromic materials and devices: present and future. *Materials Chemistry and Physics* **2003,** *77* (1), 117-133.
187. Baucke, F. G. K.; Bange, K.; Gambke, T., Reflecting electrochromic devices. *Displays* **1988,** *9* (4), 179-187.
188. Wangati, C. K.; Njoroge, W. K.; Okumu, J., Influence of Deposition Parameters on the Optical Properties of Thin Tungsten Oxide Films Prepared By Reactive De Magnetron Sputtering. *East African Journal of Physical Sciences* **2008,** *8* (1).
189. Nagai, J.; Kamimori, T., Kinetic Study of LixWO3Electrochromism. *Japanese Journal of Applied Physics* **1983,** *22* (Part 1, No. 4), 681-687.
190. Parreira, N. M. G.; Carvalho, N. J. M.; Cavaleiro, A., Synthesis, structural and mechanical characterization of sputtered tungsten oxide coatings. *Thin Solid Films* **2006,** *510* (1), 191-196.
191. Dyer, A. L.; Thompson, E. J.; Reynolds, J. R., Completing the Color Palette with Spray-Processable Polymer Electrochromics. *ACS Applied Materials & Interfaces* **2011,** *3* (6), 1787-1795.
192. Beaujuge, P. M.; Amb, C. M.; Reynolds, J. R., A Side-Chain Defunctionalization Approach Yields a Polymer Electrochrome Spray-Processable from Water. *Advanced Materials* **2010,** *22* (47), 5383-5387.
193. Chen, B.-H.; Kao, S.-Y.; Hu, C.-W.; Higuchi, M.; Ho, K.-C.; Liao, Y.-C., Printed Multicolor High-Contrast Electrochromic Devices. *ACS Applied Materials & Interfaces* **2015,** *7* (45), 25069-25076.
194. Cai, G.; Wang, J.; Lee, P. S., Next-Generation Multifunctional Electrochromic Devices. *Accounts of Chemical Research* **2016,** *49* (8), 1469-1476.
195. Cai, G.; Darmawan, P.; Cui, M.; Chen, J.; Wang, X.; Eh, A. L.-S.; Magdassi, S.; Lee, P. S., Inkjet-printed all solid-state electrochromic devices based on NiO/WO3 nanoparticle complementary electrodes. *Nanoscale* **2016,** *8* (1), 348-357.
196. Kim, J.; Ong, G. K.; Wang, Y.; LeBlanc, G.; Williams, T. E.; Mattox, T. M.; Helms, B. A.; Milliron, D. J., Nanocomposite Architecture for Rapid, Spectrally-Selective Electrochromic Modulation of Solar Transmittance. *Nano Letters* **2015,** *15* (8), 5574-5579.
197. Xu, T.; Walter, E. C.; Agrawal, A.; Bohn, C.; Velmurugan, J.; Zhu, W.; Lezec, H. J.; Talin, A. A., High-contrast and fast electrochromic switching enabled by plasmonics. *Nature Communications* **2016,** *7*, 10479.
198. Nguyen, C. A.; Xiong, S.; Ma, J.; Lu, X.; Lee, P. S., High ionic conductivity P(VDF-TrFE)/PEO blended polymer electrolytes for solid electrochromic devices. *Physical Chemistry Chemical Physics* **2011,** *13* (29), 13319-13326.

199. Duek, E. A. R.; De Paoli, M.-A.; Mastragostino, M., A solid-state electrochromic device based on polyaniline, prussian blue and an elastomeric electrolyte. *Advanced Materials* **1993,** *5* (9), 650-652.
200. De Paoli, M. A.; Casalbore-Miceli, G.; Girotto, E. M.; Gazotti, W. A., All polymeric solid state electrochromic devices. *Electrochimica Acta* **1999,** *44* (18), 2983-2991.
201. Wagner, W.; Rauch, F.; Bange, K., Concentration profiles of hydrogen in technical oxidic thin films

and multilayer systems. *Fresenius Z Anal Chem* **1989,** *333*, 478-480.
202. Wagner, W.; Rauch, F.; Ottermann, C.; Bange, K., In-depth profiling of hydrogen in oxidic multilayer systems. *Surface and Interface Analysis* **1990,** *16* (1-12), 331-334.
203. Bard, A.; Faulkner, L., *Electrochemical Methods: Fundamentals and Applications*. 2nd ed.; John Wiley & Sons: New York, 2001.
204. Mirkin, M. V., Determination of Electrode Kinetics. In *Handbook of Electrochemistry*, Zoski, C. G., Ed. Elsevier: Amsterdam, 2007; pp 639-660.
205. Bond, A. M.; Henderson, T. L. E.; Mann, D. R.; Mann, T. F.; Thormann, W.; Zoski, C. G., A fast electron transfer rate for the oxidation of ferrocene in acetonitrile or dichloromethane at platinum disk ultramicroelectrodes. *Analytical Chemistry* **1988,** *60* (18), 1878-1882.
206. Shao, Y.; Mirkin, M. V.; Fish, G.; Kokotov, S.; Palanker, D.; Lewis, A., Nanometer-Sized Electrochemical Sensors. *Analytical Chemistry* **1997,** *69* (8), 1627-1634.
207. Sun, P.; Mirkin, M. V., Kinetics of Electron-Transfer Reactions at Nanoelectrodes. *Analytical Chemistry* **2006,** *78* (18), 6526-6534.
208. Li, Y.; Bergman, D.; Zhang, B., Preparation and Electrochemical Response of 1−3 nm Pt Disk Electrodes. *Analytical Chemistry* **2009,** *81* (13), 5496-5502.
209. Zhang, B.; Fan, L.; Zhong, H.; Liu, Y.; Chen, S., Graphene Nanoelectrodes: Fabrication and Size-Dependent Electrochemistry. *Journal of the American Chemical Society* **2013,** *135* (27), 10073-10080.
210. Chen, R.; Nioradze, N.; Santhosh, P.; Li, Z.; Surwade, S. P.; Shenoy, G. J.; Parobek, D. G.; Kim, M. A.; Liu, H.; Amemiya, S., Ultrafast Electron Transfer Kinetics of Graphene Grown by Chemical Vapor Deposition. **2015,** *54* (50), 15134-15137.
211. Bond, A. M.; Oldham, K. B.; Zoski, C. G., Theory of Electrochemical Processes at an Inlaid Disc Microelectrode Under Steady-State Conditions. *J. Electroanal. Chem.* **1988,** *245*, 71-104.
212. Yu, Y.; Sun, T.; Mirkin, M. V., Toward More Reliable Measurements of Electron-Transfer Kinetics at Nanoelectrodes: Next Approximation. *Analytical Chemistry* **2016,** *88* (23), 11758-11766.
213. Zhang, B.; Zhang, Y.; White, H. S., The Nanopore Electrode. *Analytical Chemistry* **2004,** *76* (21), 6229-6238.
214. Zoski, C. G., Ultramicroelectrodes: Design, fabrication, and characterization. *Electroanalysis* **2002,** *14* (15-16), 1041-1051.
215. Bond, A. M.; Luscombe, D.; Oldham, K. B.; Zoski, C. G., A Comparison of the Chronoamperometric Response at Inlaid and Recessed Disc Microelectrodes. *J. Electroanal. Chem.* **1988,** *249*, 1-14.
216. Bartlett, P. N.; Taylor, S. L., An accurate microdisc simulation model for recessed microdisc electrodes. *Journal of Electroanalytical Chemistry* **1998,** *453* (1-2), 49-60.
217. Britz, D.; Strutwolf, J., Electroanalytical response of an ultramicroelectrode at the bottom of an insulating conical well: Digital simulation. *Electrochimica Acta* **2006,** *52* (1), 33-41.

218. Amatore, C.; Oleinick, A. I.; Svir, I., Construction of optimal quasi-conformal mappings for the 2D-numerical simulation of diffusion at microelectrodes. Part 1: Principle of the method and its application to the inlaid disk microelectrode. *Journal of Electroanalytical Chemistry* **2006,** *597* (1), 69-76.
219. Aguiar, F. A.; Gallant, A. J.; Rosamond, M. C.; Rhodes, A.; Wood, D.; Kataky, R., Conical recessed gold microelectrode arrays produced during photolithographic methods: Characterisation and causes. *Electrochemistry Communications* **2007,** *9* (5), 879-885.
220. Amatore, C.; Oleinick, A. I.; Svir, I., Numerical Simulation of Diffusion Processes at Recessed Disk Microelectrode Arrays Using the Quasi-Conformal Mapping Approach. *Anal. Chem.* **2009,** *81* (11), 4397-4405.
221. Guo, J.; Lindner, E., Cyclic Voltammograms at Coplanar and Shallow Recessed Microdisk Electrode Arrays: Guidelines for Design and Experiment. *Analytical Chemistry* **2009,** *81* (1), 130-138.
222. Guo, J.; Lindner, E., Cyclic voltammetry at shallow recessed microdisc electrode: Theoretical and experimental study. *Journal of Electroanalytical Chemistry* **2009,** *629* (1), 180-184.
223. Simonov, A. N.; Morris, G. P.; Mashkina, E. A.; Bethwaite, B.; Gillow, K.; Baker, R. E.; Gavaghan, D. J.; Bond, A. M., Inappropriate Use of the Quasi-Reversible Electrode Kinetic Model in Simulation-Experiment Comparisons of Voltammetric Processes That Approach the Reversible Limit. *Analytical Chemistry* **2014,** *86* (16), 8408-8417.
224. Baranski, A. S., On Possible Systematic-Errors in Determinations of Charge-Transfer Kinetics at Very Small Electrodes. *J. Electroanal. Chem.* **1991,** *307* (1-2), 287-292.
225. Oldham, K. B., A hole can serve as a microelectrode. *Analytical Chemistry* **1992,** *64* (6), 646-651.
226. Nogala, W.; Velmurugan, J.; Mirkin, M. V., Atomic Force Microscopy of Electrochemical Nanoelectrodes. *Analytical Chemistry* **2012,** *84* (12), 5192-5197.
227. Streetman, B. G.; Banerjee, S. K., *Solid State Electronic Devices*. 6th ed.; Pearson Education: Upper Saddle River, NJ, 2006.
228. Decker, F.; Fracastoro-Decker, M.; Badawy, W.; Dolbhafter, K.; Gerischer, H., The Photocurrent-Voltage Characteristics of the Heterojunction Combination n-Si/SnO_2/Redox Electrolyte. *J. Electrochem. Soc.* **1983,** *130* (11), 2173-2179.
229. Bruckenstein, S.; Rosamilia, J. M.; Miller, B., Coupled Photovoltaic Junction-Metal Dissolution Elements Under Mass and Light Flux Variation. *J. Phys. Chem.* **1985,** *89*, 677-681.
230. Koval, C. A.; Howard, J. N., Electron Transfer at Semiconductor Electrode-Liquid Electrolyte Interfaces. *Chem. Rev.* **1992,** *92* (3), 411-433.
231. Acharya, S.; Lancaster, M.; Maldonado, S., Semiconductor Ultramicroelectrodes: Platforms for Studying Charge-Transfer Processes at Semiconductor/Liquid Interfaces. *Analytical Chemistry* **2018,** *90* (20), 12261-12269.
232. Marcus, R. A., On Theory of Electron-Transfer Reactions .6. Unified Treatment for Homogeneous and Electrode Reactions. *J. Chem. Phys.* **1965,** *43* (2), 679-701.
233. Frese, K. W., A Study of Rearrangement Energies of Redox Species. *J. Phys. Chem.* **1981,** *85* (25), 3911-3916.
234. Royea, W. J.; Hamann, T. W.; Brunschwig, B. S.; Lewis, N. S., A comparison between interfacial electron-transfer rate constants at metallic and graphite electrodes. *J Phys Chem B* **2006,** *110* (39), 19433-19442.

235. Vijaikanth, V.; Li, G. C.; Swaddle, T. W., Kinetics of Reduction of Aqueous Hexaammineruthenium(III) Ion at Pt and Au Microelectrodes: Electrolyte, Temperature, and Pressure Effects. *Inorg. Chem.* **2013,** *52* (5), 2757-2768.
236. *CRC Handbook of Chemistry and Physics*. 99 ed.; CRC Press: 2018.
237. Marcus, R. A., Theory of Electron-Transfer Rates across Liquid Liquid Interfaces .2. Relationships and Application. *J. Phys. Chem.* **1991,** *95* (5), 2010-2013.
238. Green, M. A.; Keevers, M. J., Optical-Properties of Intrinsic Silicon at 300 K. *Prog. Photovoltaics* **1995,** *3* (3), 189-192.
239. Oldham, K. B.; Myland, J. C.; Zoski, C. G.; Bond, A. M., Kinetic parameters from steady-state voltammograms at microdisc electrodes. *J. Electroanal. Chem.* **1989,** *270* (1-2), 79-101.
240. Royea, W. J.; Kruger, O.; Lewis, N. S., Frumkin corrections for heterogeneous rate constants at semiconducting electrodes. *J. Electroanal. Chem.* **1997,** *438* (1-2), 191-197.
241. Sun, Y. Y. T.; Mirkin, M. V., Toward More Reliable Measurements of Electron-Transfer Kinetics at Nanoelectrodes: Next Approximation. *Anal. Chem.* **2016,** *88* (23), 11758-11766.
242. Zettler, R. A.; Cowley, A. M., p-n Junction-Schottky Barrier Hybrid Diode. *IEEE Trans. Electron Dev.* **1969,** *ED-16* (1), 58-63.
243. Lepselter, M. P.; Sze, S. M., Silicon Schottky Barrier Diode with Near-Ideal I-V Characteristics. *Bell Labs Tech. J.* **1968,** *47* (2), 195-208.
244. Natarajan, A.; Oskam, G.; Searson, P., The potential distribution at the semiconductor/solution interface. *J. Phys. Chem. B* **1998,** *102* (40), 7793-7799.
245. Hens, Z.; Gomes, W. P., On the diffusion impedance at semiconductor electrodes. *J. Phys. Chem. B* **1997,** *101* (30), 5814-5821.
246. Lewis, N. S., Progress in understanding electron-transfer reactions at semiconductor/liquid interfaces. *J. Phys. Chem. B* **1998,** *102* (25), 4843-4855.
247. Horrocks, B. R.; Mirkin, M. V.; Bard, A. J., Scanning Electrochemical Microscopy. 25. Application to Investigation of the Kinetics of Heterogeneous Electron Transfer at Semiconductor (WSe_2 and Si) Electrodes. *J. Phys. Chem.* **1994,** *98* (37), 9106-9114.
248. Li, Y. X.; Bergman, D.; Zhang, B., Preparation and Electrochemical Response of 1-3 nm Pt Disk Electrodes. *Anal. Chem.* **2009,** *81* (13), 5496-5502.
249. Lanyon, Y. H.; Arrigan, D. W. M., Recessed nanoband electrodes fabricated by focused ion beam milling. *Sensors and Actuators B-Chemical* **2007,** *121* (1), 341-347.
250. Lanyon, Y. H.; De Marzi, G.; Watson, Y. E.; Quinn, A. J.; Gleeson, J. P.; Redmond, G.; Arrigan, D. W. M., Fabrication of nanopore array electrodes by focused ion beam milling. *Anal. Chem.* **2007,** *79* (8), 3048-3055.
251. Tsushima, M.; Tokuda, K.; Ohsaka, T., Use of Hydrodynamic Chronocoulometry for Simultaneous Determination of Diffusion-Coefficients and Concentrations of Dioxygen in Various Media. *Anal. Chem.* **1994,** *66* (24), 4551-4556.
252. Hill, C. M.; Kim, J.; Bodappa, N.; Bard, A. J., Electrochemical Nonadiabatic Electron Transfer via Tunneling to Solution Species through Thin Insulating Films. *J. Am. Chem. Soc.* **2017,** *139* (17), 6114-6119.
253. Morita, M.; Ohmi, T.; Hasegawa, E.; Kawakami, M.; Ohwada, M., Growth of Native Oxide on a Silicon Surface. *J. Appl. Phys.* **1990,** *68* (3), 1272-1281.
254. Depas, M.; Vanmeirhaeghe, R. L.; Laflere, W. H.; Cardon, F., Electrical Characteristics of Al/Sio2/N-Si Tunnel-Diodes with an Oxide Layer Grown by Rapid Thermal-Oxidation. *Solid·State Electron.* **1994,** *37* (3), 433-441.

255. Loo, B. H.; Frese, K. W.; Morrison, S. R., The Influence of Surface Oxide-Films on the Stabilization of N-Si Photoelectrode. *Surf. Sci.* **1981,** *109* (1), 75-81.
256. Groner, M. D.; Koval, C. A., Electron transfer at n-silicon methanol interfaces: effects of ferricenium pretreatment and silicon dioxide overlayers. *J. Electroanal. Chem.* **2001,** *498* (1-2), 201-208.
257. Peter, L.; Ushiroda, S., Microwave reflectance studies of photoelectrochemical kinetics at semiconductor electrodes. 3. Photolectrochemical reduction of Ru(NH3)(6)(3+) at p-Si. *J. Phys. Chem. B* **2004,** *108* (8), 2660-2665.
258. Royea, W. J.; Fajardo, A. M.; Lewis, N. S., Fermi golden rule approach to evaluating outer-sphere electron-transfer rate constants at semiconductor/liquid interfaces. *J. Phys. Chem. B* **1997,** *101* (51), 11152-11159.
259. Mandal, K. C.; Ozanam, F.; Chazalviel, J. N., In situ Infrared Evidence for the Electrochemical Incorporation of Hydrogen into Si and Ge. *Appl. Phys. Lett.* **1990,** *57* (26), 2788-2790.
260. Philipsen, H. G. G.; Ozanam, F.; Allongue, P.; Kelly, J. J.; Chazalviel, J. N., In-situ infrared study of silicon in KOH electrolyte: Surface hydrogenation and hydrogen penetration. *Surface Science* **2016,** *644*, 180-190.
261. Rodman, S.; Spitler, M. T., Determination of Rate Constants for Dark Current Reduction at Semiconductor Electrodes Using ZnO Single Crystal Microelectrodes. *J. Phys. Chem. B* **2000,** *8*, 9438-94443.
262. Foley, J. M.; Price, M. J.; Feldblyum, J. I.; Maldonado, S., Analysis of the operation of thin nanowire photoelectrodes for solar energy conversion. *Energy Environ. Sci.* **2012,** *5*, 5203-5220.
263. Hagedorn, K.; Forgacs, C.; Collins, S.; Maldonado, S., Design Considerations for Nanowire Heterojunctions in Solar Energy Conversion/Storage Applications. *J. Phys. Chem. C* **2010,** *114* (27), 12010-12017.
264. Zoski, C. G., Review - Advances in Scanning Electrochemical Microscopy (SECM). *J. Electrochem. Soc.* **2016,** *163* (4), H3088-H3100.
265. Amemiya, S.; Bard, A. J.; Mirkin, M. V.; Unwin, P. R., Scanning Electrochemical Microscopy. *Annu. Rev. Anal. Chem.* **2008,** *1*, 95-131.
266. Mandler, D.; Bard, A. J., High Resolution Etching of Semiconductors by the Feedback Mode of the Scanning Electrochemical Microscope. *J. Electrochem. Soc.* **1990,** *137* (8), 2468-2472.
267. Zhang, J.; Jia, J.; Han, L.; Yuan, Y.; Tian, Z. Q.; Tian, Z. W.; Zhan, D., Kinetic Investigation of the Confined Etching System of n-type Gallium Arsenide by Scanning Electrochemical Microscopy. *J. Phys. Chem. C* **2014,** *118* (32), 18604-18611.
268. Shiue, C. C.; Sah, C. T., New Mobility-Measurement Technique on Inverted Semiconductor Surfaces Near the Conduction Threshold. *Phys. Rev. B* **1979,** *19*, 2149-2162.
269. Hongtao, Y.; Hidekazu, S.; Ye, J.; Sungjae, Y.; Hasniah, A.; Atsushi, T.; Masashi, K.; Yoshihiro, I., Electrostatic and Electrochemical Nature of Liquid-Gated Electrical-Double-Layer Transistors Based on Oxide Semiconductors. *J. Am. Chem. Soc.* **2010,** *132* (51), 18402-18407.
270. Shreve, G. A.; Karp, C. D.; Pomykal, K.; Lewis, N. S., Limits on the Corrosion Rate of Si Surfaces in Contact with CH_3OH-Ferrocene$^{+/0}$ and CH_3OH-1,1'-Dimethylferrocene$^{+/0}$ Solutions. *J. Phys. Chem.* **1995,** *99* (15), 5575-5580.
271. Fajardo, A. M.; Lewis, N. S., Rate constants for charge transfer across semiconductor-liquid interfaces. *Science* **1996,** *274* (5289), 969-972.

272. Fajardo, A. M.; Lewis, N. S., Free-energy dependence of electron-transfer rate constants at Si/liquid interfaces. *J. Phys. Chem. B* **1997,** *101* (51), 11136-11151.
273. Ebejer, N.; Schnippering, M.; Colburn, A. W.; Edwards, M. A.; Unwin, P. R., Localized High Resolution Electrochemistry and Multifunctional Imaging: Scanning Electrochemical Cell Microscopy. *Anal. Chem.* **2010,** *82* (22), 9141-9145.
274. Howard, J. N.; Koval, C. A., Design and Performance of a Minielectrochemical Cell for Spatial-Resolution of 2-Dimensional Structures. *Anal. Chem.* **1991,** *63* (23), 2777-2786.
275. Sharel, P. E.; Kang, M.; Wilson, P.; Meng, L. C.; Perry, D.; Basile, A.; Unwin, P. R., High resolution visualization of the redox activity of Li2O2 in non-aqueous media: conformal layer vs. toroid structure. *Chem. Commun.* **2018,** *54* (24), 3053-3056.
276. Li, T.; Dong, H.; Fu, X.; He, M.; Li, Y.; Hu, W., Microelectrode electrochemistry with semiconducting microelectrode chips. *Small* **2014,** *10* (5), 878-83.
277. Hamann, T. W.; Lewis, N. S., Control of the stability, electron-transfer kinetics, and pH-dependent energetics of Si/H2O interfaces through methyl termination of Si(111) surfaces. *J. Phys. Chem. B* **2006,** *110* (45), 22291-22294.
278. Yao, M.; Li, T.; Long, Y.; Shen, P.; Wang, G.; Li, C.; Liu, J.; Guo, W.; Wang, Y.; Shen, L.; Zhan, X., Color and transparency-switchable semitransparent polymer solar cells towards smart windows. *Science Bulletin* **2019**.